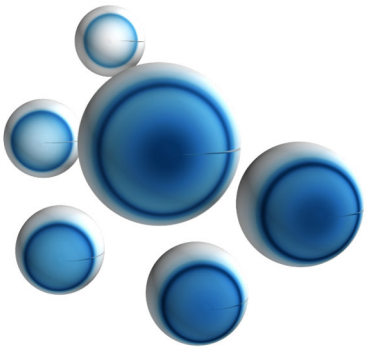

On using stellar pulsations to constrain atmospheric models of strongly magnetic stars

Paola Quitral-Manosalva

Program Doutoral em Astronomia

Departamento de Fisica e Astronomia

2018

Orientador

Margarida S. Cunha, Investigador Principal CAUP

On using stellar pulsations to constrain atmospheric models of strongly magnetic stars

by

Paola Quitral-Manosalva

A thesis submitted in conformity with the requirements
for the degree of Doctor of Philosophy
Departamento de Física e Astronomia
Universidade do Porto

Dedication

To my husband, Jhon W., who has shared this dream. He supported every sacrifice every setback and every triumph.

Acknowledgements

Thanks to Margarida, for guiding and supporting me during this time. Thanks to Carolina and Sascha who were always there when I needed help. The author gratefully acknowledge the financial support of CONICYT/Becas Chile.

Abstract

Studies of high-resolution spectroscopy of rapidly oscillating Ap (roAp) stars show that the pulsations in these stars have a complex behavior in the atmospheric region, which results from their magnetoacoustic nature. Aiming at a better understanding of these pulsations, we carried out a theoretical investigation of the velocity field in these stars and produced observables that could be confronted with the observations currently available for these stars. In particular, we developed a theoretical tool for the computation of the radial velocities in roAp stars, as a function of depth. In the computation, we consider that the star is permeated by a dipolar magnetic field. We explore the amplitude and phase behavior derived from the theoretical radial velocities, for different mode degrees and different lines of sight. We find that for integration over the full disc, in the outermost layers the radial velocity is generally dominated by the acoustic waves, showing a rapid increase in amplitude. The most significant depth-variations in the radial velocity phase are seen for observers directed towards the magnetic equator and for even degree modes with frequencies close to, or above the acoustic cut-off. We found and describe the conditions under which a false node is formed in our model. We also study the photometric visibility of different mode degrees by computing the luminosity perturbation. In particular, we show that the strong distortion that the magnetic field induces in the eigenfunctions results in a significant increase in the visibility of modes of degree $l = 3$ and higher, that may, for that reason, be visible in roAp stars.

Contents

List of Tables

List of Figures

Chapter 1

Introduction

1.1 Asteroseismology

The impossibility of observing the interior of the stars leaves us with a great limitation when it comes to fully understanding their physics. The only way we can test the reliability of our models is through observational evidence. Asteroseismology, that is the study of the oscillations in stars, gives us an excellent opportunity to perform these tests, since through the study of the pulsations observed at the stellar surface it is possible to infer the properties within the star. A beautiful example of this is given by Helioseismology. Thanks to the study of the oscillations in the sun we have a detailed understanding of its internal structure (e.g. Chaplin & Basu, 2008, for a review).

Major progress in asteroseismology was also possible over the last decade thanks to the space missions CoRoT of France/ESA (Baglin et al., 2002) and Kepler of NASA (Koch et al., 2010). These missions were designed to search for extrasolar planets with the transit method, where a high precision in the photometric measurements and long duration of the observation are required, the same requirements as for asteroseismology studies (Christensen-Dalsgaard et al., 2007; Baglin et al., 2001). These missions detected oscillations in thousands of stars, including solar-like and classical pulsators. Their potential was very clear from the first results in asteroseismology (Chaplin et al., 2010; Bedding et al., 2010; Gilliland et al., 2010; Appourchaux et al., 2008). Some important recent results include the determination of the size and shape of the convective core of the binary system KIC 10080943, which is composed of two F-type stars (Schmid & Aerts, 2016), the determination of the rotation rate of the core in γ Dor stars (Van Reeth et al., 2016), and the determination of the internal differential rotation in other solar-type stars besides the sun (Benomar et al., 2018).

The future progress of asteroseismology is also assured, as it is a priority area of study

for a recently approved ESA mission, that will have as one of its primary objectives the asteroseismic observation of thousands of stars. This mission, named PLATO 2.0 (PLAnetary Transits and Oscillation of stars) (Pagano et al., 2014) has the advantage over the already extremely successful Kepler mission, that it will observe bright stars. This will make possible to complement the study of the stars with spectroscopic data from ground-based observatories. Another important mission for asteroseismology is the Transiting Exoplanet Survey Satellite (TESS), launched in April 18, 2018 (Ricker et al., 2010). The main aim of this mission is to find planets with the transit method in stars from classes M to F, but asteroseismology is also part of the additional aims and will be explored by the TESS Asteroseismic Science Consortium (TASC) that involves a large number of researchers working in places across the world. The mission TESS is observing brighter objects than Kepler did, and over the whole sky. It can observe them with two cadences, namely, of 2 minutes and 30 minutes. In addition, there is the possibility of observing in a 20 second cadence. This 20-second cadence observations will be particularly important for the rapidly oscillating Ap (roAp) stars, the objects of study of this thesis, as these stars oscillate at high frequencies. It is expected that the TESS mission, that it going to observe most known roAp stars, and also look into a large number of roAp candidates, will clarify questions still open about these pulsators.

The pulsating stars can be separated in two groups: classical pulsators and solar-like pulsators. In classical pulsators an excitation mechanism amplifies the perturbations making them intrinsically unstable. Usually this leads to oscillations of larger amplitude, hence to larger changes in the brightness of the star. In solar-like pulsators the oscillations are caused by turbulent motion in the convective regions and are intrinsically stable.

The different types of stellar pulsators are shown in the Hertzsprung-Russell (HR) diagram of pulsating stars, Fig. 1.1. Solar-like pulsators are found in the lower part of the main sequence as well as among subgiants and redgiants. Classical pulsators are found in main sequence stars more massive than the sun and in later stages of stellar evolution, as well as during the pre-main sequence. As we mentioned above, the objects of study of this thesis are the roAp stars, located at the base of the instability strip. Because of that they overlap with other pulsating stars like the δ Scuti (δ Sct) and, in part, also with the γ Doradus (γ Dor) stars.

1.1.1 Theory of stellar pulsations in brief

To model a pulsating star we need to consider a hydrodynamic fluid and apply the physics necessary to describe the oscillations. The equations describing the oscillations

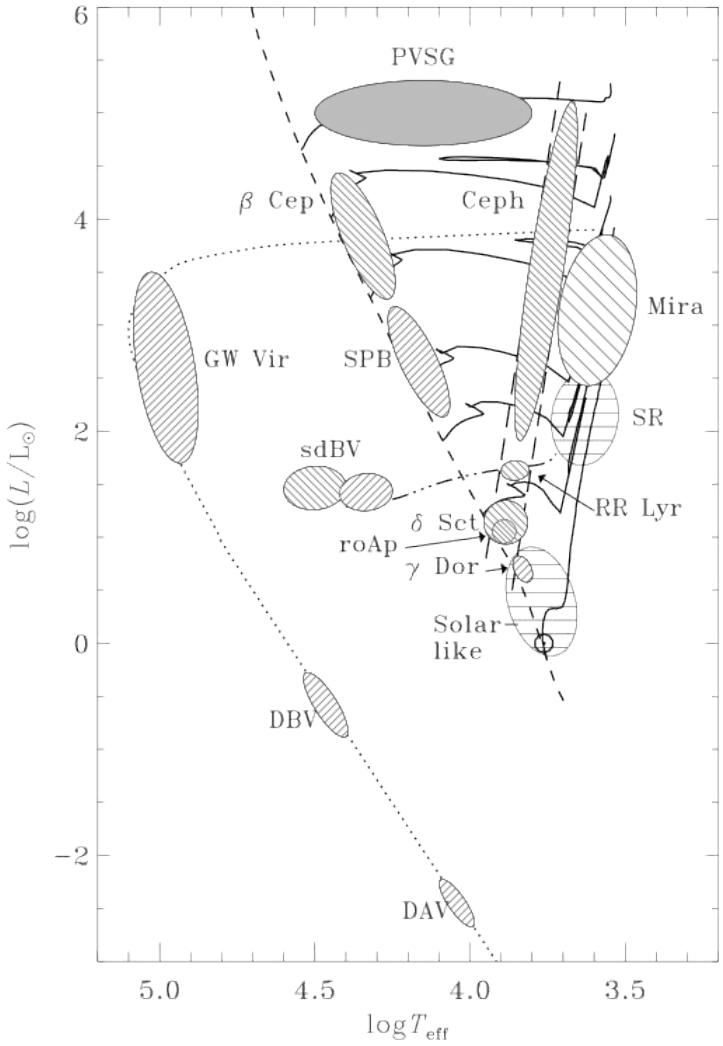

Figure 1.1: Hertzsprung-Russell Diagram showing different classes of pulsating stars. The roAp stars can be found in the region around Log $T_{\rm eff} \approx 3.9$ and Log $(L/L_{\odot}) \approx 1$. Figure extracted from Kurtz (2014), adapted from Aerts et al. (2010).

follow from application of basic laws of conservation of mass, linear momentum, and energy. In general the pulsations are considered to correspond to small perturbations to an equilibrium state and, consequently, the equations are approximated to the linear regime. In addition, since the characteristic thermal time-scale within the star is orders of magnitude larger than the oscillation periods, equations are most often considered in an adiabatic regime (for detailed information, see Aerts et al. (2010); Cunha (2007); Joshi & Joshi (2015)). The solutions to the equations describing linear adiabatic perturbations to a spherically symmetric equilibrium are

$$f'(r,\theta,\phi,t) = \Re\left[f'(r)Y_l^m(\theta,\phi)\exp^{-i2\pi\nu t}\right], \tag{1.1}$$

$$\vec{\xi}(r,\theta,\phi,t) = \Re\left[\left(\xi_r(r)Y_l^m(\theta,\phi)\widehat{e}_r + \xi_h(r)\left(\frac{\partial Y_l^m(\theta,\phi)}{\partial\theta}\widehat{e}_\theta + \frac{\partial Y_l^m(\theta,\phi)}{\partial\phi}\widehat{e}_\phi\right)\right)\exp^{-i2\pi\nu t}\right], \tag{1.2}$$

were f' is a scalar perturbation quantity, and $\vec{\xi}$ is the displacement perturbation, with ξ_r and ξ_h the corresponding radial and horizontal components, and $\widehat{e}_i$ the unitary vectors in the direction of the spherical coordinate system defined by (r,θ,ϕ). Also, $Y_l^m(\theta,\phi)$ are the spherical harmonic special functions and the indices l and m are integer numbers that refer to the harmonic degree and the azimuthal order, respectively, where for each l mode there are $(2l+1)$ azimuthal m orders, giving a set of solutions for each l mode degree. Finally, ν is the frequency of the oscillation which, in the case of a spherically symmetric background, does not depend on m. It depends on yet another quantum number, n, called the overtone of the mode or radial order, and on the mode degree, hence usually being written as ν_{nl}. When the symmetry in the underlying equilibrium model is entirely broken by some additional physical mechanism such as rotation, the degeneracy in azimuthal order is lifted, leading to a set of $2l+1$ different frequencies, for each mode degree, l, that now depended of the azimuthal order, and are usually written as ν_{nlm}. These three quantum numbers determine the spacial configuration of each individual oscillation mode, specifically, n determines the number of nodes in the radial direction, while l and m determine, respectively, the number of nodes at the surface and how many of them are longitudinal lines. For the case when the rotation can be considered a small perturbation, the frequencies, ν_{nlm}, in the frame of reference of the observer are given by the Ledoux rotational splitting relation (Ledoux, 1951)

$$\nu_{nlm} = \nu_{nl0} + m\frac{\Omega}{2\pi}(1 - C_{nl}). \tag{1.3}$$

where Ω is the rotation frequency and C_{nl} is a mode dependent and model dependent quantity that results from the effect of the Coriolis force. Here, the term for the rotational splitting in the expression, written in terms of the frame of the star, is $m\Omega C_{nl}/2\pi$.

Pressure and Gravity modes

Depending on the dominating restoring force one can distinguish different families of solutions for the pulsations equations. In the case of non-rotating, non-magnetic equilibrium, considered here, there are three such families. One of these is the family of f modes, fundamental modes formed at the surface of the star, in which the restoring force is gravity. They are observed at high degree in the sun (Christensen-Dalsgaard, 2002). The other two families, which are the most commonly studied in the context of asteroseismology, are the p-modes and the g-modes. When the dominating force is that associated to the gradient of the pressure perturbation, the solutions are acoustic waves, named pressure modes or p-modes. This kind of mode is more sensitive to the outer layers of the star, therefore, they are usually used to extract information from these regions. When the restoring force is that associated to the buoyancy, the solutions are gravity waves, named gravity modes or g-modes. This kind of modes are more sensitive to the inner layers of the star, therefore they are usually used to extract information of the inner radiative layers, including the core, when it is not convective. When the characteristic frequencies of the p- and g-modes overlap, the general result are mixed-modes, that are oscillation modes that have a dual character, behaving like a gravity wave in a part of the star and like an acoustic wave in another part.

The frequencies of p-modes, g-modes, and mixed-modes can be derived through numerically solving the pulsation equations. Under some conditions they can also be approximated through an asymptotic analysis of the equations. In particular, for p-modes in non-rotating stars and conditioned to $l \ll n$ the oscillation frequencies can be approximated by (Shibahashi, 1979; Tassoul, 1980, 1990; Gough, 1986),

$$\nu_{nl} \simeq \Delta\nu_0 \left(n + \frac{l}{2} + \frac{1}{4} + \alpha \right) - \left[Al(l+1) - \delta \right] \frac{\Delta\nu_{nl}^2}{\nu_{nl}}, \tag{1.4}$$

where,

$$\Delta\nu_0 = \left(2 \int_0^R \frac{dr}{c} \right)^{-1}, \tag{1.5}$$

and is directly related with the inverse of the sound speed travel time across the stellar

diameter, R is the radius at the surface, and c is the sound speed. Moreover,

$$A = \frac{1}{4\pi^2 \Delta\nu_0} \left[\frac{c(R)}{R} - \int_0^R \frac{dc}{dr}\frac{dr}{r} \right], \tag{1.6}$$

α is a quantity that depends slowly on the frequency and on the reflection properties at the surface, and δ is a small correction term. From eq. (1.4) we can see that for two modes with consecutive overtone, n, and the same degree, l, the separation is almost constant (the difference arising only from the second order term and from a possible small change in α). This separation is called "large frequency separation" and it is defined as $\Delta\nu_{nl} = \nu_{n+1l} - \nu_{nl}$. From eq. (1.4) it is also possible to see that when comparing two modes of consecutive overtone, n, for degrees, l, differing by two, the frequency difference comes essentially from the second term in eq. (1.4). The separation between the frequencies of these two modes is called "small frequency separation" and it is defined as $\delta\nu_{nl} = \nu_{nl} - \nu_{n-1l+2}$. It can be approximated by:

$$\delta\nu_{nl} \simeq -\frac{\Delta\nu_0}{\nu_{nl}} \frac{(4l+6)}{4\pi^2} \left(\int_0^R \frac{dc}{dr}\frac{dr}{r} \right). \tag{1.7}$$

Thus, this quantity is sensitive to the gradient of the sound speed, especially in the core.

For the g-modes, the asymptotic relation is usually expressed in terms of the periodicity of the modes. In a non-rotating star and for $l \ll n$, it predicts that the oscillation periods are given approximately by

$$\Pi_{nl} = \frac{\Pi_0}{\sqrt{l(l+1)}} \left(n + \frac{l}{2} + \alpha_g \right), \tag{1.8}$$

(Tassoul, 1980), where α_g is a phase constant, and Π_0 is the basic period spacing given by

$$\Pi_0 = 2\pi^2 \left(\int_{r_i}^{r_f} \frac{N}{r} dr \right)^{-1} \tag{1.9}$$

where N is the Brunt-Väisälä frequency, and r_i and r_f are the limits of the cavity of propagation of the mode.

1.2 Rapidly Oscillating Ap stars

The rapidly oscillating Ap stars were discovered by Kurtz (1982), with the first member of this class, HD 101065 (Przybylski's Star), being claimed as a variable star in Kurtz (1978). They are a particularly interesting class of classical stellar pulsators found amongst a subclass of the chemical peculiar (CP) stars, in particular the CP2 stars, also classically known as Ap stars (Preston, 1974). They are strongly magnetic stars and show excess of rare earth elements (REE). Specifically, so far they seem to be members of the coolest sub-group of Ap stars called the Ap(SrCrEu) stars.

1.2.1 Magnetic field and chemical stratification in Ap stars

The first measurement of a stellar magnetic field, in a sunspot, was carried out by Hale (1908) and it was accomplished through detection of the Zeeman effect. Nearly forty years later, the magnetic field of an Ap star was measured by Babcock (1947). Currently there are several techniques to detect, estimate, and model magnetic fields, some involving looking at the line profile with high-resolution spectroscopy, others considering the polarization of light with photopolarimetry or spectropolarimetry (e.g. Reiners, 2012).

The magnetic fields of sun-like stars are generated in the convective zone, where a dynamo effect occurs, probably originated by the convective movement associated to the differential rotation of the star (Landstreet, 1992). The structure and dynamics of the magnetic fields in solar-like stars are very complex, the fields having a highly inhomogeneous structure and varying on a very short time scale. For example, in the sun it is possible to observe regions where the field changes over the course of weeks or hours, as well as isolated areas where the field is particularly strong (Lüftinger et al., 2010). In contrast with what is observed in solar-like stars, the magnetic field observed in the Ap stars is strong and stable, with a more homogeneous structure generally of a dipolar type. It is also possible to find CP stars whose fields show a multipolar form, like the "spectacular field" of HD 37776, a He-strong star, which presents an octupolar structure (Kochukhov et al., 2011). Nevertheless, the structure of these magnetic fields does not change in an observable time scale. The magnetic field of these stars is thought to be of fossil origin, (Braithwaite & Spruit, 2004; Neiner et al., 2014; Villebrun et al., 2016; Alecian et al., 2017). Although this theory is not fully confirmed, it presents a plausible scenario which explains the current observations.

In addition to strong magnetic fields, the Ap stars have a very slow rotation velocity. Also, it is believed that the Lorentz force suppresses the outer convection zone in the outer layers of the star (Balmforth et al., 2001). Both these facts favour the phenomenon

of levitation of the chemical elements in the atmosphere of Ap stars, leading to chemical stratification. The phenomenon of chemical stratification observed in the Ap stars can also be observed in white dwarf stars (Kurtz, 2013). In the Ap stars the overabundance is more noticeable in heavy elements, including the rare earths. The stratification of these elements allows us to study through high resolution spectroscopic observations the atmospheric layers at different heights.

The element stratification resulting from the levitation of the chemical elements depends on the balance between opposing forces, mainly the radiation pressure and the gravitational force (Kochukhov, 2010). However, when the particles get to sufficiently high layers in the atmosphere, the magnetic field breaks the symmetry of the problem, resulting in an inhomogeneous distribution of the elements and leading to the generation of spots and rings of different chemical compositions. The physical phenomena that are involved in this stratification of elements are known, but there is still much to study because the models are not in agreement with the observations (Alecian, 2015; Alecian & Stift, 2017; Kochukhov & Ryabchikova, 2017).

The vertical stratification of elements can also be derived from high resolution spectroscopic observations, using complex atmospheric models that account for the possibility of such stratification, such as the LL models (Shulyak et al., 2004).

1.2.2 Origin and properties of pulsations in roAp stars

The Ap stars are laboratories for studies of diffusion and magnetic fields, as well as for the interaction between these two with convection. Due to the chemical stratification of elements, their atmospheres are very complex. They are, thus, perfect targets for testing and developing atmospheric models. The fact that some of them pulsate opens a nice window of opportunity for such tests. However, not all the Ap stars exhibit oscillations and even amongst the cooler subgroup many are not found to pulsate. These stars, in which roAp type pulsations have been searched for and not found, are usually called non-oscillating Ap (noAp) stars. They are also Ap stars, and some of them have global parameters very similar to the roAp stars, but for some unknown reason, do not seem to present oscillations. It should be noticed, however, that in fact it is not possible to determine if they do not oscillate or if their oscillations are simply not detected, due to some observational bias. The TESS mission, mentioned earlier, should help clarifying this matter.

The roAp stars are characterized by oscillations with short periods so far detected within the range of 6 to 24 min (Kurtz, 1982; Alentiev et al., 2012). Their magnetic

fields have typical mean magnitudes of a few kG (Mathys, 2017), and their effective temperatures range from $\sim$ 6100 K to 9000 K. Up to this day, 61 pulsators of this type have been found (Smalley et al., 2015). The pulsations they exhibit are interpreted as high radial order p-modes that are modified in the surface layers by the magnetic field. Since they were first discovered efforts have been made to find new roAp stars. The first, and most successful one, is the Cape rapidly oscillating Ap star survey (Martinez et al., 1991) in the southern hemisphere. The Nainital Cape survey (Joshi et al., 2016) and the Hvar survey (Paunzen et al., 2012), are additional examples in the northern hemisphere. Recently, 5 new additions to this class of pulsators was possible thanks to the Kepler satellite (Balona et al., 2010, 2011; Kurtz et al., 2011; Holdsworth et al., 2014a; Smalley et al., 2015) and the ground-based WASP survey led to the discovery of 10 more roAp stars (Holdsworth et al., 2014a).

As we mentioned earlier, in the HR diagram the roAp stars overlap with the δ Sct stars, which are also classical pulsators, with an effective temperature in a range similar to that found for roAp stars. They, however, seem to be more diverse, including main sequences stars, but also pre-main-sequence and early subgiant stars. These stars are multiperiodic p-mode pulsators, but their periods are typically longer than in roAp stars, varying from 15 min to 8 h. The main difference with respect to the pulsations in roAp stars is that the pulsations in the δ Sct stars are of low radial order. In addition, δ Sct stars can also exhibit g-mode pulsations, that are the pulsations found in γ Dor stars, in which case they are called hybrid pulsators (Bowman & Kurtz, 2018). In contrast, no clear evidence for g-modes in roAp stars has so far been found. It should also be noted that roAp stars are not the only chemically peculiar stars found to pulsate. In fact, the Am stars, which are non-magnetic chemically peculiar stars (CP1 in the Preston Classification) with excess in Fe, were for long time thought not to exhibit pulsations. However, they are now in some cases known to pulsate (Kurtz, 1989; Smalley et al., 2016). Nevertheless, only the coolest Am stars (within effective temperatures in the range from 6900 K to 7600 K) show pulsations (Smalley et al., 2011, 2016). The reason for these oscillations is not well understood yet. Moreover, they are usually found in binary systems (Joshi et al., 2006), unlike the roAp stars.

Currently, the most likely explanation for the instability of the pulsations observed in the roAp stars is the κ-mechanism acting in the hydrogen ionization zone, as it is described by Balmforth et al. (2001); Cunha (2002); Cunha et al. (2013). In the case of roAp stars the κ-mechanism acts in the ionization zone of the hydrogen. The oscillations are driven when a layer can gain heat under compression of the gas. In the zone where the gas is partially ionized the compression ionizes it further, without raising the tem-

perature much. Thus, the opacity increases under compression, blocking the radiation and capturing more energy. The pressure increases with the extra heat, leaving the layer out of an equilibrium state, the gas starts to expand, and the opacity drops. The temperature drops slightly and the ionized gas begins to recombine, thus, the gas gives back energy, making the pressure decrease causing a new compression and starting a new cycle. Because of the extra heat gained under compression the amplitude of the perturbation increases from cycle to cycle. Hence the perturbation is intrinsically unstable. But there are still doubts as to whether this is the only mechanism that can excite the oscillations in these stars, since this mechanism does not explain the presence of some very high frequencies that are observed, especially the frequencies that are above the acoustic cut-off frequency. Another possible explanation, suggested by Cunha et al. (2013), is that the turbulent pressure in the outer convective zone can act like an excitation mechanism for these very high frequencies.

Because the rapidly oscillating Ap stars have strong magnetic fields, the pulsation axis is expected to be nearly aligned with the magnetic field axis and, in turn, not with the rotation axis, as is commonly seen in other types of pulsating stars, where the most significant agent breaking the underlying symmetry is rotation. The misalignment between the pulsation and rotation axes gives rise to the oblique pulsator model proposed by Kurtz (1982). According to this model the pulsation mode can be described by a single spherical harmonic, and because of the misalignment between the pulsation axis and the rotation axis, the luminosity of the star is modulated as the star rotates. This modulation gives rise to a multiplet in the pulsation spectra whose sidelobes are separated by exactly the rotation frequency. Observationally the impact of rotation (not considered in the original oblique pulsator model) is seen mostly in the different amplitudes of the side lobes observed in some stars, which cannot be explained by the effect of the magnetic field.

Since the introduction of the oblique pulsator model, that was essentially geometrical in nature, several studies have been carried out in an attempt to improve it (Dziembowski & Goode, 1985; Shibahashi & Takata, 1993; Takata & Shibahashi, 1994). The most recent development to this model, with the inclusion of the combined effects of rotation and magnetic field, is discussed in the papers by Bigot & Dziembowski (2002); Bigot & Kurtz (2011).

The modulation of the pulsation light curve due to the misalignment of the rotation and pulsation axes facilitates the identification of the pulsation modes. Generally, it is found that the observed modes are axi-symmetric about the pulsation axis ($m = 0$ in that reference frame), but can be significantly distorted by the magnetic field, being

best represented by the superposition of different degrees, l. From the theoretical point of view, a possible justification for a predominance of axi-symmetric modes ($m = 0$ in the pulsation frame), with maximum amplitude along the pulsation axis, hence, also, along the magnetic axis, was put forward by Balmforth et al. (2001), who showed that the modes that are aligned with the magnetic field are more likely excited, because the magnetic field more easily suppresses convection in the polar regions of the star. The dominant mode in these magnetic stars seems to be of degree $l = 1$ (Bigot & Kurtz, 2011). In fact, several of the roAp stars in which it has been possible to identify the oscillation modes are oscillating in a $l = 1$, $m = 0$ mode (e.g. Kurtz et al., 1990, 2005b; Bruntt et al., 2009; Bigot & Kurtz, 2011). Nevertheless, recently several stars have been found oscillating with modes of $l = 2$, $m = 0$ (e.g. Balona et al., 2011; Saio et al., 2012; Holdsworth et al., 2014a), which gives us a very interesting scenario to explore.

1.2.3 Pulsations in the atmospheres of roAp stars

Since the first detection of radial velocity variations in roAp stars (Matthews et al., 1988), many high-resolution spectroscopic studies have made possible the extraction of large amounts of information about the pulsations through the inspection of these radial velocities. A distinguishing feature of roAp pulsations demonstrated by these studies is an unusually large difference in pulsation amplitudes and phases observed in spectral lines of different chemical elements and even different ions of the same element. That is due to the stratification of metals, in particular rare-earth elements, in the atmosphere of peculiar stars, which gives us the opportunity of observing different heights in the atmosphere of the star. Moreover, the fact that some of these elements are not uniformly distributed, but rather concentrated in spots, means that through high-resolution spectroscopy one can probe different areas on the stellar disk.

With the development of instruments capable of producing very precise time-series of high-resolution spectroscopy, the measurement of time variations for a single spectral line became possible (e.g., Kochukhov (2005)). This, along with the stratification of elements present in Ap stars, allows for the study of pulsation-induced velocity fields throughout these stars' atmospheres. In fact, the study of pulsations in the presence of stratification of elements opens the interesting possibility to obtain a 3D-view of the atmospheres of roAp stars through the spectroscopic time-series observations (Baldry et al., 1998; Kurtz et al., 2005a; Kochukhov, 2010; Freyhammer et al., 2009). Different rare earth elements show a different pulsation amplitude because they are located at different depths. As an example, in the study of the roAp star HD24712 made by Ryabchikova et al. (2007a)

using high-resolution spectroscopy and polarimetry we see the variation of the pulsation amplitude in the rare earth elements ranging from 150 to 400 ms^{-1}, while other elements like Mg, Si, Ca, and Fe seem to be almost constant. In another work, by Kurtz et al. (2005a) based on the bisector analysis of the spectral lines on the star 33 Lib, the authors studied the radial velocities for several spectral lines, for example in NdII and NdIII lines, and found that the radial velocities vary across the region where the lines are formed.

1.2.4 Modeling of the pulsations in the presence of a magnetic field

The oscillation modes in roAp stars are not well modeled with a standard pulsation model. The frequencies of the oscillations, and in particular the large separation, are not well explained with this model. The discrepancy arises from the effect of the strong magnetic field present in the roAp stars which standard pulsation models do not take into account. Moreover, the pulsation velocity field in the outer layers also differs very significantly from that expected in non-magnetic stars.

The magnetic field in roAp stars influences pulsations essentially in the star's outer layer. It is possible to split this magnetic boundary layer in two regions: the magnetoacoustic layer and magnetic-dominant layer. The first region is where the Lorentz force and the acoustic restoring force, produced by the gradient of the pressure perturbation, are comparable. In this region the waves are magnetocacoustic in nature. On the other hand, the magnetic dominant layer is where the magnetic field dominates the dynamics of the problem (Cunha, 2007). In the latter the magnetoacoustic wave is decoupled and it can be described as the sum of two components: a magnetic and an acoustic wave. In the interior, below the magnetic boundary layer, the behavior of the fluid is dominated by the gas pressure and the magnetic field effect on the oscillations can be neglected. There, the wave is essentially acoustic in nature.

A number of different theoretical non-perturbative analyses have been developed over the years to address the coupling between the magnetic field and pulsations in roAp stars in an adiabatic framework (Dziembowski & Goode, 1996; Bigot et al., 2000; Cunha & Gough, 2000; Saio & Gautschy, 2004; Cunha, 2006; Sousa & Cunha, 2008a; Khomenko & Kochukhov, 2009; Sousa & Cunha, 2011). Among these, the works by Cunha (2006) and Saio & Gautschy (2004) are possibly the most comprehensive in that, on the one hand they account for the whole star, and, on the other, they consider a wide range of frequencies, finding cases of optimal coupling between the magnetic and acoustic waves that were missed in some of the other works. Both these works consider small adiabatic

perturbations to the stellar equilibrium in the Cowling approximation (Cowling, 1941). They address the pulsation problem in the presence of the magnetic field, including the Lorenz force as a restoring force in the magnetohydrodynamics equations, in the limit of perfect conductivity. They nevertheless use two different mathematical approaches to solve the system of equations. Saio & Gautschy's approach consists in an expansion of the solutions in a series of spherical harmonics, that is an infinite sum that is truncated when the solution converges. Cunha's method uses the variational principle to compute the magnetic perturbation to the eigenfrequencies.

1.3 Context and aims of the this work

In this work we have used the pulsation modeling approach of Cunha (2006). This model considers a local plane-parallel approximation in the magnetic boundary layer to solve the magnetohydrodynamic equations that describe the linear, adiabatic pulsations, considering a Cartesian coordinate system at each latitude, where the z-axis increases outwardly. The system is solved locally for each latitude assuming a locally constant magnetic field. In practice this means that both horizontal and vertical derivatives of the magnetic field are neglected, which is justified by the fact that the magnetic field considered varies only on large scales. The problem is then described by a fourth-order system of complex total differential equations, if $m = 0$, or a sixth-order system, if $m \neq 0$, which is solved with a Runge-Kutta algorithm. The variables are complex because the boundary conditions allow for energy losses by the system. The solutions in the magnetic boundary layer are then matched to appropriate solutions in the interior, where the magnetic effect is neglected. Moreover, the boundary conditions at the outermost layer are derived one from the solutions valid for the magnetic-dominant layer and two by imposing that the magnetic field is matched onto the appropriate solution for a vacuum field. This code, which is at the base of the code developed and applied in this thesis, is named MAgnetic Perturbations to Pulsations in Ap stars (or MAPPA code).

In addition to the above-mentioned study, which considers the solutions for the whole star but focuses its analysis only on the magnetic impact on the eigenfrequencies, a toy model for the study of the radial velocity field in the outermost layers of roAp stars was developed by Sousa & Cunha (2011). It consists in a theoretical analysis of pulsations, in the magnetic-dominated region only, under an isothermal approximation.

Through this thesis we further develop the oscillation model first presented in Cunha (2006) to compute the observable quantities radial velocity and luminosity perturbation. The aim of this calculation is to study the diversity of solutions that can be found when

the modes are highly distorted by the magnetic field, highlight the differences with respect to normal modes, and compare the model observables with the observations.

Throughout the remainder of this thesis the work is organized as follows: we present the mathematical background in Chapter 2. The radial velocity calculation and some general results are presented in Chapter 3. In Chapter 4 we discuss some particular results for the radial velocities, either because they are interesting or because they are very different. In Chapter 5 we analyze the visibility of the modes, both in terms of the luminosity perturbation and in terms of the radial velocity, for modes of degree up to 7.

Chapter 2

Theoretical model of the oscillations in a roAp star

2.1 Mathematical background

The models by Cunha (2006) and by Saio & Gautschy (2004) are particularly relevant to the current study, as they consider a realistic equilibrium model, full coupling between the interior and atmosphere and allow the probing of frequencies beyond the acoustic cut-off. Both models show that the eigenfunctions are strongly distorted in the outer layers by the presence of the magnetic field, which not only changes the amplitude of the perturbations, but also adds a significant angular component to the displacement. This type of distortion has been detected also in observations by Kochukhov (2004).

The pulsation model used throughout this work to calculate the radial velocity and the luminosity for roAp stars, is an extension of the MAPPA code by Cunha (2006). As mentioned earlier, in this model two regions are considered, namely, the interior of the star, where the magnetic pressure is neglected and the outer layers, named the magnetic boundary layer, where the magnetic pressure is comparable or larger than the gas pressure. In the interior, the standard oscillation model is used to describe the p-modes. In the Magnetic boundary layer, with a characteristic depth of only a few % of the radius, we consider the direct effect of the magnetic field on the pulsations, and we describe them by the following system of magnetohydrodynamic equations:

$$\frac{\partial \vec{B}}{\partial t} = \nabla \times (\vec{v} \times \vec{B}), \tag{2.1}$$

$$\frac{D\rho}{Dt} + \rho \nabla \cdot \vec{v} = 0, \tag{2.2}$$

$$\rho\frac{D\vec{v}}{Dt} = -\nabla p + \vec{j}\times\vec{B} + \rho\vec{g}, \tag{2.3}$$

$$\frac{Dp}{Dt} = \frac{\gamma p}{\rho}\frac{D\rho}{Dt}, \tag{2.4}$$

where the current density is $\vec{j} = 1/\mu_0\,(\nabla\times\vec{B})$, μ_0 is the permeability in the vacuum, ρ is the density of the gas, p is the pressure, $\vec{g}$ is the gravitational field, $\vec{\xi}$ is the displacement vector and $\vec{v} = \partial\vec{\xi}/\partial t$ is the velocity.

Next, we take small Eulerian perturbations to the equilibrium structure, $\rho = \rho_0 + \rho'$, $p = p_0 + p'$ and $\vec{B} = \vec{B}_0 + \vec{B}'$. Then, within the Cowling approximation, in the limit of perfect conductivity, and neglecting products of small quantities, the resulting system of equations is

$$\frac{\partial^2\vec{\xi}}{\partial t^2} = -\frac{1}{\rho_0}\nabla p' + \frac{\rho'}{\rho_0^2}\nabla p_0 + \frac{1}{\mu_0\rho_0}\left(\nabla\times\vec{B'}\right)\times\vec{B}_0, \tag{2.5}$$

$$p' = -\vec{\xi}\cdot\nabla p_0 - \gamma p_0\nabla\cdot\vec{\xi}, \tag{2.6}$$

$$\rho' = -\vec{\xi}\cdot\nabla\rho_0 - \rho_0\nabla\cdot\vec{\xi}, \tag{2.7}$$

$$\vec{B}' = \nabla\times\left(\vec{\xi}\times\vec{B}_0\right). \tag{2.8}$$

From here onwards the subscript '0" on equilibrium variables will be dropped, being then, ρ, p, $\vec{B}$, the equilibrium quantities.

Since the magnetic boundary layer is thin and the magnetic field varies on large scales only, the equations in this region of the star are solved by performing a plane-parallel approximation and assuming a local constant magnetic field, at each latitude. Consequently, at each latitude a local-coordinate system (x, y, z) is defined with the z component pointing outwards of the star, and such that the magnetic field is zero in the y direction, as it is represented in Fig. 2.1(a). The local magnetic field at a given co-latitude θ, is then given by,

$$\vec{B} = \left(\frac{B_p}{2}\sin(\theta), 0, B_p\cos(\theta)\right), \tag{2.9}$$

where B_p is assumed to be constant, which is a good approximation given that the layer is thin. Furthermore, the system is solved under a linear approximation and, as a consequence, it does not inform about the amplitude of the displacement.

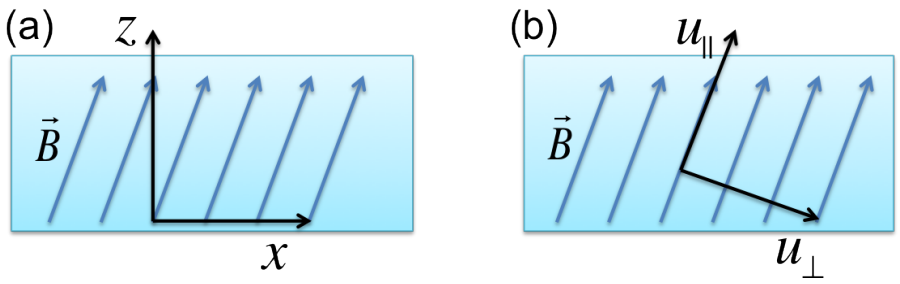

Figure 2.1: Local coordinate systems used in the MAPPA code: (a) coordinate system with z pointing out of the star, and the x and y coordinates defined using the condition $B_y = 0$. (b) second local coordinate system used in this work defined by $\vec{e_{\|}} = \vec{B}/\|\vec{B}\|$ end $\vec{e_{\perp}} = \vec{e_y} \times \vec{B}/\|\vec{B}\|$.

This model predicts shifts in the frequencies that are caused by the pulsation distortion of the magnetic field. The frequency shifts increase smoothly up to a point when they decrease suddenly, starting to increase again for frequencies still larger. This is illustrated in Fig 2.2 where the frequency shifts, Δf (not to be confused with the large separation $\Delta\nu$), are shown as a function of the cyclic frequency f. These sudden jumps repeat periodically as the frequency increases, every time the coupling between the oscillations and the magnetic field is optimal. This can be seen more clearly in the panels (c) and (d) with magnetic fields of 3 kG and 4 kG, respectively. This behavior of the frequency shifts was found also by Saio & Gautschy (2004), and in both works it was found that around these frequency jumps the eigenfunctions are most strongly perturbed, and their modeling becomes increasingly difficult. Due to the difficulty in modelling the eigenfunctions close to the frequency jumps mentioned before, in the present work we will not consider such frequencies.

Throughout this thesis we will consider only solutions corresponding to the azimuthal order $m = 0$, thus, the solution for the displacement at each latitude, in the local coordinate system, will be written as $\vec{\xi} = \xi_x \widehat{e}_x + 0\widehat{e}_y + \xi_z \widehat{e}_z$, where $\widehat{e}_x$, $\widehat{e}_y$ and $\widehat{e}_z$ are the unit vectors of the local coordinated system. Moreover, a second coordinate system will be used in the local approximation, this second coordinate system denoted by $(u_{\|}, y, u_{\perp})$, shown in Fig. 2.1(b), has axes parallel and perpendicular to the magnetic field. This coordinate system is obtained from the first through a rotation of α_B around the y axis, where α_B is the angle between the z direction and the direction of the magnetic field $\vec{B}$. In this case the solutions are written in the form $\vec{\xi} = \xi_{\|}\widehat{e}_{\|} + 0\widehat{e}_y + \xi_{\perp}\widehat{e}_{\perp}$, where $\widehat{e}_{\|}$ and $\widehat{e}_{\perp}$ are the unit vectors in the direction parallel and perpendicular to the magnetic field.

In order to understand the solutions given by the MAPPA code we need to consider separately the two different regions mentioned before, namely the magnetic boundary

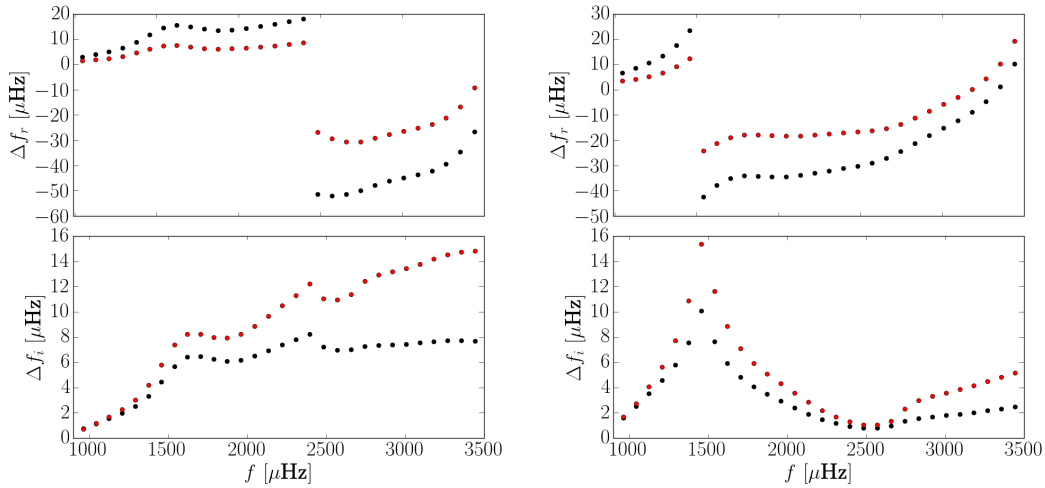

(a) $B_p = 1$ kG

(b) $B_p = 2$ kG

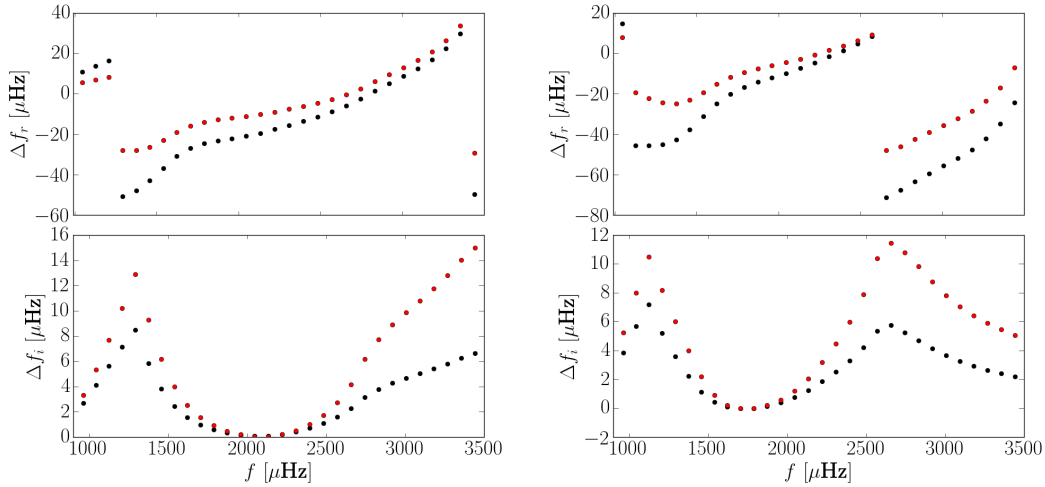

(c) $B_p = 3$ kG

(d) $B_p = 4$ kG

Figure 2.2: Real (top) and imaginary (bottom) parts of the frequency shifts Δf, as a function of the cyclic frequency f, for the modes degrees $l = 0$ (black dots) and $l = 1$ (red dots), computed using the MAPPA code (Cunha, 2006). The results are shown for four different magnetic fields, namely: (a) $B_p = 1$ kG, (b) $B_p = 2$ kG, (c) $B_p = 3$ kG, and (d) $B_p = 4$ kG.

Table 2.1: Parameters of the stellar model considered in this work. Mass, radius, effective temperature, temperature of the isothermal atmosphere, and acoustic cut-off frequency.

Mass	Radius	$T_{\rm eff}$	$T_{\rm iso}$	$f_{\rm cut-off}$
1.8 $M_\odot$	1.57 $R_\odot$	8363 K	6822 K	2.458 mHz

layer of the star, and the interior of the star. In the interior, dominated by the pressure of the gas, we find two decoupled solutions, an acoustic wave, that is displacing the gas in the radial direction, and a transverse Alfvén wave that is displacing the gas in a local horizontal direction (Cunha & Gough, 2000; Dziembowski & Goode, 1996). Moreover, in the magnetic boundary layer the solutions can be best understood by further dividing this layer into two different regions (Cunha, 2007), namely, the region where the pressure of the gas is of the same order of magnitude as the magnetic pressure and the outermost layers, where the magnetic pressure dominates. In the former, we have magnetoacoustic waves, while in the latter the waves decouple once again in the form of acoustic waves that are displacing the gas in the direction parallel to the magnetic field, and of compressional Alfvén waves, that are displacing the gas in the direction perpendicular to the magnetic field (Sousa & Cunha, 2008b).

2.2 Equilibrium model

To model the radial velocities in the outer layers of the stars, we consider small perturbations to an equilibrium model with global properties within the range observed for this class of pulsators (see in Table 2.1). The parameters of this model also set it within the region where the excitation mechanism of roAp stars can be theoretically understood (Balmforth et al., 2001; Cunha, 2002; Saio, 2005; Cunha et al., 2013).

As we are particularly interested in studying the pulsation properties in the atmosphere of the star, the equilibrium model, computed with the CESAM code (Code d'Evolution Stellaire Adaptatif et Modulaire) (Morel, 1997), has had the atmosphere extended. This can be seen in Fig. 2.3 that shows the pressure, density and temperature on the outer 2% of the stellar model used for this work. The vertical red line indicates the surface of the star, and we can see how the model extends from the surface with a small atmosphere.

To increase the size of the atmosphere we added an isothermal atmosphere on the top of the model in order to allow us to reach lower densities such as those found in the self consistent models of peculiar stars' atmospheres (Shulyak et al., 2009). In the isothermal atmosphere the pressure and density have the form: $p = p_s e^{-\eta/H}$ and $\rho = \rho_s e^{-\eta/H}$,

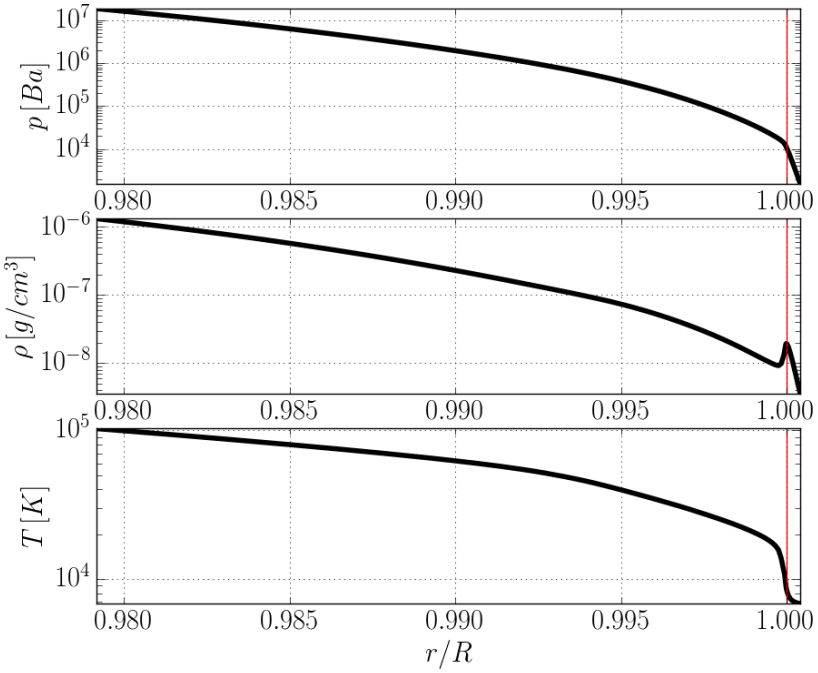

Figure 2.3: pressure, density and temperature as a function of the normalized radius of the CESAM stellar model in the outer 2% of the star. The red vertical line represents the bottom of the photosphere.

respectively, were η is the height measured from the bottom of the isothermal atmosphere, p_s and ρ_s are the pressure and density at the top of the CESAM model with values of 2×10^3 Ba and 4×10^{-9} g cm^{-3} respectively, and H is the pressure scale height.

2.3 Decoupling of the waves

The system of equations (2.5)-(2.8) is solved up to a normalizing constant by applying adequate boundary conditions. At the surface the magnetic field is matched continuously onto a vacuum field. The remaining boundary conditions are obtained by matching the numerical solutions to approximate analytical solutions in the regions where the magnetic and acoustic waves are decoupled, as described below.

In the interior of the star the acoustic component corresponds to the solution obtained when $\vec{B} = 0$ and the magnetic component is assumed to be a wave that dissipates inside the star. Then, there the numerical solution for the magnetic component is matched onto an analytical asymptotic solution for an Alfvén wave propagating towards the interior of the star (see Cunha & Gough (2000) for details).

The final boundary condition consists in matching the numerical solution for the parallel component of the displacement to its analytical counterpart in the isothermal atmosphere. In the isothermal atmosphere the analytical solutions are those derived in the work of Sousa & Cunha (2011). There the magnetoacoustic waves are already decoupled into a (slow) acoustic wave and a (fast) compressional Alfvén wave that move in the directions parallel and perpendicular to the magnetic field, respectively, and have the form,

$$\varepsilon_{\parallel} = \frac{|A_s|}{p^{1/2}} \exp i(\pm k_{\parallel}\eta + \omega t + \phi_s), \tag{2.10}$$

$$\varepsilon_{\perp} = |A_f| J_0(2\sqrt{\chi\rho}) \exp i(\omega t + \phi_f), \tag{2.11}$$

where ω is the angular oscillation frequency, $|A_s|$, ϕ_s, $|A_f|$, ϕ_f are the amplitudes (A) and phases (ϕ) of the acoustic and magnetic waves respectively, at the bottom of the isothermal atmosphere, that depend on the latitude, J_0 is the Bessel function and χ is a constant $\chi = \mu_0 H^2 \omega^2 / B_p^2$. Moreover, the parallel component of the wavenumber is defined by:

$$k_{\parallel} = \sqrt{\frac{\omega^2 \rho}{\gamma p \cos^2 \alpha_B} - \frac{1}{4H^2}}, \tag{2.12}$$

where γ is the fist adiabatic exponent. The parallel wavenumber $k_{\parallel}$ can be real or imaginary. In the former case, the parallel component of the solution (acoustic wave) is

oscillatory,

$$\varepsilon_{\parallel} = \frac{|A_s|}{p^{1/2}} \exp i(-k_{\parallel}\eta + \omega t + \phi_s), \tag{2.13}$$

thus, the eq. (2.10) takes the form of a running behavior, where the sign on the exponent was chosen to guarantee that the wave propagates outwardly. While in the latter case, when $k_{\parallel}$ is imaginary, eq. (2.10) is turned into,

$$\varepsilon_{\parallel} = \frac{|A_s|}{p^{1/2}} \exp\left(-k_{\parallel}\eta\right) \exp i(\omega t + \phi_s), \tag{2.14}$$

resulting in an exponential behavior. In Eq. (2.14), $k_{\parallel}$ now stands for the modulo of the parallel wavenumber and the sign in the exponent was chosen such as to guarantee that the energy of the wave decreases outwardly.

Inspecting the parallel component of the wavenumber $k_{\parallel}$, we can see that it depends on latitude through the angle α_B. Therefore, even when the frequency of the oscillation is below the acoustic cut-off frequency for a non-magnetic star, in the presence of a magnetic field $k_{\parallel}$ will became real and the solutions will beceme oscillatory when the co-latitude is larger than a given critical value. The critical frequency,

$$\omega_c = \sqrt{\frac{\gamma p \cos^2 \alpha_B}{4H^2\rho}}, \tag{2.15}$$

defines the co-latitude at which the parallel component of the solution changes its behavior from exponential to oscillatory in the presence of the magnetic field. We shall call that co-latitude the critical angle, α_{cr}.

For a dipolar magnetic field, the critical frequency has its maximum value at the magnetic pole, corresponding to the critical frequency in the absence of a magnetic field, (i.e. to the acoustic cut-off frequency). But it decreases as the magnetic equator is approached. As a consequence, even if the oscillation frequency is below the acoustic cut-off frequency, it will always be above the local critical frequency for co-latitudes larger than a critical value and, thus, there are always going to be wave energy losses in the equatorial zone when the magnetic field is considered.

2.4 Displacement solutions

Due to the structure of the global magnetic field, at each latitude the distortion of the oscillation is different. In particular, the magnitude and direction of the magnetic field is different at different latitudes, affecting differently both the amplitude and characteristic

scale of the displacement. As a consequence, to model the waves in the full star we have used the MAPPA code to compute the distorted waves at 99 different latitudes, equally separated in $\cos(\theta)$. The displacement at each latitude is normalized in the inner layer of the computation of the code, where the waves are decoupled and the vertical component is the same as an unperturbed acoustic solution satisfying the regularity condition at the center of the star. The distortion caused by the magnetic field and the effect of the coupling of the acoustic and magnetic waves on the solutions in the magnetic boundary layer can then be compared between latitudes.

As the MAPPA code has limitations for the size of the isothermal atmosphere that can be added to the stellar model, we use the eqs. (2.14) or (2.13) and (2.11), valid for an isothermal atmosphere, to describe the solutions beyond the outermost layer of the extended CESAM model.

To obtain the values of the amplitudes and phases $|A_s|$, ϕ_s,$|A_f|$ and ϕ_f, we use the displacements obtained from the MAPPA code written in terms of the directions parallel and perpendicular to the magnetic field, $\xi_\parallel$ and $\xi_\perp$, respectively. We fit the numerical solution for the parallel component with the eqs.(2.14), or (2.13) depending on the value of α_{cr}, using the the real and imaginary part of the solution in the isothermal atmosphere,

$$\Re[\xi_\parallel]^2 + \Im[\xi_\parallel]^2 = \Re[\varepsilon_\parallel]^2 + \Im[\varepsilon_\parallel]^2, \tag{2.16}$$

and

$$\frac{\Im[\xi_\parallel]}{\Re[\xi_\parallel]} = \frac{\Im[\varepsilon_\parallel]}{\Re[\varepsilon_\parallel]}. \tag{2.17}$$

In the same way, we fit the numerical solution for the component perpendicular to the magnetic field $\xi_\perp$ with the eq.(2.11), using,

$$\Re[\xi_\perp]^2 + \Im[\xi_\perp]^2 = \Re[\varepsilon_\perp]^2 + \Im[\varepsilon_\perp]^2, \tag{2.18}$$

and

$$\frac{\Im[\xi_\perp]}{\Re[\xi_\perp]} = \frac{\Im[\varepsilon_\perp]}{\Re[\varepsilon_\perp]}. \tag{2.19}$$

With these fits, we extend the numerical solutions throughout an atmosphere with a size larger than 0.2% of the radius of the star, corresponding to 12 times the pressure scale height.

To illustrate the solutions in the extended atmosphere, we will discuss below the cases of two particular cyclic frequencies ($f = \omega/2\pi$). First, we shall consider a frequency of 1.2 mHz, that is far below the acoustic cut-off (see in Table 2.1). In this case, the acoustic

waves change from having a standing character to having a running character at a critical angle $\alpha_{cr} = 62°$ (*cf.* eq. (2.15)), meaning that for co-latitudes larger than this angle the local critical frequency is smaller than 1.2 mHz. The second frequency is of 2.2 mHz, that is below the acoustic cut-off but close to it, with a critical angle of only $\alpha_{cr} = 33°$.

The displacement as a function of the radius for the frequency of 1.2 mHz is shown in Fig. 2.4 for three different latitudes. In the left panels we show the components of the solution in the innermost part of the magnetic boundary layer, using the local coordinates system (x, y, z), and on the right panels the local parallel and perpendicular components of the solution in the outermost part of the magnetic boundary layer, using the coordinate system $(u_{\parallel}, y, u_{\perp})$. The use of the two different coordinate systems at the two limit regions is aimed at recognizing the acoustic and magnetic waves in the regions where they are decoupled.

In Fig. 2.4(a) and (b) we show the displacement for co-latitudes of 31° and 53°. At these co-latitudes the frequency is below the critical frequency. Thus, in the isothermal atmosphere, marked by the yellow-shaded region on the right panels, the acoustic wave (component of the displacement parallel to the magnetic field) shows a standing behavior as does the compressional Alfvén wave (perpendicular component), which shows, in addition, a constant amplitude in that part of the atmosphere, as expected from eq. (2.11).

In the inner layers shown on the left panels, the acoustic wave (vertical component ξ_z in these layers), also presents an almost standing behavior, that is not completely standing because the coupling of the acoustic and magnetic waves in the layers above leads to some energy loss. Moreover, the Alfvén wave (the horizontal component ξ_x) has a clear running behavior, dissipating towards the interior of the star as expected from the boundary conditions.

For comparison, Fig. 2.4(c) illustrates a case of a co-latitude of 78°. As expected, for a co-latitude closer to the equator, where the frequency of the wave is larger than the critical frequency, the acoustic wave will, instead, have a running behavior in the atmosphere. As a consequence, at this co-latitude the exponential growth of the wave amplitude is larger than at the previously considered co-latitudes of 31° and 53°. Because the energy carried by the acoustic running wave is conserved, the wave amplitude increases as the inverse of the root square of the density (or, equivalently in these layers, of the root square of the pressure- cf eq. (2.10)). We note, for comparison, that for the co-latitudes of 31° or 53°, the decreasing exponential term in eq. (2.14) partially compensates the exponential increase associated with the decrease of the pressure, leading to a smaller increasing rate of the amplitude with height in the atmosphere, consistent with a decrease in the energy

content of the acoustic wave.

In Fig. 2.5 we consider a higher frequency value of 2.2 mHz. We can identify the same features as for the previous frequency. In the inner layers (left panels) we see the almost standing behavior of the acoustic wave (ξ_z), and the running behavior of the the Alfvén wave (ξ_x). Also, in the outermost layers, in the isothermal atmosphere, the compressional Alfvén wave ($\xi_\perp$) shows a constant amplitude (right-bottom panels). The main difference appears in the acoustic waves parallel to the magnetic field (right-top panels). Here, as the frequency is higher, the angle of critical frequency, α_{cr}, is much smaller than in the previous case. By comparing the results at different co-latitudes in Fig. 2.5, it becomes clear that the standing behavior of the acoustic waves ($\xi_\parallel$) in the isothermal atmosphere is seen only at the first co-latitude, of 31°, while for the co-latitudes of 53° and 78° we identify a running behavior.

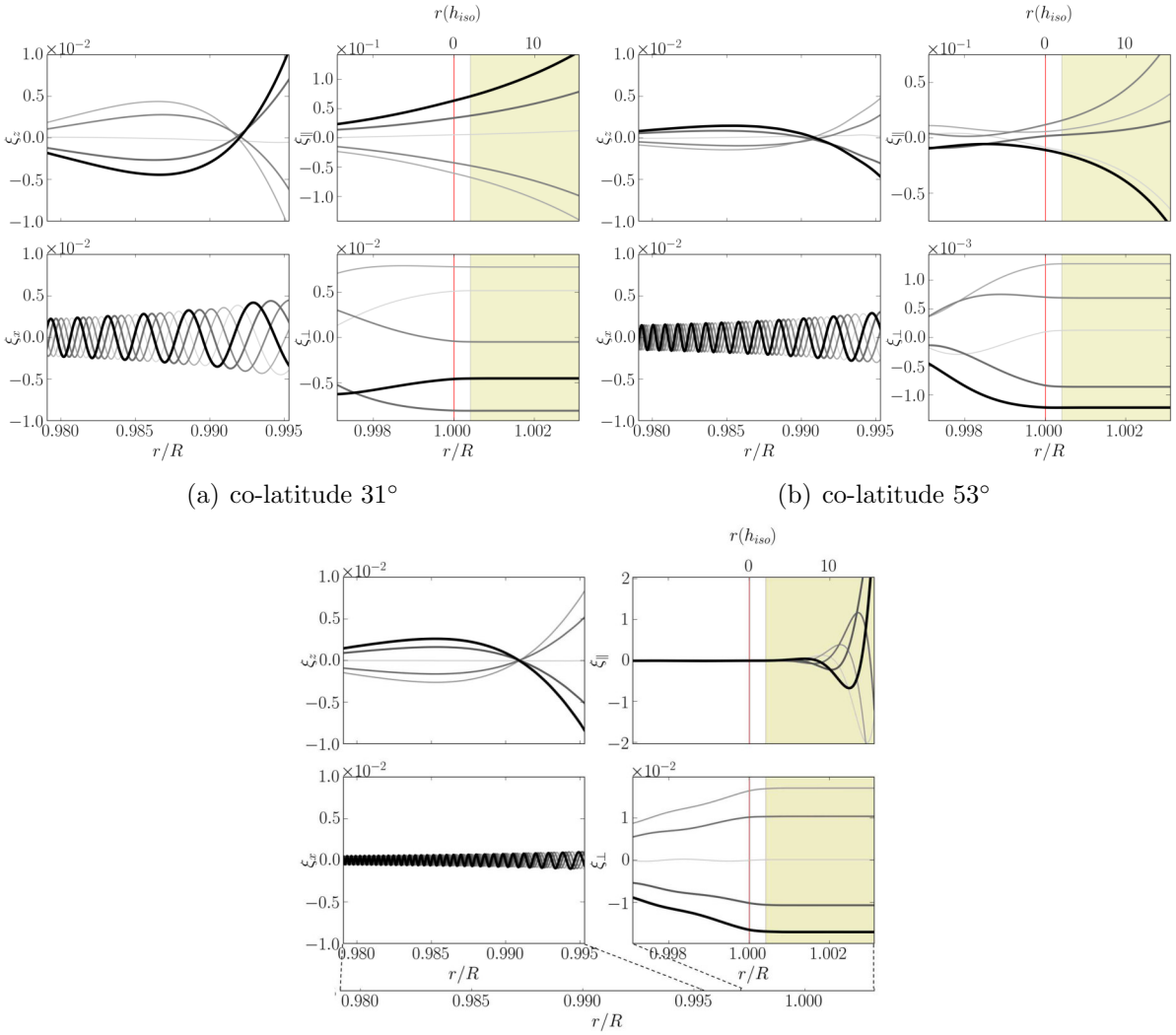

(a) co-latitude 31°

(b) co-latitude 53°

(c) co-latitude 78°

Figure 2.4: Each figure shows the displacement $\vec{\xi}$ as a function of the normalized radius (bottom x axis) in the outer 2% of the stellar model, for a frequency of 1.2 mHz with a magnetic field of 2 kG at the identified co-latitude. The left panels show the components of the displacement in the local vertical (top) and local horizontal (bottom) directions. The right panels show the displacement in the direction parallel to the magnetic field (top), and perpendicular to the magnetic field (bottom). The different curves represent different times, the yellow shadow marks the isothermal atmosphere, and the red vertical line represents the bottom of the photosphere of the star. The top x axis indicates the atmospheric height measured from the bottom of the photosphere in units of the (constant) pressure scale height of the isothermal atmosphere.

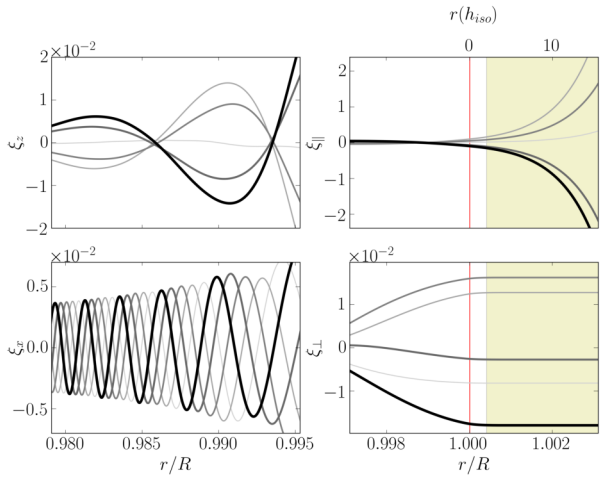

(a) co-latitude 31°

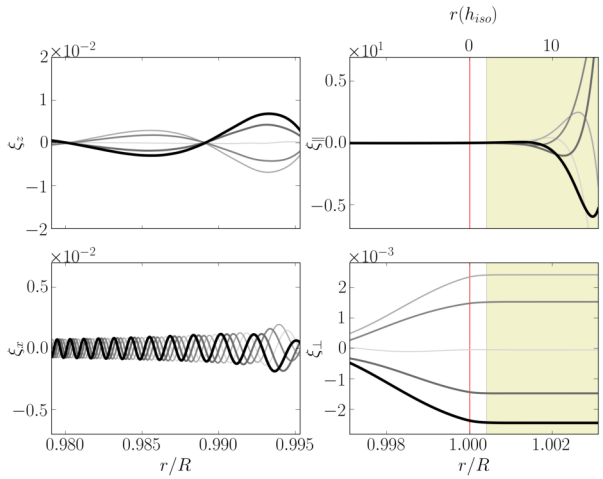

(b) co-latitude 53°

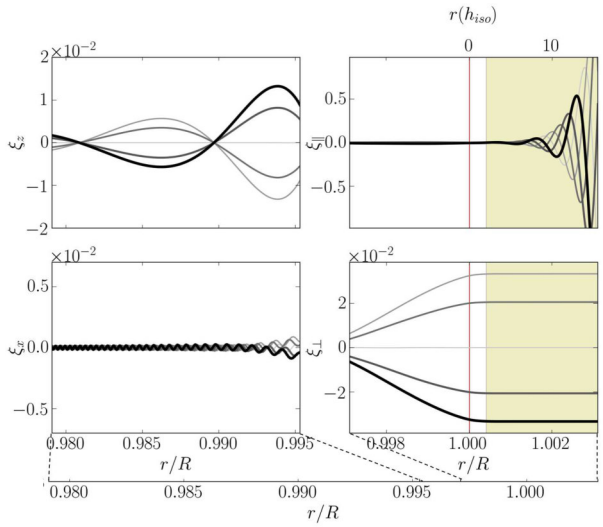

(c) co-latitude 78°

Figure 2.5: The same as Fig. 1.3 but for a frequency 2.2 mHz.

Chapter 3

Radial velocity

3.1 Radial velocities

From our oscillation model we are able to calculate the velocity field in the outer layers of the star. To obtain a measurable quantity from the velocity field, we need to transform it into radial velocities. To obtain the radial velocity as a function of the radius in the outer layers of a roAp star we need to integrate the velocity field at each specific radius, projected in the direction of the observer, over the area of interest, which may be the full visible disk, or a sub-section of it, when the elements contributing to the radial velocity measurement are concentrated in a particular region only.

In order to compute the radial velocity that an observer can measure, we define two coordinate systems, as are depicted in Fig. 3.1. The first one is to describe the oscillations in the stars, with the Z-axis aligned with the polar axis of the magnetic field, (X, Y, Z), where (r, θ, ϕ) are the associated spherical coordinates. The second one is defined by the observer, with the Z'-axis aligned with direction in which the observer is located, (X', Y', Z'), where (r, θ', ϕ') are the associated spherical coordinates. Both coordinate systems are linked by the rotational matrices,

$$R_z(\alpha) = \begin{bmatrix} \cos(\alpha) & -\sin(\alpha) & 0 \\ \sin(\alpha) & \cos(\alpha) & 0 \\ 0 & 0 & 1 \end{bmatrix}, \tag{3.1}$$

and

$$R_x(\beta) = \begin{bmatrix} 1 & 0 & 0 \\ 0 & \cos(\beta) & -\sin(\beta) \\ 0 & \sin(\beta) & \cos(\beta) \end{bmatrix}, \tag{3.2}$$

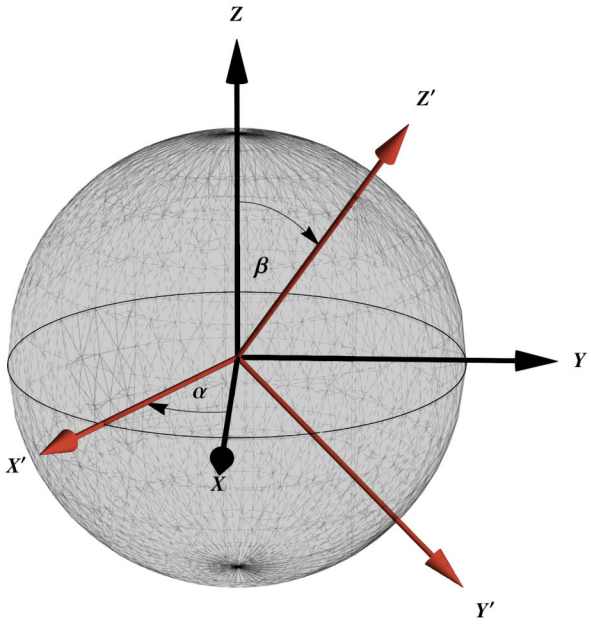

Figure 3.1: Illustration of the star, permeated by a dipolar magnetic field with identification of the Cartesian coordinates (X, Y, Z), and the spherical coordinates (r, θ, ϕ), with the Z axis in the direction of the polar axis. And a second set of Cartesian coordinates (X', Y', Z'), with the Z' axis in the direction of the observer.

in such a way that, a vector $\vec{r}'$ in the coordinate system aligned with the observer can be written in terms of the coordinate system of the star as,

$$\vec{r}' = R_z(\alpha)R_x(\beta)\vec{r}. \tag{3.3}$$

To obtain the radial velocity as a function of the radius in the outer layers of a roAp star we compute the integrated projected velocity field, considering a linear limb-darkening

law [1], using the expression (Dziembowski, 1977),

$$V_{int} = \int_{\varphi'_i}^{\varphi'_f} \int_{\theta'_i}^{\theta'_f} [v_r X_r + v_\theta X_\theta] \times C_n^{-1}(1 - a(1 - \cos\theta')) \cos\theta' \sin\theta' d\theta' d\varphi', \tag{3.4}$$

where a is the limb-darkening coefficient, for which we adopt a value of 0.46 (Claret & Hauschildt, 2003), C_n is a normalization constant from the integration of the limb-darkening in the visible disk. The angles φ'_i, φ'_f and θ'_i, θ'_f, are the integration limits, that represent a given area of the visible disk. X_r and X_θ are the projections of the unit vectors along the radial direction $\widehat{r}$ and along the polar direction $\widehat{\theta}$, onto the direction of the observer $\widehat{z'}$, respectively, defined by,

$$X_r = \widehat{z'} \cdot \widehat{r}, \tag{3.5}$$

$$X_\theta = \widehat{z'} \cdot \widehat{\theta}, \tag{3.6}$$

The velocity components v_r and v_θ are derived from the time derivative of the displacement, $\vec{v} = \frac{d}{dt}\delta\vec{r}$, where,

$$\delta\vec{r} = \left(\xi_r(r,\theta)\widehat{r} + \xi_\theta(r,\theta)\widehat{\theta}\right) e^{i\omega t} Y_l^0, \tag{3.7}$$

where, ξ_r and ξ_θ are the radial and angular (or horizontal) components of the displacement and are derived by combining the extended solutions obtained from the MAPPA code ξ_z and ξ_x, respectively, at each co-latitude. Their dependence on the polar angle, θ, is a consequence of the magnetic field which, as discussed before, influences the eigenfunction differently at different latitudes distorting the eigenfunctions from the pure spherical harmonic solutions obtained in the non-magnetic case. Moreover, since the system loses energy both from the running magnetic waves at the bottom of the magnetic boundary layer and from the acoustic running waves in the atmosphere, the eigenfrequencies and eigenfunctions become complex.

It is also important to note that the angular component of the displacement in eq. (3.7) is multiplied by the spherical harmonic instead of its derivative, as it would be expected in the non-magnetic case. This is because the horizontal movement in the

[1] We also computed the integral for the radial velocity considering, instead, the limb-darkening and line-weighting proposed by Landstreet & Mathys (2000). However, using their proposed main values for the coefficients, we did not find a significant difference when comparing to the results obtained with eq. (3.4).

magnetic stars is caused by the Lorentz force and not by the gradient of the pressure perturbation. The terms generated by the Lorentz force are dominated by the radial derivatives of the displacement and, consequently, are proportional to the spherical harmonics.

To facilitate the physical interpretation of the radial velocity V_{int}, the code allows us to separate the contributions to V_{int} of the different components of the velocity perturbation. This is done by performing the integral defined in Eq. (3.4), except that the total velocity projected in the direction of the observer that enters that integral is substituted by the projection of a single component of the velocity.

Then, to calculate the contribution to the integrated radial velocity of the parallel component of the velocity field, $V_\parallel$, we consider only the velocity field component aligned with the magnetic field in the integral. We take the extended solution for $\xi_\parallel$ and calculate its radial and angular components, thus getting,

$$V_\parallel = \int_{\phi'_i}^{\phi'_f}\int_{\theta'_i}^{\theta'_f} \left[\vec{v}_\parallel \cdot \widehat{r}\, X_r + \vec{v}_\parallel \cdot \widehat{\theta}\, X_\theta\right] \times C_n^{-1}(1 - a(1 - \cos\theta')) \cos\theta' \sin\theta' d\theta' d\varphi' \tag{3.8}$$

where,

$$\vec{v}_\parallel = \frac{d}{dt}\left(\xi_\parallel(r,\theta)\, \widehat{e}_\parallel\, e^{i\omega t} Y_l^0\right). \tag{3.9}$$

Similarly, to calculate the contribution to the integrated radial velocity of the perpendicular component of the velocity field, $V_\perp$, we consider only the velocity field component perpendicular to the magnetic field. We take the extended solution for $\xi_\perp(r,\theta)$, and calculate its radial and angular components. Thus getting,

$$V_\perp = \int_{\phi'_i}^{\phi'_f}\int_{\theta'_i}^{\theta'_f} \left[\vec{v}_\perp \cdot \widehat{r}\, X_r + \vec{v}_\perp \cdot \widehat{\theta}\, X_\theta\right] \times C_n^{-1}(1 - a(1 - \cos\theta')) \cos\theta' \sin\theta' d\theta' d\varphi'. \tag{3.10}$$

where,

$$\vec{v}_\perp = \frac{d}{dt}\left(\xi_\perp(r,\theta)\, \widehat{e}_\perp\, e^{i\omega t} Y_l^0\right). \tag{3.11}$$

The computation of $V_\parallel$ and $V_\perp$ eases the physical interpretation the results for V_{int}, because in the outer atmospheric layers the acoustic waves correspond to displacements parallel to the magnetic field while the magnetic waves correspond to displacements perpendicular to it. Moreover, we compute similar integrals considering the radial and polar components of the velocity denominating the results by V_r and V_θ, respectively.

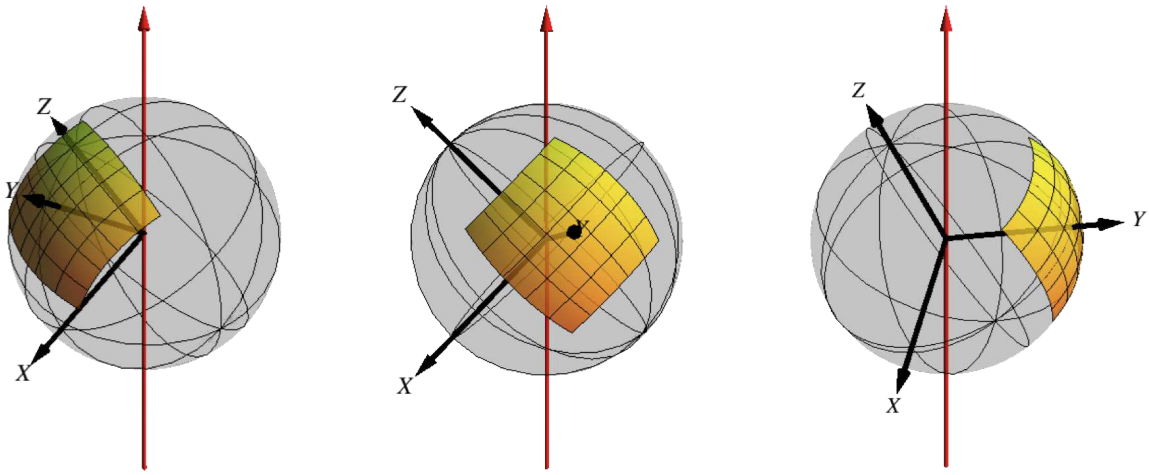

Figure 3.2: Representation of a spot in the code to calculate the radial velocity, considering the star at different rotational phases.

In summary, the code developed for this work allows us to compute the radial velocity associated to the stellar pulsations, either for the full visible disk or for part of it. Being able to define any area in the surface of the sphere, that can represent a spot or a belt of elements in the atmosphere of the star, and redefining the limits of integration, so that these always remain in the visible disk, the code makes it possible to study the pulsations for different positions of the observer, for a single spot or the full visible disk. In addition, it allows us to study the contributions to the radial velocity of the different components of the velocity field.

3.2 Results

To analyze different possible solutions, in this chapter we fix the magnetic field at 2 kG and explore four different pulsation frequencies. For each frequency we explore mode degrees from 0 to 2. In doing so, in particular by fixing the frequencies, we intentionally ignore the difference in frequency that would result from solving the eigenvalue problem for modes of different degrees. In this way, we can isolate the impact of changing the mode degree, without mixing it with the effects caused by the coupling of the magnetic and acoustic waves, and by the variation of the critical angle position, which depend on the frequency. In this chapter we explore two positions of the observer, the pole-on

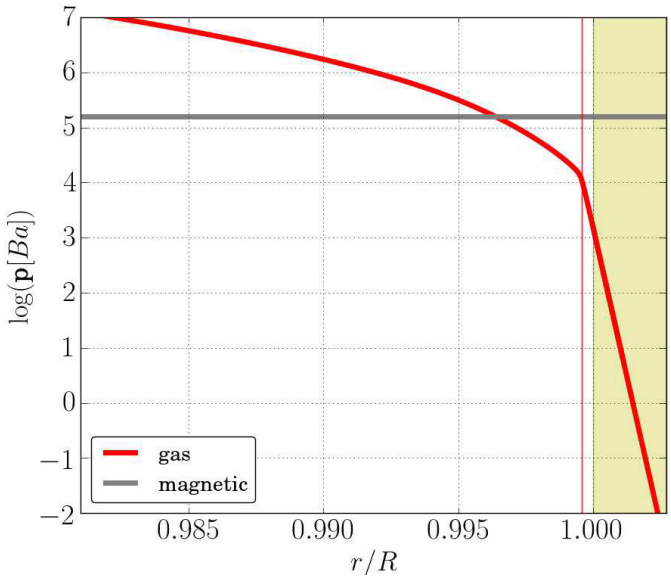

Figure 3.3: Comparison between the gas pressure (thick red line) and the magnetic pressure (grey line) in the outer 2% of the star for a magnetic field of 2 kG. The thin vertical red line marks the bottom of the photosphere.

corresponds to a rotation of $\alpha = 0$ and $\beta = 0$, and the equator-on that corresponds to a rotation $\alpha = 0$ and $\beta = \pi/2$.

For a magnetic field of 2 kG, the magnetoacoustic region in our stellar model is placed fully in the interior of the star. This is illustrated in Fig. 3.3 where the gas and magnetic pressures are compared and we can see that the region where the two have the same order of magnitude is around a normalized radius of 0.997. This means that in the atmospheric region the acoustic and magnetic waves are completely decoupled and, as discussed in the section 2.3, the acoustic waves induce displacements in the direction of the local magnetic field, and the magnetic waves in the direction perpendicularly to it.

To compare the amplitude, A_r, and phase, ϕ_r, variations of the theoretical radial velocity with those derived from observations (e.g. Ryabchikova et al. (2007b)), we match the numerical solutions in the atmosphere to a function of the type,

$$V_{int} = A_r \cos(\omega t + \phi_r). \tag{3.12}$$

3.2.1 Frequency far below the acoustic cut-off

The first frequency that we discuss, namely, 1.2 mHz, is far below the acoustic cut-off, as mentioned in section 2.4. The angle at which the critical frequency becomes smaller than

1.2 mHz is $\alpha_{cr} = 62°$. We recall that the magnetic field polar intensity is $B_p = 2$ kG, and that we will consider different cases for the same frequency, with mode degrees of $l = 0, 1, 2$ and with observers pole-on and equator-on.

The first case to be discussed for this frequency is that of a dipole mode, $l = 1$, with a pole-on observer. The results for this case are shown in Fig. 3.4. The radial velocity is shown in the left panel. The contributions of the components of the velocity parallel and perpendicular to the magnetic field to the radial velocity, defined, respectively, by eqs. (3.8) and (3.10), are presented in the top- and bottom-middle panels, respectively. The amplitude and phase variation of the radial velocity and its components are shown in the top- and bottom-right panels. In each panel the vertical red line indicates the bottom of the photosphere of the star and the shaded-yellow area represents the isothermal atmosphere. The same notation is used for all other cases.

Looking at the contributions of the parallel and perpendicular velocity components in the atmosphere of the star (middle panels), we can verify that the acoustic and magnetic waves are already decoupled, since they behave as predicted analytically by eqs. (2.10) and (2.11). We identify an exponential behavior for the parallel component, and a constant behavior for the perpendicular component. It is important to note that the amplitude of the acoustic and magnetic waves' contribution to the radial velocity (which correspond to the parallel and perpendicular contributions, respectively) are of the same order of magnitude through the whole atmosphere.

Regarding the amplitude and phase of the radial velocity for this case, shown in right panels of Fig. 3.4 we find that both the acoustic and the magnetic waves contribute to the final result. To see that, we note that the black lines show the total amplitude and phase (parameters from eq. (3.12)), derived from fitting the radial velocity; the red lines correspond to the parallel amplitude and phase, derived from the fitting of $V_{\parallel}$ and are related to the contribution of acoustic waves; the grey lines correspond to the perpendicular amplitude and phase, derived from the fitting of $V_{\perp}$, and relate to the contribution of magnetic waves. In the top-right panel, we can see that the total amplitude is simply the sum of the acoustic and magnetic waves' contribution while the total phase has a constant behavior. The perpendicular phase is always constant, due to the standing nature of the magnetic waves, while the parallel phase, related to the acoustic component, is constant due to the pole-on view that favors the area where the standing waves are located, and the low value of the frequency, that guarantees that the standing acoustic waves occupy a large area in the visible disk of the star. Because the amplitudes of the two contributions are in the same order of magnitude throughout the full atmosphere, there is no change in the dominance of the acoustic or magnetic

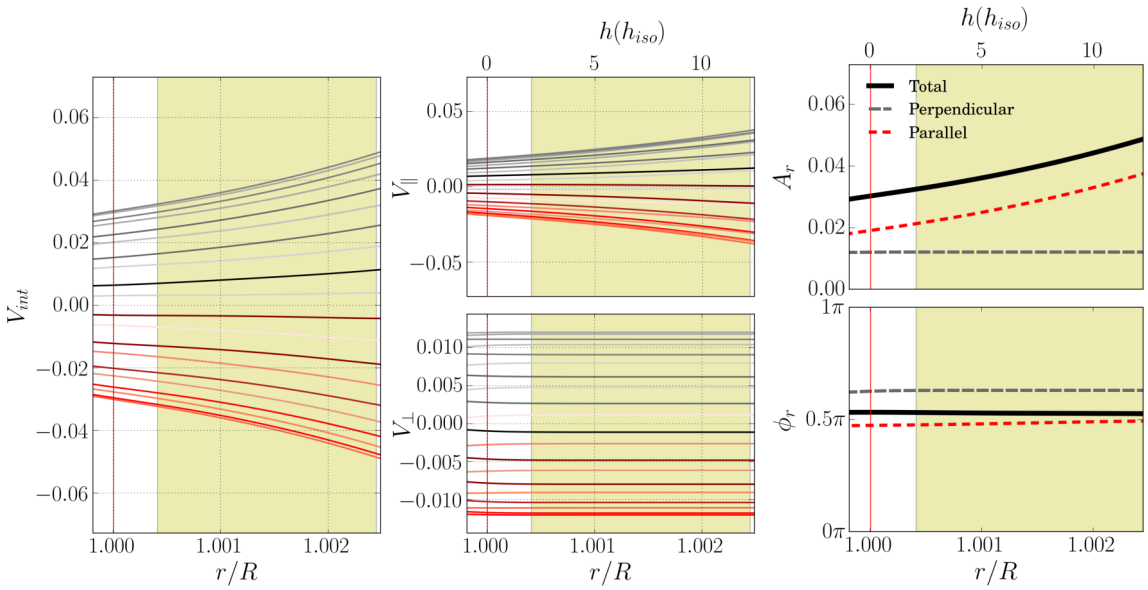

Figure 3.4: Dimensionless and normalized radial velocity. This case is for integration over the visible disk, a magnetic field of 2 kG, a mode of frequency 1.2 mHz and degree $l = 1$, and an observer pole-on. Shown in the left panel is the radial velocity as a function of the radius, at different times within the oscillatory period represented by curves of different colors. The upper middle panel shows the contribution to the radial velocity of the velocity component parallel to the magnetic field. The bottom middle panel shows the contribution to the radial velocity of the velocity component perpendicular to the magnetic field. The right panels show the amplitude (top) and the phase (bottom) of the radial velocity fitted to the function given by eq. (3.12). The radial velocity amplitude and phase are in black, the amplitude and phase derived from $V_{\parallel}$ in red, and the amplitude and phase derived from $V_{\perp}$ in grey. The labels on the top horizontal axes show the height measured from the bottom of the photosphere in units of the (constant) pressure scale height of the isothermal atmosphere. The red vertical line represents the bottom of the photosphere and the yellow shadow region represents the isothetmal atmosphere.

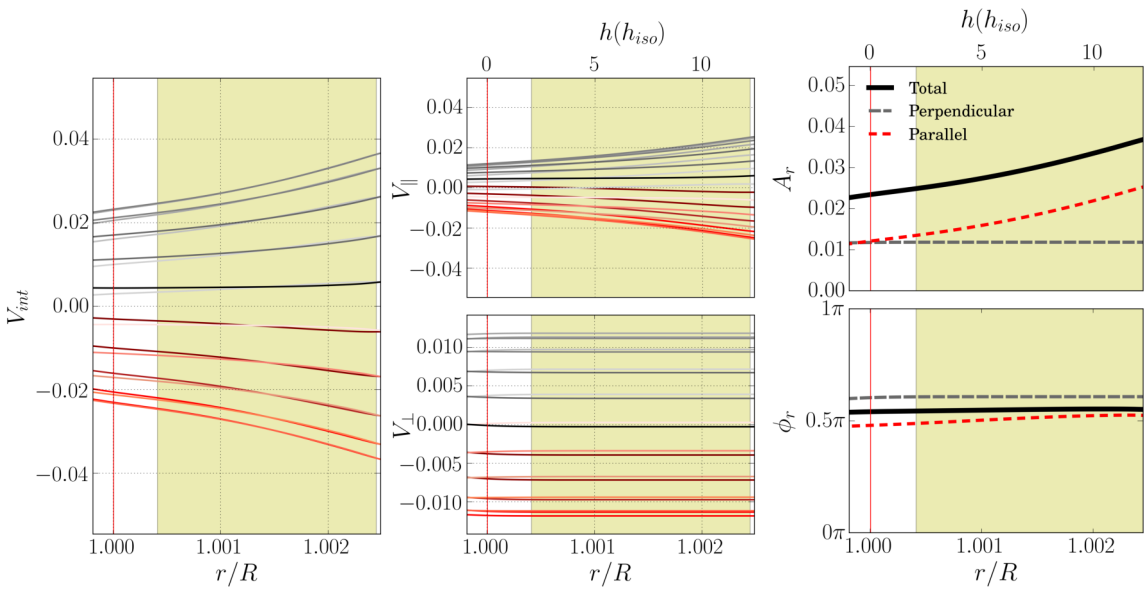

Figure 3.5: The same as Fig. 3.4 but for a mode of degree $l = 0$ and an polo-on view.

waves' contribution resulting in a constant total phase. We do not discuss the case of the equator-on observer for the $l = 1$ mode as it is anti-symmetrical and, thus, it completely cancels out.

The second case that we discuss is that of a spherically-symmetric mode, $l = 0$, with a pole-on observer, presented in Fig. 3.5. The behavior of the radial velocity does not change significantly from that found for the $l = 1$ mode, because the spherically-symmetric mode and the dipolar mode seen from the pole are relatively similar. This case also shows a constant phase and a constructive interaction[2] between the acoustic and magnetic waves. But when we inspect the radial velocity for the equator-on view, shown in Fig. 3.6, we see that the radial velocity (left panel) differs from that found for a pole-on observer, in that now we find a modulation in the exponential behavior. Inspecting the contributions of the acoustic and magnetic waves (middle panels), we can see that they are of the same order of magnitude, as in the previous cases, but this time the acoustic wave's contribution shows the same amplitude modulation as that found for the radial velocity. From the right panels of Fig. 3.6, we see that the total amplitude behaves as in the previous cases. However, now the total phase varies significantly throughout the atmosphere. This variation results from the contribution of the acoustic waves, particularly because an observer that is equator-on looks directly at the region where the traveling acoustic waves are found.

[2]Here, the words constructive interaction are used to indicate that the contributions of the two waves to the integral defining V_{int} have the same sign at any given time.

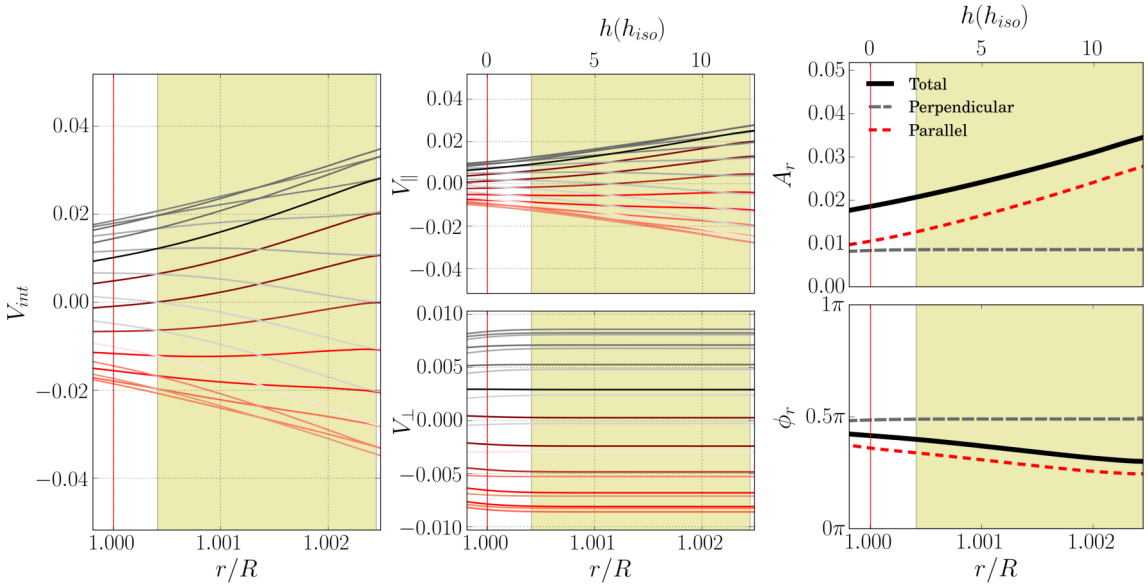

Figure 3.6: The same as Fig. 3.4 but for a mode of degree $l = 0$ and an equator-on view.

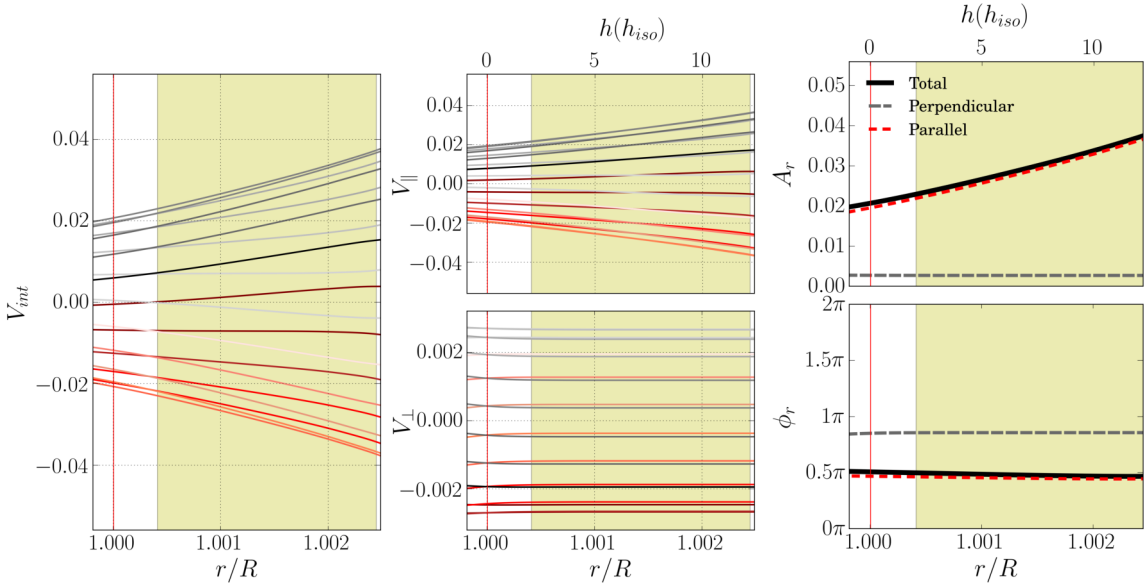

Figure 3.7: The same as Fig. 3.4 but for a mode of degree $l = 2$.

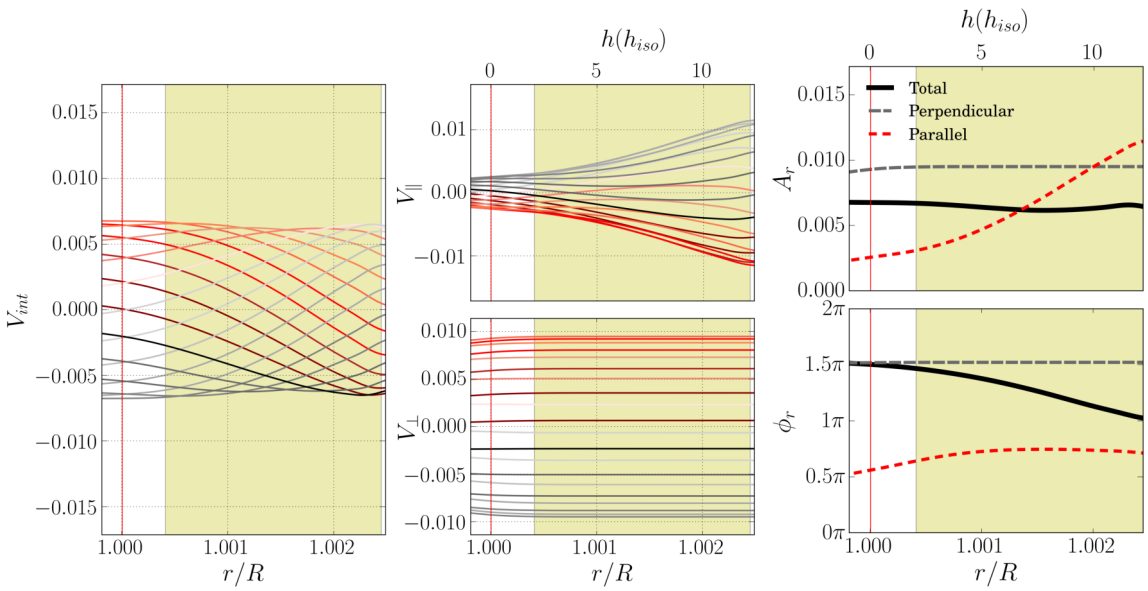

Figure 3.8: The same as Fig. 3.4 but for a mode of degree $l = 2$, and an equator-on view.

We now turn to the case of a quadrupolar mode, i.e., a mode of degree $l = 2$, whose results are shown in Fig. 3.7 (pole-on view) and 3.8 (equator-on view). The behavior in this case is different from what has been found so far, because the shape of the quadrupole suppresses the waves in the middle of the hemispheres.

For the pole-on view (Fig. 3.7), the radial velocity (left panel) looks similar to the previous cases. However, looking at the contributions of the acoustic and magnetic waves' (middle panel), we see that they differ by one order or magnitude. This is because from a pole-on view the magnetic waves that have velocities in the direction of the observer are found at co-latitudes around 45^o, which is the region suppressed by the geometry of the $l = 2$, axisymmetric, spherical harmonic. As a consequence, the magnetic contribution decreases significantly and the radial velocity is dominated by the acoustic waves. The dominance is clear in the plots of the amplitude and phase (right panels), in which we can see that the total amplitude and the total phase follow the amplitude and phase of the acoustic wave contribution.

Next we look at the radial velocity for the mode of degree $l = 2$ with an equator-on view (Fig. 3.8). The behavior in this case is very different, because from this observer's point of view there is an important cancellation of the acoustic wave's contribution, resulting in an almost constant amplitude for the radial velocity. Comparing the acoustic and magnetic waves' contributions (middle panels), we can see from the colors that represent the different times, that the two contributions are significantly out of phase, in contrast with the previous cases. As a result, the parallel and perpendicular amplitudes

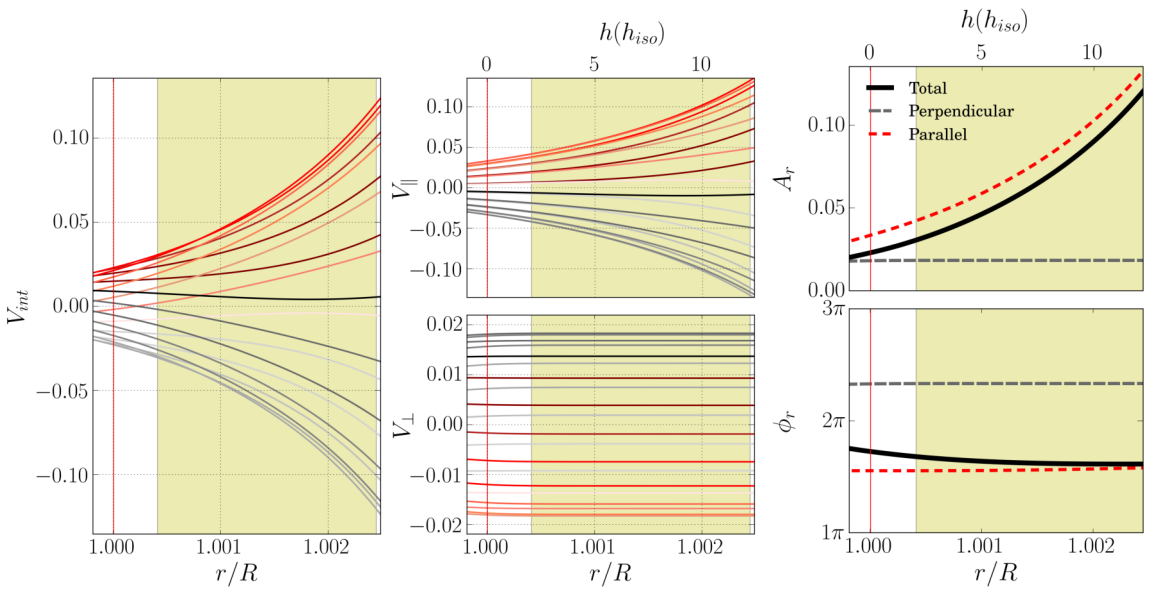

Figure 3.9: The same as Fig. 3.4 but for a mode of frequency 1.7 mHz and degree $l = 1$, a magnetic field of 2 kG, and an observer pole-on.

(top-right panel) interact destructively [3] leaving the total amplitude in between the two in the inner atmosphere, while in the upper atmosphere the acoustic waves start to dominate, due to the exponential behavior of their amplitudes. Moreover, in the total phase (bottom-right panel) we see a large variation caused by the change in the dominance from the acoustic to the magnetic waves, as we move down into the atmosphere, giving rise to a large amplitude modulation also in the radial velocity (left panel).

3.2.2 Frequency below the acoustic cut-off

The second frequency to be discussed has a value of 1.7 mHz. At this particular frequency the critical angle is $\alpha_{cr} = 50°$, meaning that for co-latitudes larger than this angle the acoustic waves change from having a standing character to having a running character. The magnetic field polar intensity is kept at 2 kG.

The first results shown for this frequency concern a dipolar mode, $l = 1$, with an observer pole-on. The corresponding radial velocity is shown in Fig. 3.9. The contributions of the parallel and perpendicular components to the radial velocity integral are similar in magnitude, although the acoustic waves become progressively dominant with increasing atmospheric height.

As we can see from the top-right panel (Fig. 3.9), the total amplitude follows the

[3]Here, the words destructive interaction are used to indicate that the contributions of the two waves to the integral defining V_{int} have the opposite sign at any given time.

behavior of the parallel amplitude, related to the contribution of acoustic waves (red line). It is, however, always smaller than the parallel amplitude because of the contribution from the magnetic waves, (gray line) which is out of phase with the first. In the bottom-right panel, we see that the total phase (black line) follows relatively closely the parallel (acoustic) phase (red line) in the outermost layers, but diverges from it in the lower atmospheric region due to the increasing impact of the perpendicular (magnetic) phase. Despite this, the phase variation across the whole atmosphere is small.

This is a clear case in which the phase variation in the radial velocity results from the competition between the acoustic and magnetic components that enter the integral, rather than from an actual phase variation in either of them. As mentioned earlier, the perpendicular phase is always constant, due to the standing nature of the magnetic waves, while the parallel phase is constant due to the pole-on view, that favours the area where the standing waves are located, and the low value of the frequency, that guarantees that the standing acoustic waves occupy a larger area in the visible disk of the star than the acoustic running waves.

Here, and in all cases that follow, we shall not show the analysis of the radial modes with a pole-on observer, because we find that the results for that case are always very similar to those found for the dipole modes and the same observer (for the reasons explained in sec. 3.2.1). Thus, the second case illustrated the for frequency of 1.7 mHz is the spherically-symmetric mode, $l = 0$, with an observer equator-on. The radial velocity is shown in Fig. 3.10, left panel. The amplitudes of the acoustic and magnetic waves' contributions (Fig. 3.10, middle panels) are of the same order of magnitude in the lower half of the atmosphere, just as was found for the dipolar mode, although here the two contributions actually become comparable near the photosphere, as seen from the right upper panel. But the main difference with respect to the case of $l = 1$ is the behavior of the phase. Looking at Fig. 3.10, lower right panel, we see that just as for the $l = 1$ mode, the total phase (black line) follows the parallel phase (red line) in the outermost layers, but diverges from it as one approaches deeper regions of the atmosphere, due to the influence of the magnetic waves. However, contrary to case of $l = 1$, the parallel phase (red line) now varies with depth, due to the contribution of the acoustic running waves that are concentrated towards the equator, where the observer is positioned. As a result, the total phase varies also in the outer atmospheric region.

The case of the quadrupole mode, $l = 2$, with a pole-on view, is illustrated in Fig. 3.11 (a). Comparing the contributions from the acoustic and magnetic waves, top- and bottom-middle panel, respectively, we notice the differences in the order of magnitude between them. As explained before, this difference arises because the quadrupole mode

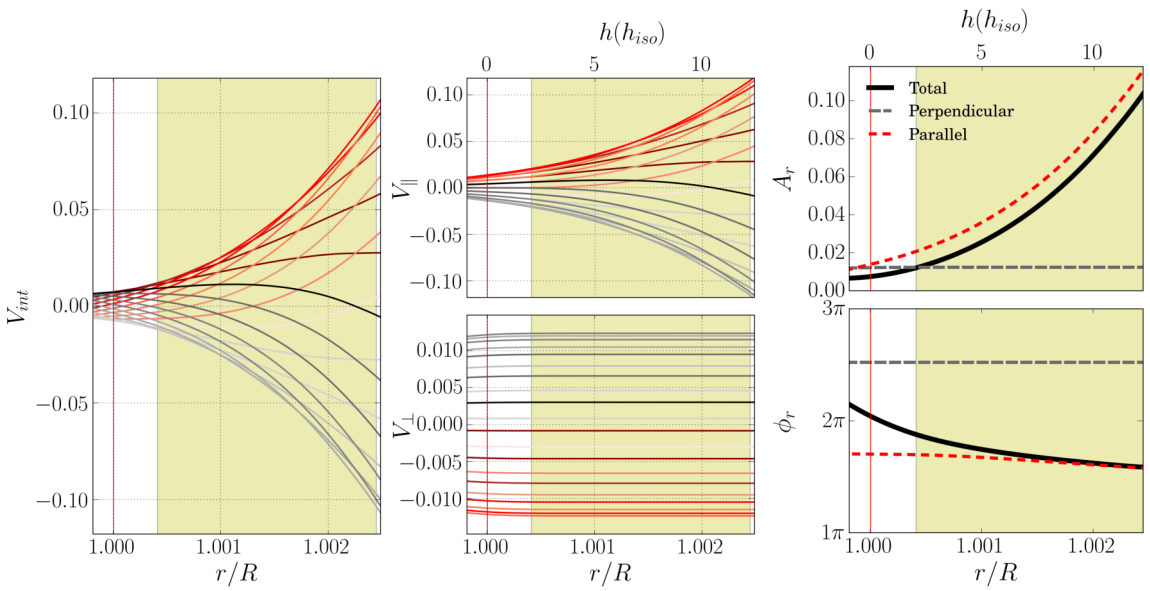

Figure 3.10: The same as Fig. 3.4 but for a mode of frequency 1.7 mHz and degree $l = 0$, and an observer equator-on.

cancels out the contribution of the magnetic waves that are more closely in the direction of the observer, that are around the co-latitude of 45^o. As a consequence the radial velocity (left-panel), has the same shape as the acoustic wave's contribution. We can confirm this by inspecting the right-panels of the same figure. The total amplitude (black line, top-panel) and the parallel amplitude (red line, top-panel) overlap. Something similar happens with the total phase (black line, bottom-panel), that follows the parallel phase (red line, bottom-panel) in the upper atmosphere, beginning to deviate slightly only as we get close to the bottom of the photosphere, demonstrating the complete dominance of the acoustic waves in this case.

On the contrary, the case of a quadrupole mode with an equator-on view, has a stronger contribution from the magnetic waves in the inner half of the atmosphere, as seen from Fig. 3.11 (b). Just as in the case of the lower frequency, with the same mode degree and observer, the radial velocity (left panel), does not follow the exponential shape of the acoustic wave's contribution seen in most of the previous cases, because in this case, it is the acoustic waves moving in the direction of the observer that are in the area where the quadrupole mode has its nodes (around co-latitude 45^o). The cancellation of the acoustic waves has a significant impact not only in the amplitude but also in the shape of the acoustic wave's contribution (middle-top panel). As a result, both the magnetic and acoustic contributions are relatively flat in the inner atmospheric region.

By inspecting the amplitude and phase variation (right panels), we can see that the

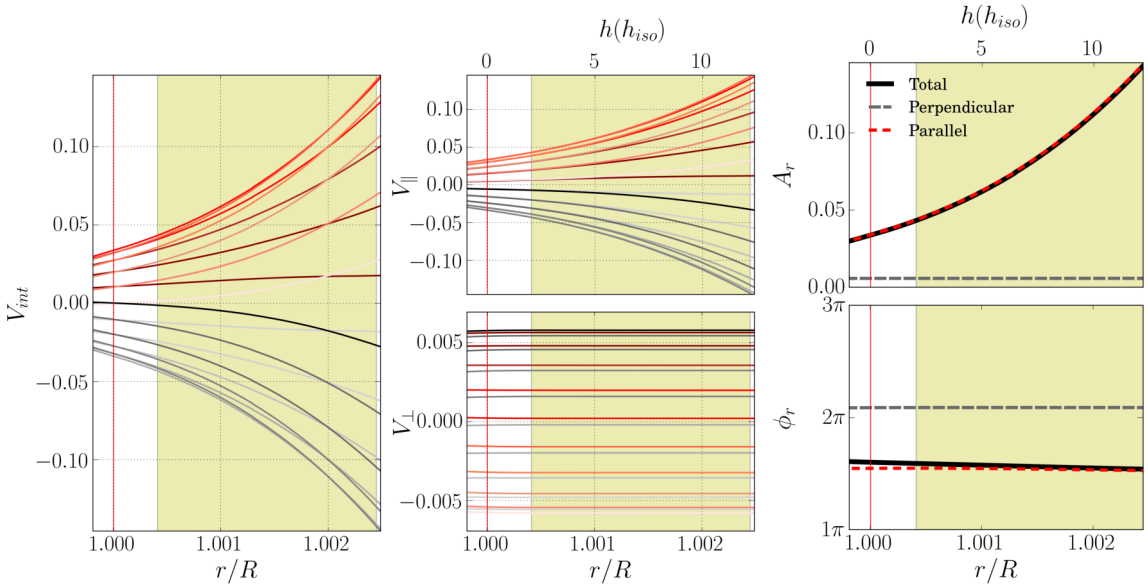

(a) pole-on view

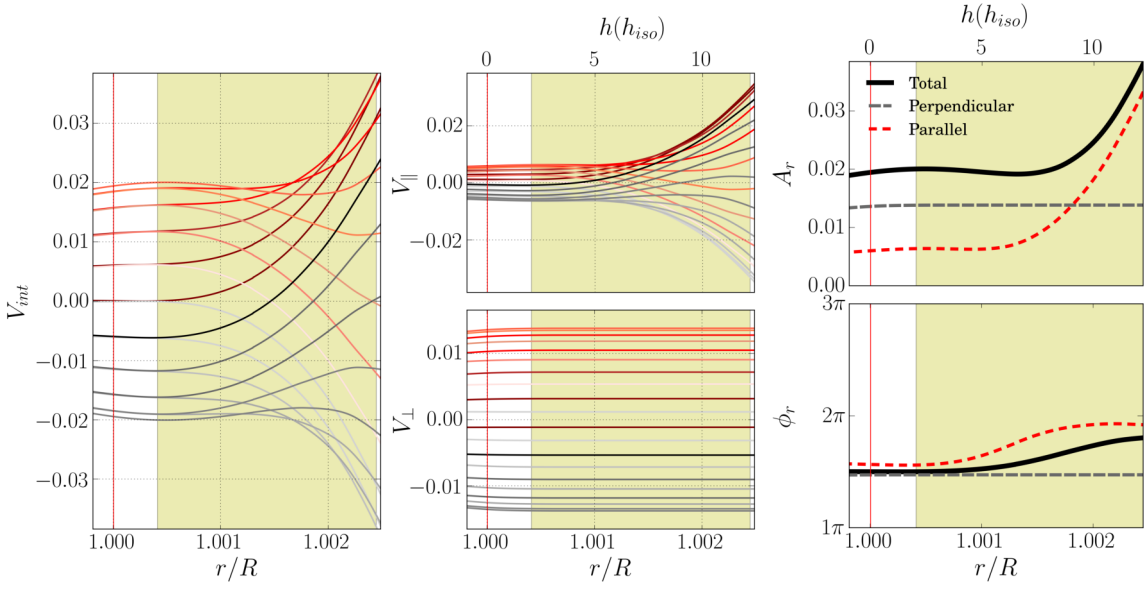

(b) equator-on view

Figure 3.11: The same as Fig. 3.4 but for a mode of frequency 1.7 mHz and degree $l = 2$: figure (a) with a pole-on view and figure (b) with an equator-on view.

total phase (black line) follows the perpendicular phase (grey line) in the lower part of the atmosphere but moves away from it in the middle of the isothermal atmosphere towards the parallel phase (red line). As for the total amplitude (black line - upper panel), in the inner half of the atmosphere shows the effect of a constructive superposition of the flat profiles of the two contributions, while in the upper part of the atmosphere begins to follow the parallel amplitude.

Comparing with the frequency of 1.2 mHz with the same degree an view, we can note that in the inner atmosphere the behaviour is similar in the two cases, but in the upper atmosphere the two start to differ, due to the higher amplitude that is reached by the acoustic waves when the frequency increases. This higher amplitude results from the fact that the critical angle is smaller for the higher frequency.

3.2.3 Frequency close to the acoustic cut-off

Next we consider a frequency of 2.2 mHz that is below the acoustic cut-off, but close to it. As mentioned in section 2.4, the angle at which the critical frequency becomes smaller than 2.2 mHz is $\alpha_{cr} = 33°$.

The radial velocity for the mode of degree $l = 1$, with an observer pole-on, is shown on the left panel of Fig. 3.12, and the contributions to it from the components of the velocity parallel and perpendicular to the magnetic field are shown on the middle panels, in the same way as for the previous case. We see, from the middle panels, the exponential behavior of the acoustic wave's contribution (top-middle) in the atmosphere of the star, and the constant amplitude of the magnetic wave's contribution (bottom-middle), but this time the amplitudes of the two contributions differ more significantly in the high atmosphere. This is because for the present frequency the fraction of the visible disk covered with acoustic running waves is larger than for the previous frequencies, and the amplitude of the displacement, hence also of the velocity, increases faster with height for running acoustic waves than for standing acoustic waves (as discussed in section 2.3). In the present case the acoustic contribution to the integral of the radial velocity becomes more dominant in the high atmosphere.

The amplitude and phase of the radial velocity are shown in the right panels of Fig. 3.12. In the outermost layers the total amplitude (black line, top panel) follows the acoustic wave's contribution (red line), but, when moving towards lower atmospheric layers the magnetic wave's contribution (gray line) becomes increasingly important. This behavior can be seen also in the phase (bottom panel), as the total phase (black line) follows the phase from the acoustic wave's contribution (red line) in the outer layers,

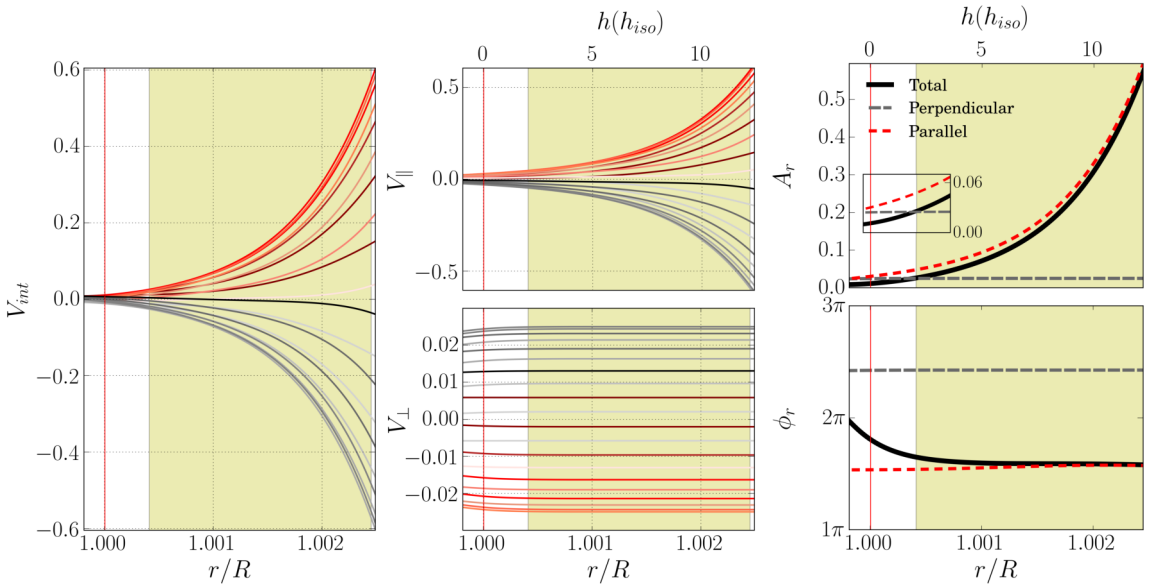

Figure 3.12: The same as Fig. 3.4 but for a mode of frequency 2.2 mHz and degree $l = 1$, a magnetic field of 2 kG, and an observer pole-on.

but approaches the phase of the magnetic wave's (gray line) contribution deeper in. Unlike in the previous frequencies for $l = 1$ and a pole-on view, here we can see a very small variation in the phase of the acoustic contribution (red line) which is due to the higher frequency of the mode considered that results in a more significant contribution of acoustic running waves to the integral of the parallel component. Nevertheless, the dominant phase variation in the radial velocity (black line) results from the competition between the contributions to the radial velocity integral of the parallel (acoustic) and perpendicular (magnetic) velocity components, as in the previous case.

The second case considered for this frequency is for a mode of degree $l = 0$ and an observer equator-on. The radial velocity is shown in Fig. 3.13, left panel, and the acoustic and magnetic waves' contributions are shown in the top- and bottom-middle panels, respectively. In the outer atmospheric layers, the two contributions differ by one order of magnitude. Thus, the acoustic waves are dominant in those layers. While this is similar to the previous case, here we can see a modulation with height of the exponential behavior in the atmosphere. This is due to the fact that in this case the observer is looking more directly at the acoustic running waves.

The amplitude and phase variations of the radial velocity are shown in Fig. 3.13, right panels, where again we have the total amplitude (black line, top panel) dominated by the amplitude derived from the acoustic wave's contribution (red line, same panel) in the high atmosphere, and a total phase (black line, bottom panel) that changes from following

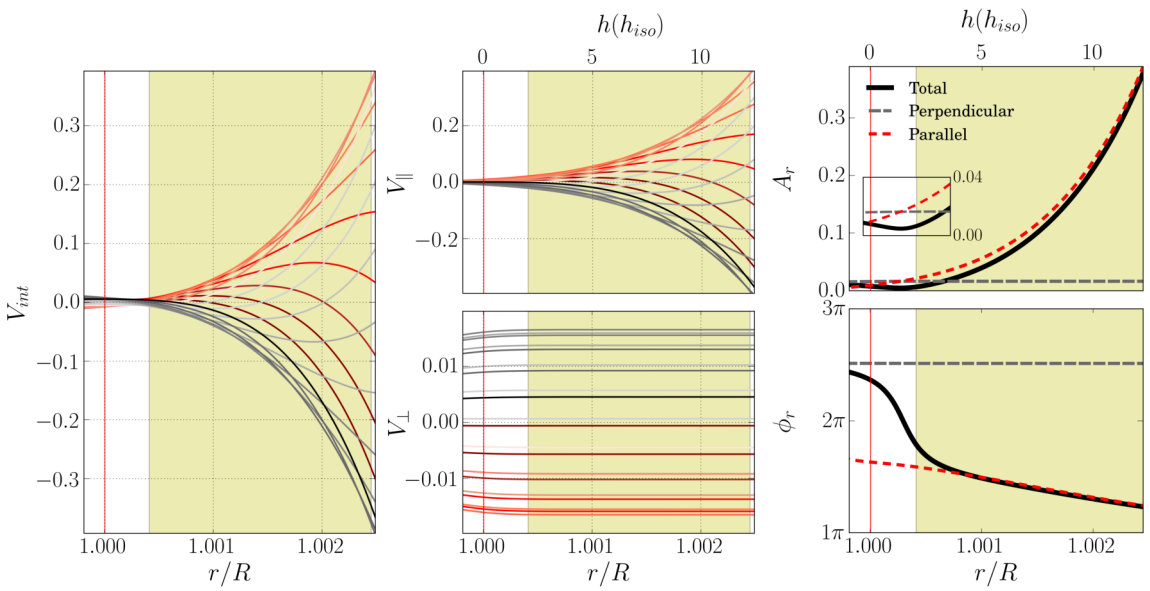

Figure 3.13: The same as Fig. 3.4 but for a mode of frequency 2.2 mHz and degree $l = 0$, a magnetic field of 2 kG, and an observer equator-on.

the phase derived from the acoustic wave's contribution in the high atmosphere (red line, same panel) to following the phase derived from the magnetic wave's contribution (gray line, same panel) in the inner layers of the atmosphere. The change in the phase is evident and much greater than the phase variation seen in the case of the pole-on view and $l = 1$ mode (which is similar to the not shown case of the pole-on view $l = 0$ mode, as mention earlier). This is again because with the pole-on view the observer is looking directly at the acoustic standing waves at the pole, but with the equator-on view the observer is looking directly at the acoustic running waves in the equator.

The case of a quadrupole mode, $l = 2$, with a pole-on view, is illustrated in Fig. 3.14 (a). Looking at the contribution of the acoustic and magnetic waves, top- and bottom-middle panel, respectively, we can see once again a very significant difference between the two contributions, because for this mode there is a cancellation of the magnetic waves that are in the direction of the observer. Thus, the radial velocity (left-panel) and the acoustic wave's contribution (top-middle panel) are essentially the same. This can also be seen in right-panels, where the total amplitude (black line top-panel) and the parallel amplitude (red line top-panel) overlap. Something similar happens with the total phase (black line bottom-panel), that follows the parallel phase (red line bottom-panel) almost throughout the entire atmosphere. Another interesting feature is that the parallel phase shows only a very small variation, hence, the total phase is almost constant. So, in this case we have a high frequency mode with a constant phase.

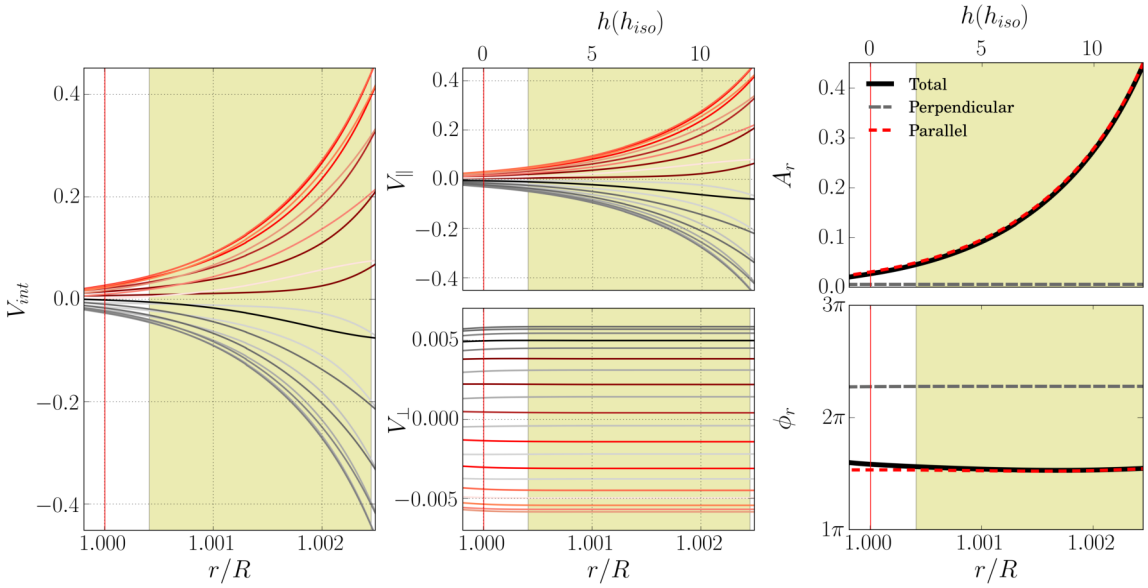

(a) pole-on view

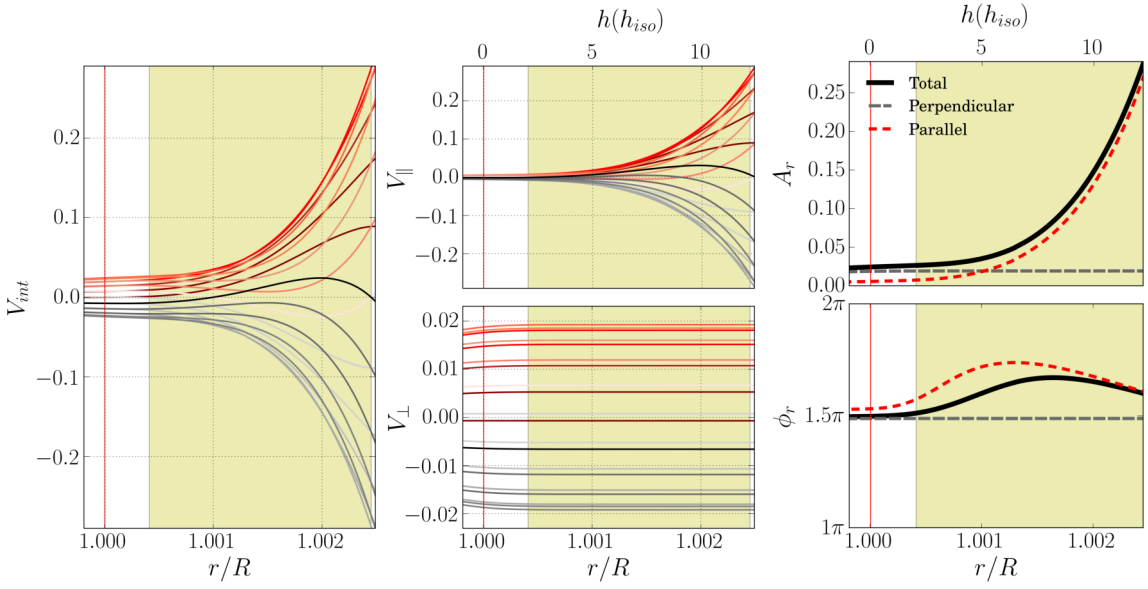

(b) equator-on view

Figure 3.14: The same as Fig. 3.4 but for a mode of frequency 2.2 mHz and degree $l = 2$, a magnetic field of 2 kG: figure (a) with a pole-on view and figure (b) with an equator-on view.

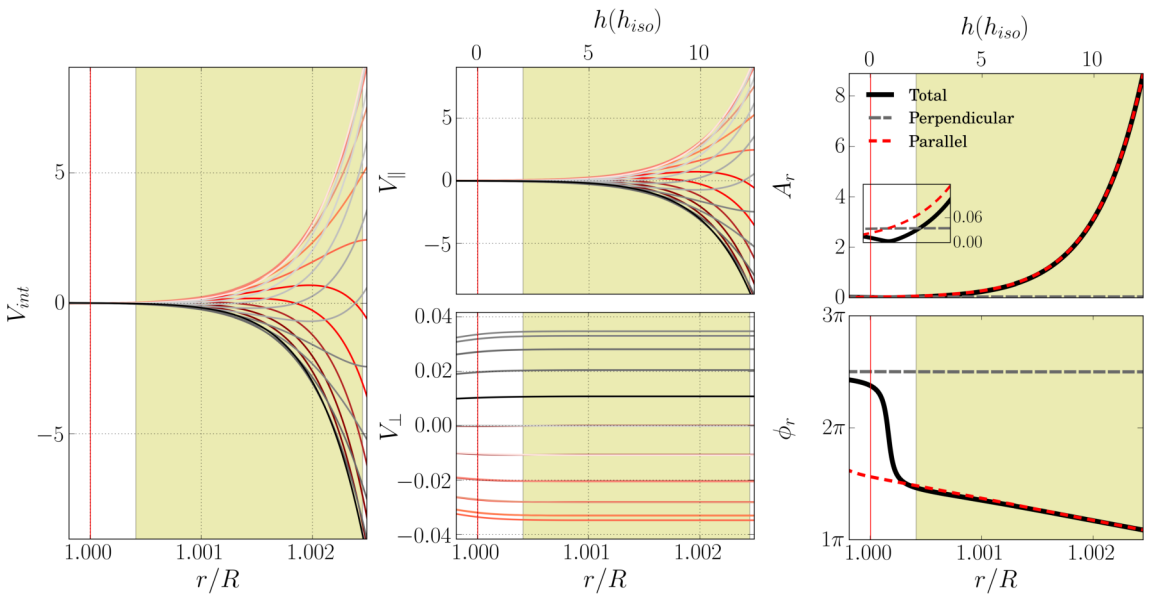

Figure 3.15: The same as Fig. 3.4 but for a mode of frequency 2.7 mHz and degree $l = 1$, a magnetic field of 2 kG, and an observer pole-on.

The case of a quadrupole mode, $l = 2$, with an equator-on view is presented in Fig. 3.14 (b). In the results for the radial velocity (left panel) for this case the exponential shape of the acoustic wave's contribution can bee seen only in the outer atmosphere, while in the inner atmosphere, the constant amplitude of the magnetic wave's contribution can be recognized. This is because again, the acoustic waves moving in the direction of the observer are around the region where the quadrupole mode has its node.

By inspecting the amplitude and phase variation (right panels), we can see that the total phase (black line) follows the perpendicular phase (grey line) down in the atmosphere but moves away from it in the isothermal atmosphere towards the parallel phase (red line). This can also be seen in the total amplitude (black line - upper panel), while in the upper part of the atmosphere begins to follow the parallel amplitude. The difference with the previous cases of $l = 2$ modes with an equator-on view is seen mostly in the outer atmospheric layers and is due to the fact that with a larger frequency the acoustic waves dominate more significantly in those layers, given the greater contribution of the running waves.

3.2.4 Frequency above the acoustic cut-off

The fourth frequency to be considered is one above the acoustic cut-off, namely, a frequency of 2.7 mHz (cut-off frequency of the star in Table 2.1). The radial velocity for the case of an $l = 1$ mode with pole-on view is shown in Fig. 3.15, left panel. Since the mode

frequency is above the acoustic cut-off, the acoustic running waves are present in the full visible disk. Due to the faster increase with height of the acoustic running waves, the amplitudes of the acoustic wave's contribution (top-middle panel) and magnetic wave's contribution (bottom-middle panel) differ by two orders of magnitude in the outermost layers, leading to a total dominance of the acoustic waves in that part of the atmosphere.

The variations in the amplitude and phase for this case are shown in Fig. 3.15, top- and bottom-right panels, respectively. The variations in the total amplitude and the total phase (black lines) show the dominance of the acoustic wave's contribution (red line) throughout the isothermal atmosphere. In that region we can see a significant variation of the parallel phase caused by the running acoustic waves. In the inner atmosphere, where the magnetic and acoustic contributions have the same order of magnitude, we can identify a crossing between the acoustic (red line) and the magnetic wave's contributions (gray line). Together with the abrupt variation in the total phase (black line) this marks the transition between the dominance of the two types of waves in the radial velocity integral. Because they are out of phase, this crossing generates an apparent node in the inner atmosphere.

The second case presented for this frequency is that of a spherically-symmetric mode, $l = 0$, with an equator-on observer. The radial velocity, seen in Fig. 3.16, left panel, shows a fast exponential growth, which is modulated with height, since the acoustic running waves are present in the full visible disk. From inspection of Fig. 3.16, middle panels, we can see, as for the previous frequency of 2.2 mHz, that the contribution from the acoustic wave to the radial velocity dominates throughout most of the atmosphere, with the exception of the innermost layers.

Figure 3.16, right panels, shows the amplitude and phase variations for this case. We see a very significant phase variation (black line, bottom panel) in the isothermal atmosphere, which is mainly due to the contribution of the acoustic running waves (red line, same panel). A significant phase variation was already seen in the previous case presented for this frequency, with a pole-on observer, but it is even more significant here. This is because the acoustic running waves near the equator are propagating almost perpendicularly to the equator-on observer. Therefore, their wavenumber projection into the line-of-sight direction is very large, resulting in rapid height-variations in the center of the visible disk, which contribute significantly to the radial velocity integral. As before, in these layers the total amplitude (black line, top panel) is dominated by the acoustic wave's contribution (red line, same panel). In the inner atmosphere we can identify a jump of π, caused by the change in the dominant contribution, from acoustic in the outer layers to magnetic in the inner layers. A phase jump had already been seen in the first

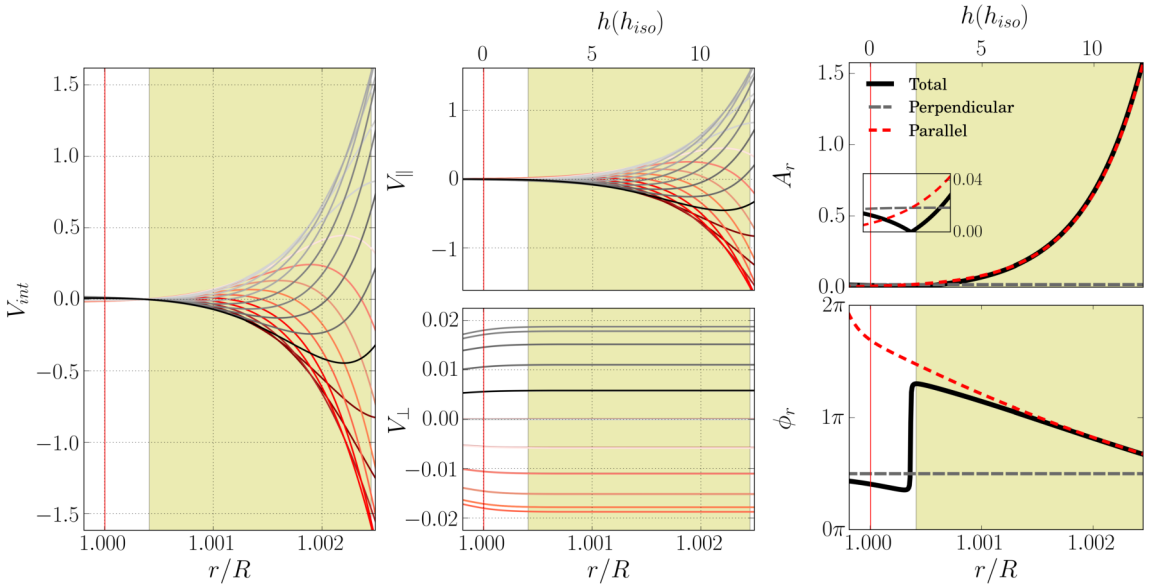

Figure 3.16: The same as Fig. 3.4 but for a mode of frequency 2.7 mHz and degree $l = 0$, a magnetic field of 2 kG, and an observer equator-on.

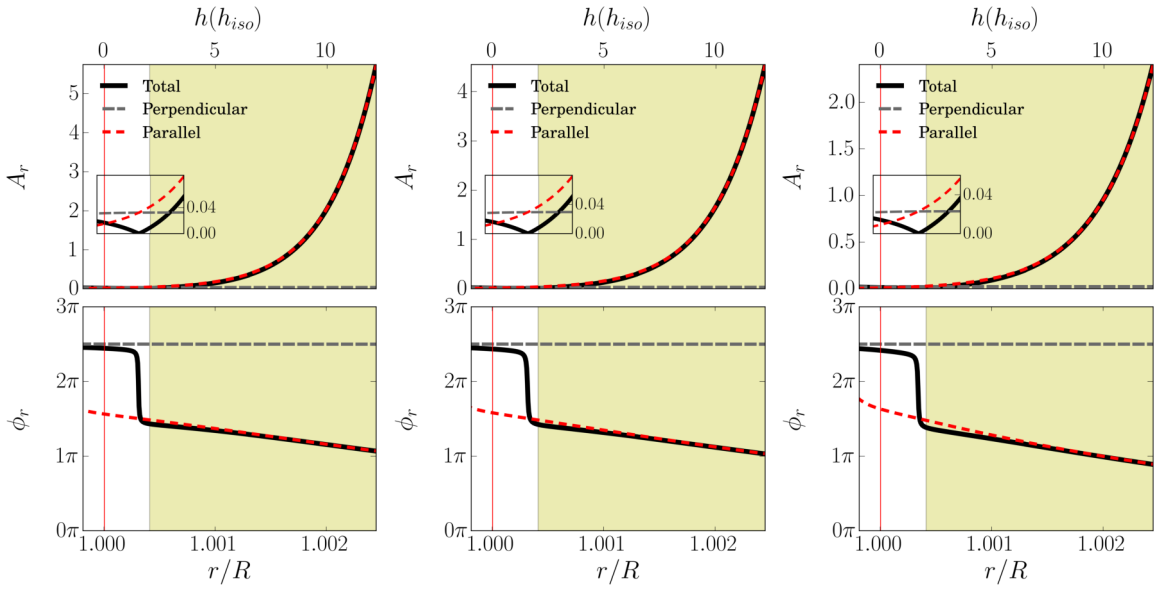

(a) pole-on view (b) view from 30^o of the pole (c) view from 60^o of the pole

Figure 3.17: The amplitude (top) and the phase (bottom) of the radial velocity fitted to the function given by eq. (3.12). Line colors and styles have the same meaning as in the previous figures. This series of plots show for a mode of frequency 2.7 mHz and degree $l = 0$, the results for different positions of the observer (as labeled).

case presented for this frequency, but in this case the change is sharper. This is because here the magnetic and acoustic contributions are completely out of phase.

We can verified looking at in Fig. 3.17, that this particular apparent node for a mode with a frequency of 2.7 mHz and degree $l = 0$ can be seen from any observation angle, although its exact position changes slightly with the observer's view.

The case of a quadrupole mode with a pole-on view is illustrated in Fig. 3.18(a). Looking at the contribution from the acoustic and magnetic waves, top- and bottom-middle panel, respectively, we can see a very significant difference in their order of magnitude similarly to the previous cases of a $l = 2$, pole-on view. Thus, the radial velocity (left-panel) and the acoustic wave's contribution (top-middle panel) are the same. This can also be seen in the right-panels, where the total amplitude (black line top-panel) and the parallel amplitude (red line top-panel) overlap. Something similar happens with the total phase (black line bottom-panel), that follows the parallel phase (red line bottom-panel) throughout the entire atmosphere. In this case, the acoustic waves dominate in the entire atmosphere, not only because with this observer the magnetic waves are hardly detectable, but also because with a higher frequency, larger amplitudes are reached by the acoustic contribution to the radial velocity.

The quadrupole mode, $l = 2$ with an equator-on view is presented in Fig. 3.18(b). The radial velocity (left panel), differs from the other cases with $l = 2$ and equator-on view, because in the innermost part of the atmosphere we still can see a constant behavior, but, for this frequency the exponential shape of the acoustic wave's contribution appears right from the lower atmospheric regions. The reason for this is that for a frequency above the acoustic cut-off the amplitude of the acoustic waves is much higher than the amplitude of the magnetic waves, thus, the acoustic wave's contribution dominates throughout most of the atmosphere even for this combination of mode degree and observer's position, where the spherical harmonic node tends to cancel the region where the acoustic modes contribute the most. Only in the innermost part of the atmosphere we can see a small differences between the radial velocity and the acoustic wave's contribution.

By inspecting the amplitude and phase variation (right panels), we can confirm the dominance of the acoustic waves, since, the total amplitude (black line - upper panel) follows the parallel amplitude (red line). We can see also that the total phase (black line) follows the parallel phase (red line) but in the innermost layers of the atmosphere the total phase starts to follows the perpendicular phase (grey line), meaning that the dominance deep enough does change from acoustic to magnetic.

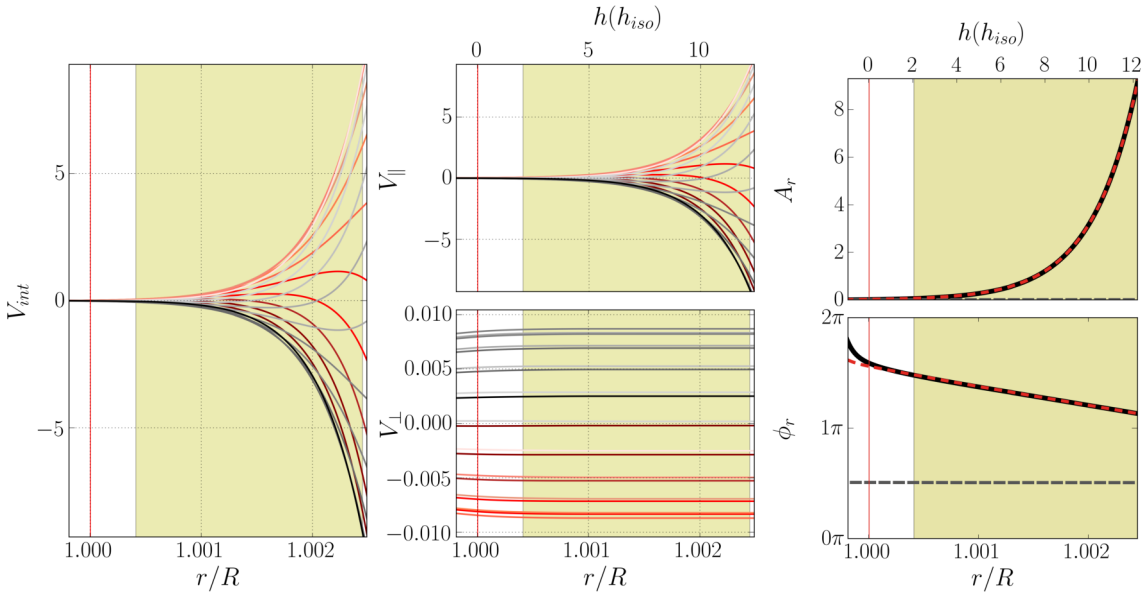

(a) pole-on view

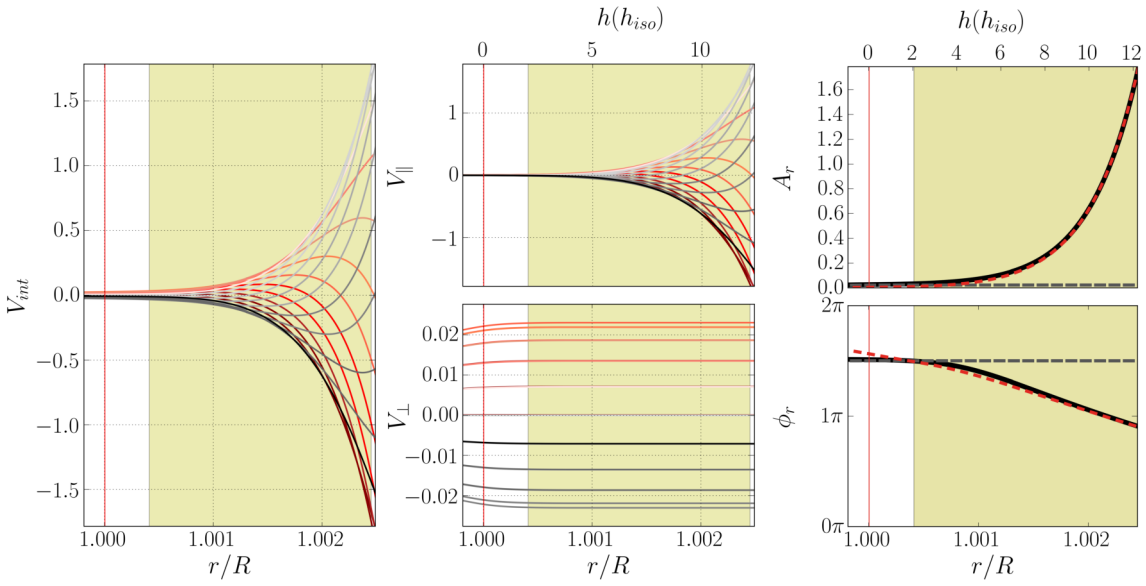

(b) equator-on view

Figure 3.18: The same as Fig. 3.4 but for a mode of frequency 2.2 mHz and degree $l = 2$, a magnetic field of 2 kG: figure (a) with a pole-on view and figure (b) with an equator-on view.

Chapter 4

Other interesting results

4.1 Parameter space

In this chapter we will review some interesting cases found when exploring the parameter space underlying the theoretical radial velocity calculations based on the model presented in Chapter 2. They were chosen either because they are out of line with the general behavior seen in the previous chapter, or because they give us an idea of the diversity of features that we can find in roAp stars.

To explore the possible solutions and study the general behavior of the radial velocities in the case of the full visible disk, we considered the following parameters' ranges:

1. Frequencies from 1.2 mHz to 3.3 mHz;
2. Polar magnetic field intensity from 1.0 kG to 4.0 kG, with intervals of 1 kG;
3. Observer views: Pole-on view, view from 30° and 60° from the pole, and equator-on view.

We also explored three different types of spots in the atmosphere: a polar spot, an equatorial belt, and a spot in the middle of the hemisphere. In the cases of the spots we considered the same range of parameters as before for the magnetic field and the observer view, but we modified the frequency range adopting, instead, an interval from 1.7 mHz to 3.1 mHz. The cases that we selected with full integration of the visible disk are listed in table 4.1.

To simulate a spot of elements in the atmosphere of a roAp star we have chosen three different areas of integration. For the equatorial belt, the region in the star's coordinate system was chosen to be $53° < \theta < 127°$. For the belt in the middle of the hemisphere, we chose $30° < \theta < 60°$. Finally for the spot located in the pole, we chose $\theta < 41°$. In

Table 4.1: Properties and parameters for the cases with full disk integration to explore in this chapter. The columns are: frequency, f; polar magnetic field, B_p; observer's view; mode degree, l; and the critical angle, α_{cr}.

	f [mHz]	B_p [kG]	Obs. position	l	α_{cr}
Case 1	2.9	3.0	pole 60° from pole 30° from pole equator	0	0°
Case 2	2.5	1.0	equator	2	21°
Case 3	2.0	1.0	pole	2	40°
Case 4	2.0	1.0	30° from pole pole 60° from pole	3	40°
Case 5	2.9	4.0	60° from pole	4	0°

Table 4.2: Properties and parameters for the cases of partial integration to explore in this chapter. The columns are: frequency, f; polar magnetic field, B_p; observer's view; mode degree; Spot type; and the critical angle, α_{cr}.

	f [mHz]	B_p [kG]	Obs. position	l	Spot type	α_{cr}
Case 1	2.7	2.0	pole	1	Equator	0°
Case 2	2.7	4.0	equator	2	Equator	0°
Case 3	2.3	1.0	60° from pole	0	Equator	30°
Case 4	2.3	3.0	pole	1	Middle	30°
Case 5	2.4	2.0	pole	1	Polar	21°

all these cases φ was taken as varying between 0 and 2π, but only regions of θ and φ occupying the visible disk were considered in the actual integration. The cases considered are listed in table 4.2.

4.2 Cases with full disk integration

4.2.1 Dependence on observer's position

For all the frequencies considered in the previous chapter, we verified that the radial velocity amplitude and phase variations changed when the star was observed from different lines of sight, in particular from pole-on and equator-on. We present here a case in which the phase variation with height maintains the same functional form when changing the observer's direction. This case is for a mode with a frequency of 2.9 mHz and degree

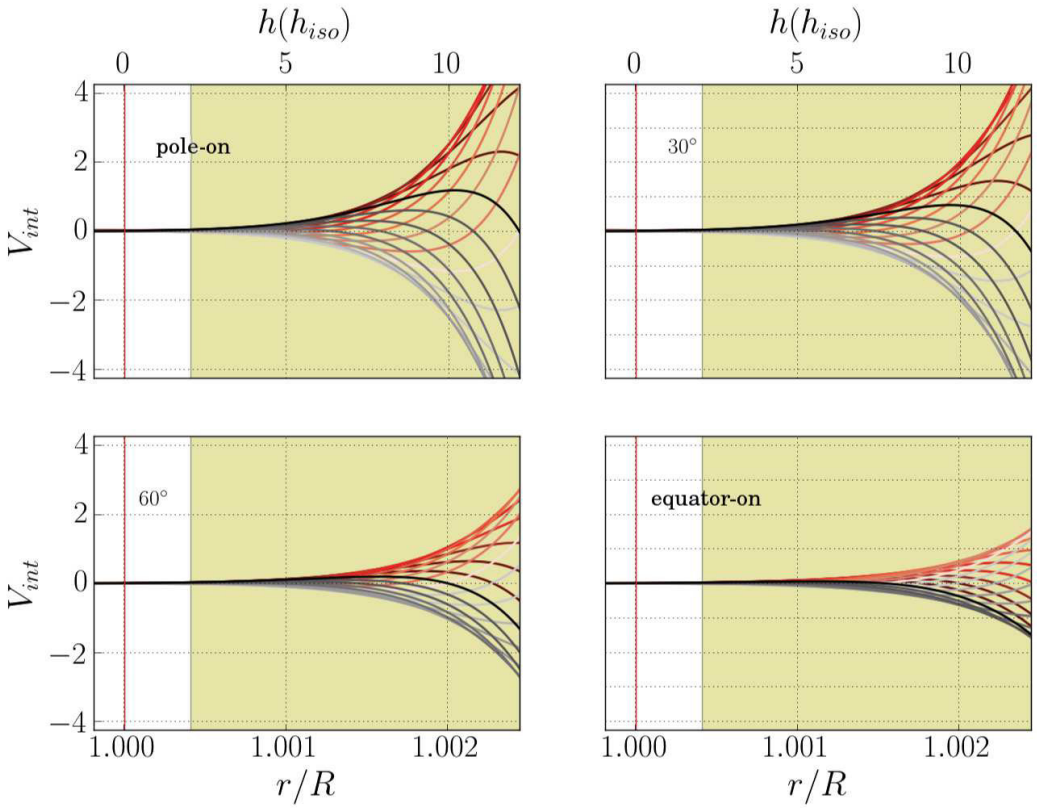

Figure 4.1: Dimensionless and normalized radial velocity. This case is for integration over the visible stellar disk, a magnetic field of 3 kG, a mode of frequency 2.9 mHz and degree $l = 0$, for 4 different observers. Top-left panel, a pole-on view, top-right panel, 30° from the pole, bottom-left panel, 60° from the pole and bottom-right panel, an equator-on view. In each panel we shown the radial velocity as a function of the radius, at different times within the oscillatory period represented by curves of different colors. Labels, red line and yellow shadow have the same meaning as in previous figures.

$l = 0$, and a magnetic field of 3 kG. The radial velocity is illustrated in Fig. 4.1 for different observer views. Comparing the results obtained from the four different views, we can see that the amplitude decreases, as expected from the previous chapter, as the observer moves, from a position at the pole (top-left panel), towards a position in the equator (bottom-right panel), passing by the two intermediate positions. This effect is due to the direction of acoustic and magnetic waves in the atmosphere and the dependence of their amplitude on atmospheric height (we note that the frequency chosen here is above the acoustic cutoff, so in this case there is no impact from the changing from acoustic standing, to acoustic running waves).

In Fig. 4.2(a) we show the amplitude (left top panel) and phase variation (left bottom panel) for the frequency under consideration. The red line is the pole-on view, the dark-red line is the view from 30° from the pole, the brown line is the view from 60° from the pole, and the black line is the equator-on view. The amplitude shows indeed a significant variation when the observer's location is changed. As for the phase, it also varies with the observers's location, but the slope of the curve is similar in all cases except for the equator-on view.

To investigate the impact of the mode frequency in the case above, in Fig. 4.2 (b) and (c) we include also the results for smaller frequencies. The middle panels (b) show the amplitude and phase variation for a mode with a frequency of 2.4 mHz, and the right panels (c) show the amplitude and phase variation for a mode with a frequency of 2.1 mHz. When we compare the diferent modes, we can see that the variation in amplitude resulting from a change in the observer's location is larger for higher frequencies. Regarding the phase variation, we can see that the slope of the curve becomes larger as the frequency increases, as expected, from the increase in the area covered by acoustic running waves. In addition, we note that for the frequencies of 2.4 mHz and 2.1 mHz the difference between the pole-on and equator-on view phase curves is more significant than for the frequency of 2.9 mHz. This is due to the fact that in the latter case the acoustic waves are always running waves, which results in a smaller dependence of the result on the observer's position.

4.2.2 Phase almost constant at high frequency

Here we illustrate a case of an almost constant phase found for a mode with a frequency of 2.5 mHz and a degree $l = 2$, with a magnetic field of 4 kG, and an observer pole-on. We have chosen this case because, despite its frequency being close to the acoustic cut-off, it has an almost constant phase. The radial velocity is shown in the left panel of Fig.

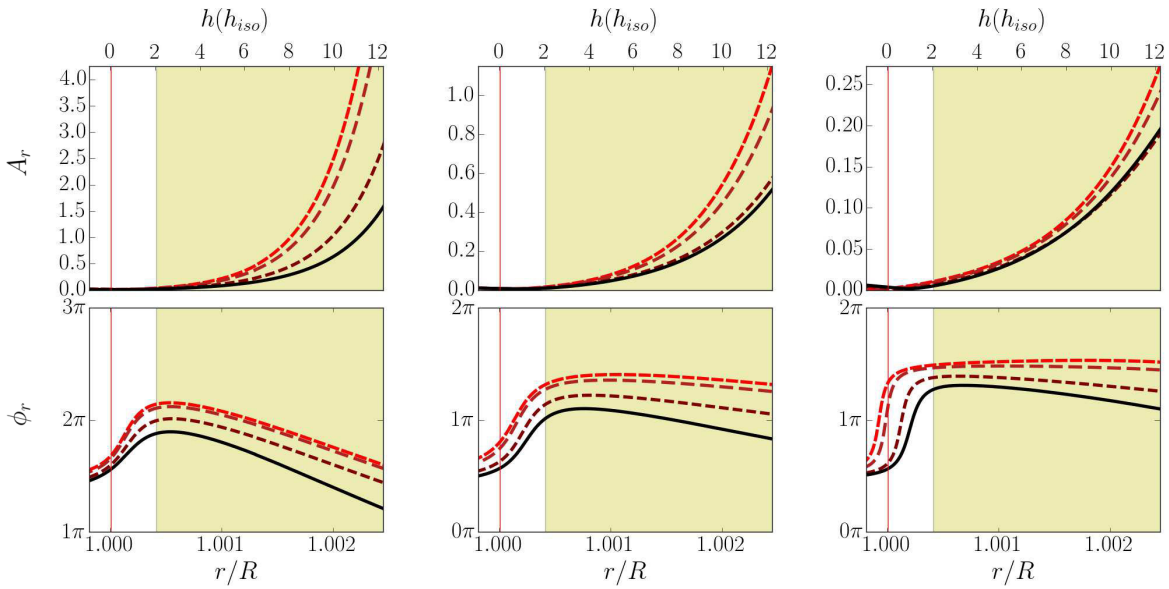

(a) $f = 2.9$ mHz (b) $f = 2.4$ mHz (c) $f = 2.1$ mHz

Figure 4.2: The amplitude (top) and the phase (bottom) of the radial velocity extracted by fitting to the function given by eq. (3.12), for modes of degree $l = 0$ and frequencies as indicated by the lower label. The polar magnetic field has a magnitude of 3 kG, and 4 different observers are considered. The radial velocity amplitude and phase for a pole-on observer are shown by a dashed-red line, for an observer 30° from the pole are shown by a dashed-dark-red line, for an observer 60° from the pole are shown by a dashed-brown line, and for an equator-on observer are shown in black. Labels, red line and yellow shadow have the same meaning as in previous figures.

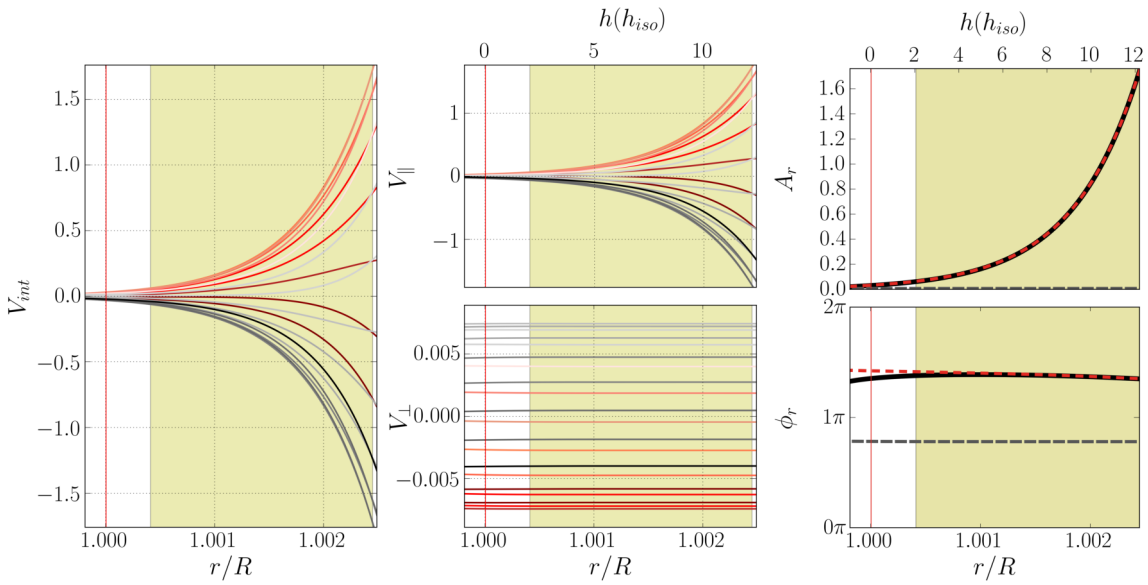

Figure 4.3: The same as Fig. 3.4 but for a mode with a frequency of 2.5 mHz and degree $l = 2$, a magnetic field of 1 kG, and an equator-on observer.

4.3 and the contribution to it from the parallel and perpendicular components are in the middle panel, top and bottom, respectively. Comparing the contribution of the parallel component (or acoustic wave's contribution) with the radial velocity we see that they are very similar, which means that the integral is dominated by the acoustic waves, as we saw for the previous cases with $l = 2$ and the pole-on view.

In the right panels of Fig. 4.3 we can see the amplitude and phase variation of the radial velocity and the parallel and perpendicular contributions to it. The total amplitude (black line) and the parallel amplitude (red line) overlap, which confirms the dominance of the acoustic waves in the star's atmosphere. The relevance of this case, however, is the phase variation. With the quadrupole mode the phase variation of the acoustic waves is almost canceled out when we integrate over the visible disk. Consequently, the phase ends up showing a similar behavior to that seen for a frequency far below the acoustic cut-off.

4.2.3 False node at $l = 2$

Next we illustrate the case of a mode with a frequency of 2.0 mHz and a degree $l = 2$, with a magnetic field of 1 kG. When the observer is equator-on a false node is formed in the first part of the isothermal atmosphere. When we look at the radial velocity, in Fig. 4.4 left panel, we see the amplitude decreasing at a relative radius of 1.0007. Looking at the radial velocity curves for each time, given by the different color lines, we see the

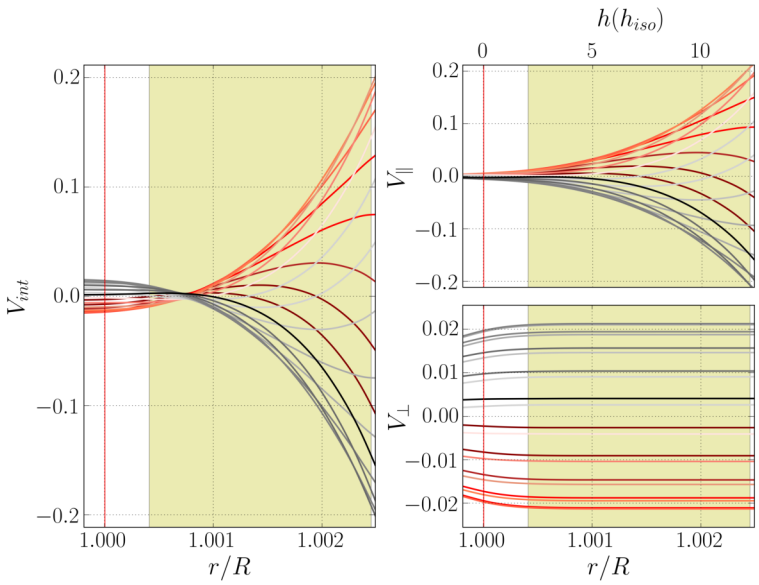

Figure 4.4: Dimensionless and normalized radial velocity. This case is for integration over the visible disk, a magnetic field of 1 kG, a mode of frequency 2.0 mHz and degree $l = 2$, and an observer equator-on. Shown in the left panel is the radial velocity as a function of the radius. The upper right panel shows the contribution to the radial velocity of the velocity component parallel to the magnetic field. The bottom right panel shows the contribution to the radial velocity of the velocity component perpendicular to the magnetic field.

inversion in the amplitude sign at that point, as expected for perturbations that are in counter-phase. As we saw in the previous chapter, for modes with a degree $l = 2$ and an equator-on observer we have a dominance of the magnetic waves, that, depending on the frequency, can reach different heights in the atmosphere. Looking at the parallel and perpendicular contributions (right panels), we can see that no node is present either in the acoustic or magnetic waves' contributions, but the color lines show that the two contributions have opposite sign.

Now, looking at Fig. 4.5 top-left panel, we see that the parallel (red line) and perpendicular (grey line) amplitudes cross each other, while the total amplitude (black line) decreases to almost zero. In the total phase variation (bottom-left panel), we identity the sudden variation of π that creates the false node, as we have discussed previously for the frequency of 2.7 mHz. But in this case the node is just visible for the pole-on observer, starting to dissipate when we change the observer's location. With the observer at 30° from the pole the amplitude decrees at the same radius, but it does not go down to zero. The phase variation seen in Fig. 4.5 is not as sudden as in the case shown in chapter 3, but it is fast enough to be interpreted as a phase jump in the observations. Moreover, it

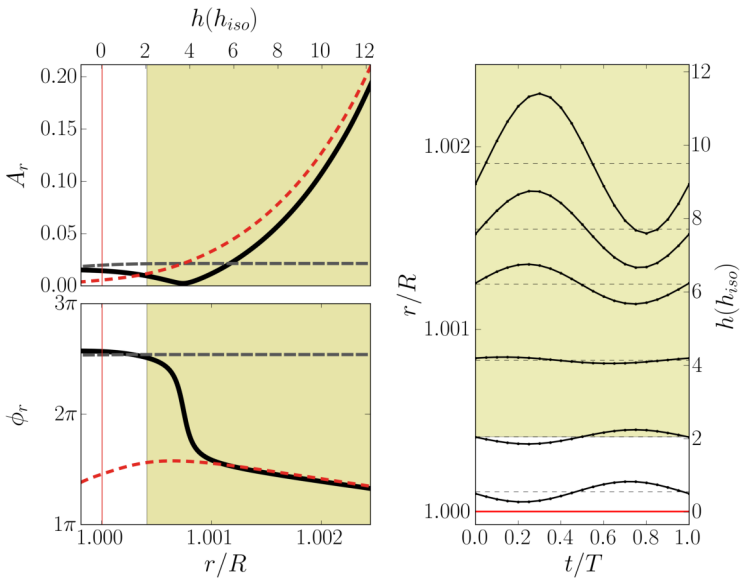

Figure 4.5: The left panels show the amplitude (top) and the phase (bottom) of the radial velocity extracted from fitting it to the function given by eq. (3.12) for a mode of frequency 2.0 mHz and degree $l = 2$, a magnetic field of 1 kG, observed from an equator-on view. The radial velocity amplitude and phase are in black, the amplitude and phase derived from $V_{\parallel}$ in red, and the amplitude and phase derived from $V_{\perp}$ in grey. The right panel shows the amplitude of the radial velocity at different heights in the atmosphere, as a function of the fraction of time within an oscillation period T.

takes place at higher atmospheric layers than the phase jump seen in the case illustrated in chapter. 3. The right panel of Fig. 4.5 gives us also an idea of the behavior of the phase. The figure shows the amplitude variation at different heights in the atmosphere. We clearly see that the curves in the upper and lower layers are in anti-phase. However, we also see that where the transition occurs the radial velocity does not reach zero amplitude.

4.2.4 False node at $l = 3$

We now present the case of a false node for a frequency of 2.0 mHz and a magnetic field of 1 kG, the same as in the previous case, but for a mode with a degree $l = 3$. Here the false node is formed with the observer at 30° from the pole, and can be seen only from this line of sight. The radial velocity for this case is presented in Fig. 4.6 left panel, and we see the false node at the beginning of the isothermal atmosphere. Again, when we look at the contributions of the parallel and perpendicular waves' components, right panels, we do not see the formation of nodes, which means that neither the acoustic nor the magnetic waves have oscillating nodes.

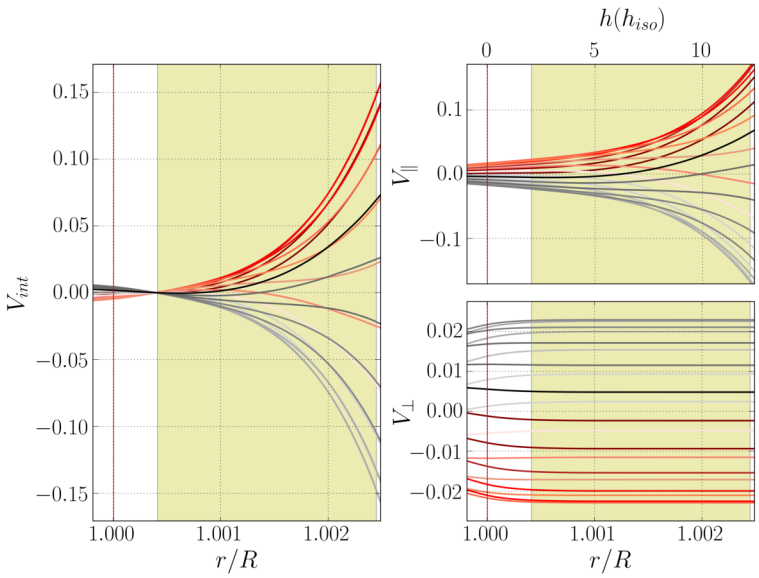

Figure 4.6: The same as Fig. 4.4 but for a mode of frequency 2.0 mHz and degree $l = 3$, a magnetic field of 1 kG, and an observer located 30° from the pole.

Inspecting the amplitude and phase variation in Fig. 4.7, we can see that the parallel (red line) and perpendicular (grey line) amplitudes cross each other, while the total amplitude (black line) decreases to zero, and that the total phase jumps by π, creating the false node. In the right panel, showing the amplitude variation with time at different heights in the atmosphere, we also see that there is a change in the phase between the upper and lower atmospheric layers, but this time at the radius where the transition occurs the radial velocity amplitude is zero.

This case is also a good example of how significant the change in the phase can be when we change the observer's position. To illustrate that, we have included in Fig. 4.8, the amplitude and phase variation for the cases of observers pole-on and at 60° from the pole (left and right panels, respectively). We see the total phase changes from a positive variation when the observer is pole-on, to form a false node with a π jump with the observer located 30° from the pole, and then the phase changes to a negative variation with the observer located 60° from the pole. By comparing the parallel and the perpendicular phase for each observer we see that they are not so different. However, modifying the observer's view shifts the place where the dominance of the waves occurs, resulting in very different total phases.

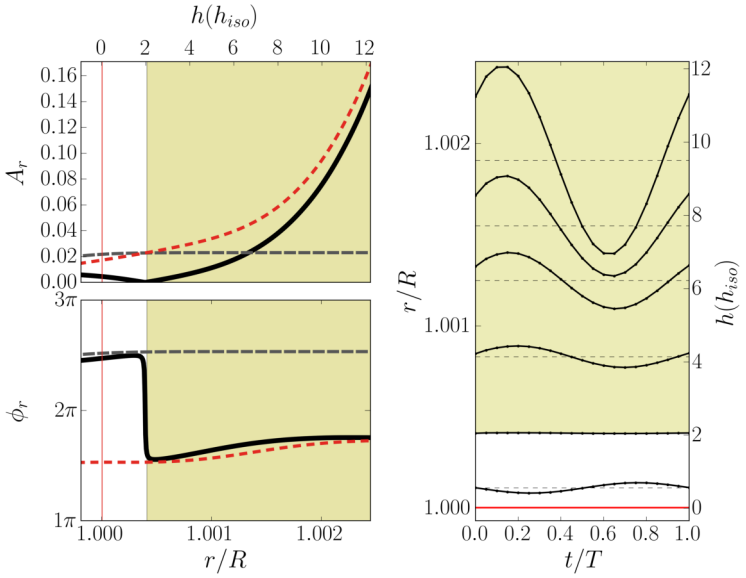

Figure 4.7: The same as Fig. 4.5 but for a mode of frequency 2.0 mHz and degree $l = 3$, a magnetic field of 1 kG, and an observer located 30° from the pole.

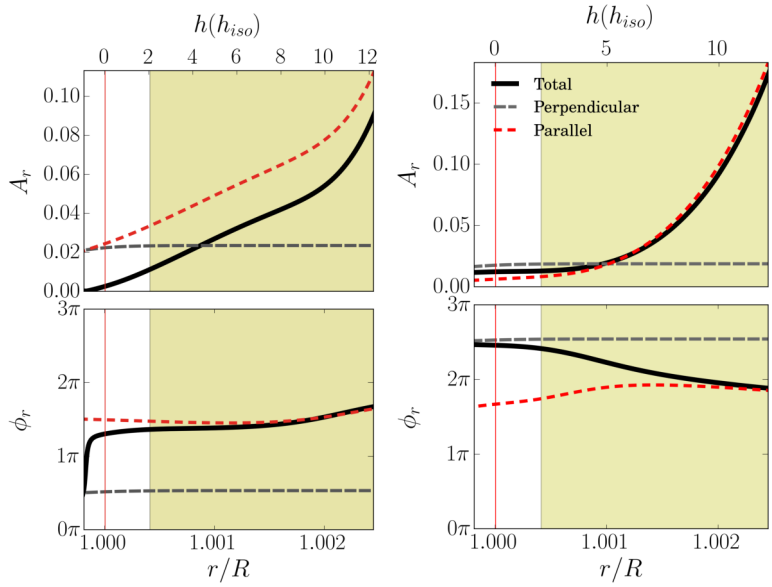

(a) pole-on (b) 60° from the pole

Figure 4.8: The same as right panel of Fig. 4.5 but for a mode of frequency 2.0 mHz and degree $l = 3$, a magnetic field of 1 kG for two different observers. Figure (a) with a pole-on view and the figure (b) with a view 60° from the pole.

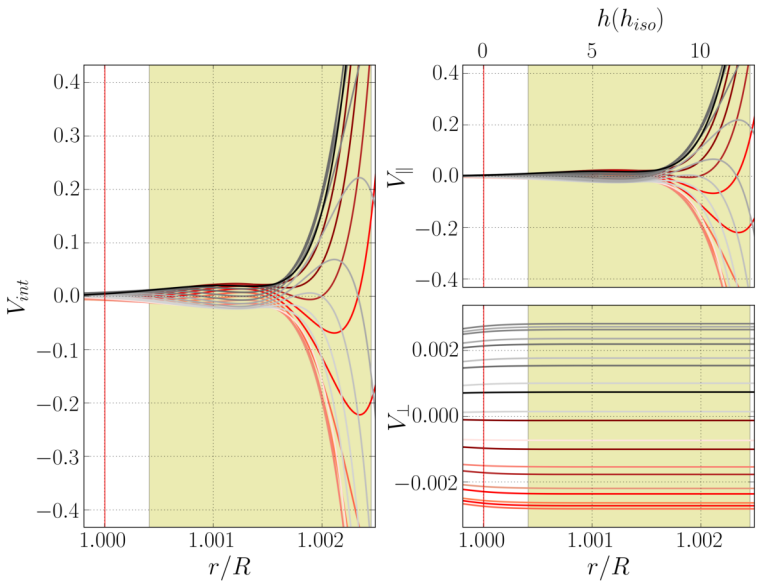

Figure 4.9: The same as Fig. 4.4 but for a mode of frequency 2.9 mHz and degree $l = 4$, a magnetic field of 4 kG, and an observer that is at 60° from the pole.

4.2.5 Unusual phase

Next we discuss the case of a mode with a frequency of 2.9 mHz and a degree of $l = 4$. The polar magnetic field B_p is 4 kG, and the observer is located at 60° from the pole. This case is selected because it shows a different phase behavior, compared to what has been presented so far. The radial velocity for this case is illustrated in Fig. 4.9, left panel, and we can see that the shape of the curve is far from the exponential form that we have found in the previous chapter, and it is also different from that found for the false nodes that we have discussed in this chapter. By looking at the contribution from the acoustic and magnetic waves, Fig. 4.9, right panels, we can see that the shape of the acoustic contribution is the same as that of the radial velocity, and that the magnetic contribution is two orders of magnitude smaller, having almost no influence in the radial velocity.

In Fig. 4.10 left panels, we can see the amplitude (top panel) and the phase (bottom panel) variation for this case. Clearly, the non-exponential shape of the total amplitude (black line) does not originate in the change of dominance between acoustic and magnetic waves. Instead, the behavior is completely dominated by acoustic waves, that are interacting destructively[1] in the interior part of the atmosphere, producing this unusual pattern for the total and the parallel amplitude. The same phenomena is noticeable in the phase behavior, as seen from the local inversion of its evolution with height at the

[1]In the sense that are partially canceling out when performing the integral defining the radial velocity

depth where the amplitude is smallest, resulting in a phase that first increases and then decreases with height in the atmosphere.

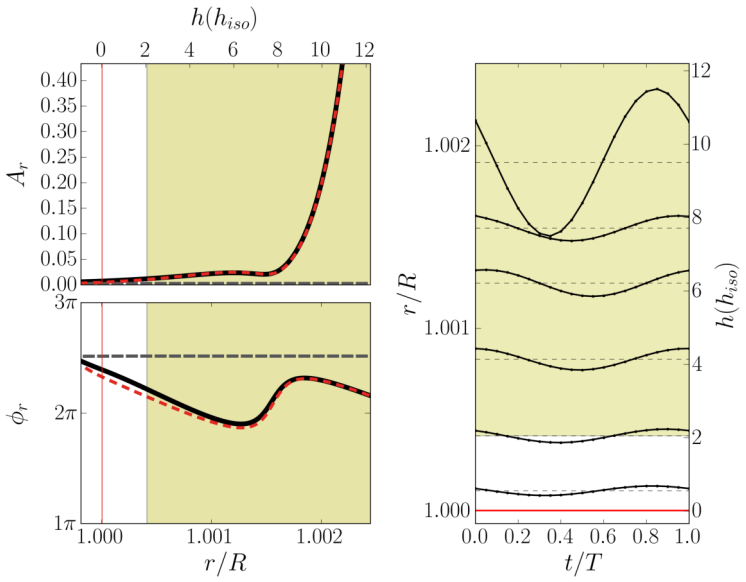

Figure 4.10: The same as Fig. 4.5 but for a mode of frequency 2.9 mHz and degree $l = 4$, a magnetic field of 4 kG, and an equator-on observer.

The strange variation in the phase is also clear in the right panel of Fig. 4.10, that shows the amplitude as a function of the time of the radial velocity at different heights. If we follow the zeros of the amplitude across the different heights we see that they first move to right and then move to the left as we look down through the atmosphere.

4.3 Partial Integration

4.3.1 Equatorial spot

For the equatorial spots we select three cases showing an apparent node in the middle of the isothermal atmosphere, as first discussed by Sousa & Cunha (2011) for a toy model of a full isothermal atmosphere. For the first case, we consider a mode with a frequency of 2.7 mHz, that is above the acoustic cut-off, and degree $l = 0$, and a magnetic field of polar magnitude $B_p = 2$ kG. Moreover, the observer is pole-on, and we assume the elements are concentrated around the equator, in the region defined by $53° < \theta < 127°$.

The radial velocity for this case is shown in Fig. 4.11, left panel. In the middle of the isothermal atmosphere we can see a sudden change in the radial velocity which looks somewhat similar to what one would expect in the presence of a node.

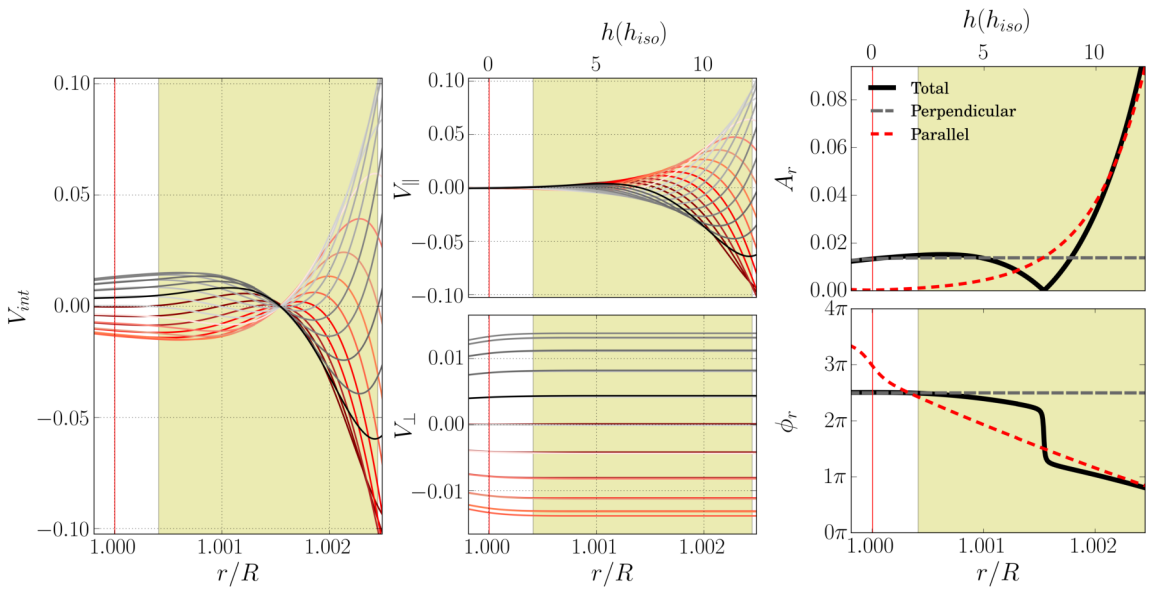

Figure 4.11: The same as Fig. 3.4 but for a mode with a frequency of 2.7 mHz and degree $l = 0$, a magnetic field of 2 kG, and an observer pole-on. The integration is in the region defined by $53° < \theta < 127°$.

From the inspection of the middle panels of the same figure, we notice that in this case the acoustic and magnetic waves' contributions are overall of the same order of magnitude. Thus, we can recognize in the radial velocity shown in the left panel, the exponential behavior of the acoustic waves in the upper atmosphere, but also, the constant behavior of the magnetic waves in the inner atmosphere. As for the frequency 2.7 mHz discussed in the previous chapter, we can see that the acoustic and magnetic waves' contributions are out of phase, as seen by the fact that for a given time (given color line in the middle panels), the acoustic (top panel) and magnetic (bottom panel) contributions have opposite sign. This leads again to a cancellation in the integral defining the radial velocity and is the cause of the apparent node.

For the stellar model adopted in this work, we find this type of apparent nodes in the higher atmospheric layers when considering elements distributed around the equator. They are seen from any observer's position, and, more commonly, for even-degree modes.

The amplitude and phase variations are shown in Fig. 4.11, right panels. We see the total amplitude (black line, top panel) changing from behaving similarly to the amplitude of the acoustic wave's contribution (red line, same panel) in the upper atmosphere to behaving like the amplitude of the magnetic wave's contribution (gray line, same panel) in the inner atmosphere. Moreover, because the magnetic and acoustic waves' contributions are similar in magnitude but with opposite sign, at some point in the isothermal atmosphere the total amplitude decreases, going through a local minimum. At the same

location we see the total phase varying by π (black line, bottom panel). These variations in amplitude and phase, in the inner atmospheric layers, would, in an observational context, be interpreted as a presence of a node. However, similar to the apparent nodes formed in lower atmospheric layers, this behavior is not caused by a node in a standing wave. It is simply a visual cancellation effect between the acoustic and magnetic contributions to the radial velocity.

From our analysis, we find that the false nodes induced by equatorial belts are a very common feature, meaning that, several modes with different parameters (magnetic field, mode frequency and mode degree) form false nodes, and they can be seen from any line of sight. For a specific set of parameters, however, in some cases the false nodes can be seen from two different observer locations, but in the majority of the cases, they are found only for a single observer.

We have selected, for illustration, two additional cases that correspond to false nodes viewed from two other directions of the observer. The radial velocity for a case with a false node with an observer equator-on is shown in Fig. 4.12, left panel. This is a case with a frequency of 2.7 mHz, a degree of $l = 2$ and a magnetic field of 4 kG. As in the previous case, we can recognize in the radial velocity shown in the left panel, the exponential behavior of the acoustic waves in the upper atmosphere, but also, the constant behavior of the magnetic waves in the inner atmosphere. And like in the others nodes that we discussed, we can see from the middle panels that the acoustic and magnetic waves' contributions are out of phase. This leads again to a cancellation in the integral defining the radial velocity and is the cause of the apparent node.

Next, we consider a equatorial belt with an observer at 60° from the pole. In Fig. 4.13 we show the radial velocity (left panel) for a mode with a frequency of 2.3 mHz, a degree of $l = 0$ and a magnetic field of 1 kG. A false node is formed at a relative radius 1.0012. As before, this node cannot be seen in the contributions from the acoustic or magnetic waves' components, top and bottom middle panels, respectively.

In Fig. 4.14 we can see the amplitude variation at different heights for the three cases of the equatorial belts discussed here. The phase jump in each of the three cases occurs at a different height, but always in the upper half of the isothermal atmosphere. This is because the integration is performed only in the stellar equatorial region (where the spot is located) and there the radial velocity has a more significant contribution from the magnetic waves than in the stellar polar regions.

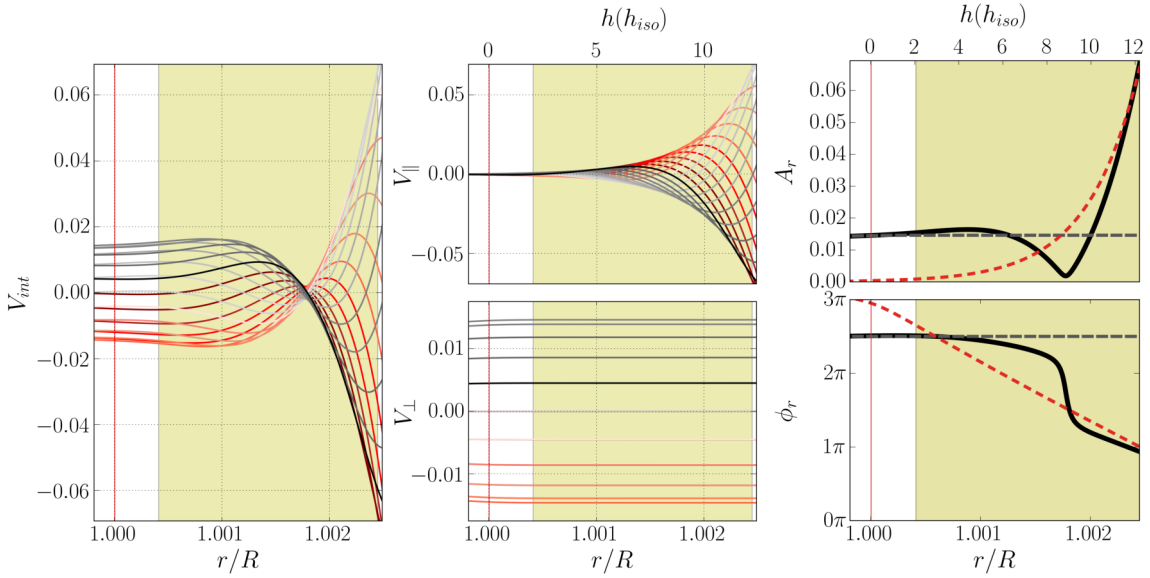

Figure 4.12: The same as Fig. 3.4 but for a mode of frequency 2.7 mHz and degree $l = 2$, a magnetic field of 4 kG, and an observer equator-on. The integration, for this case is in the region defined by $53° < \theta < 127°$.

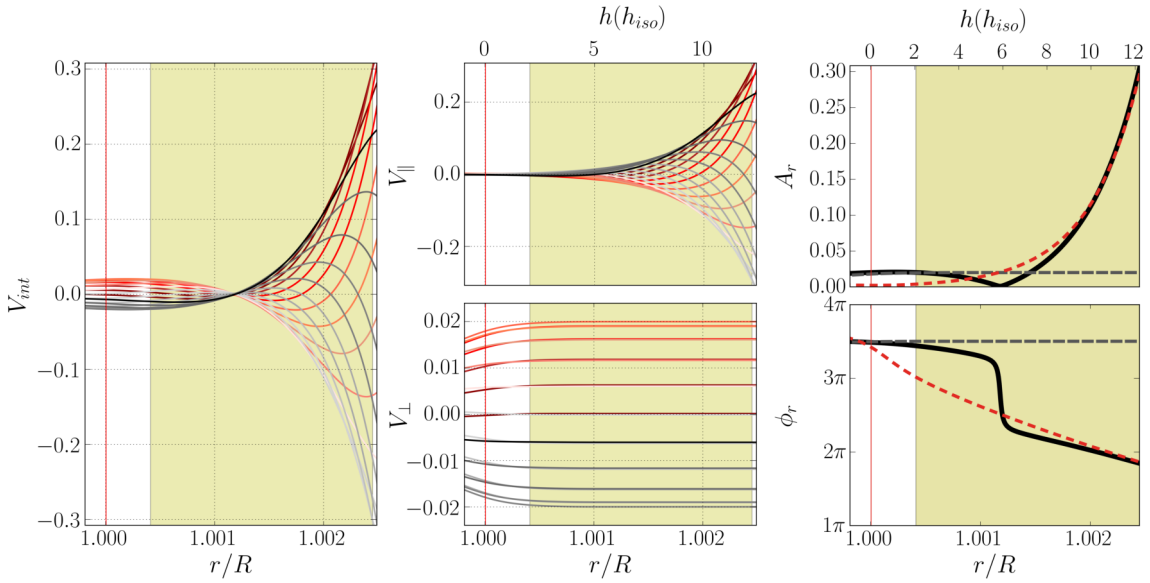

Figure 4.13: The same as Fig. 3.4 but for a mode of frequency 2.3 mHz and degree $l = 0$, a magnetic field of 1 kG, and an observer of 60° from the pole. The integration, for this case is in the region defined by $53° < \theta < 127°$.

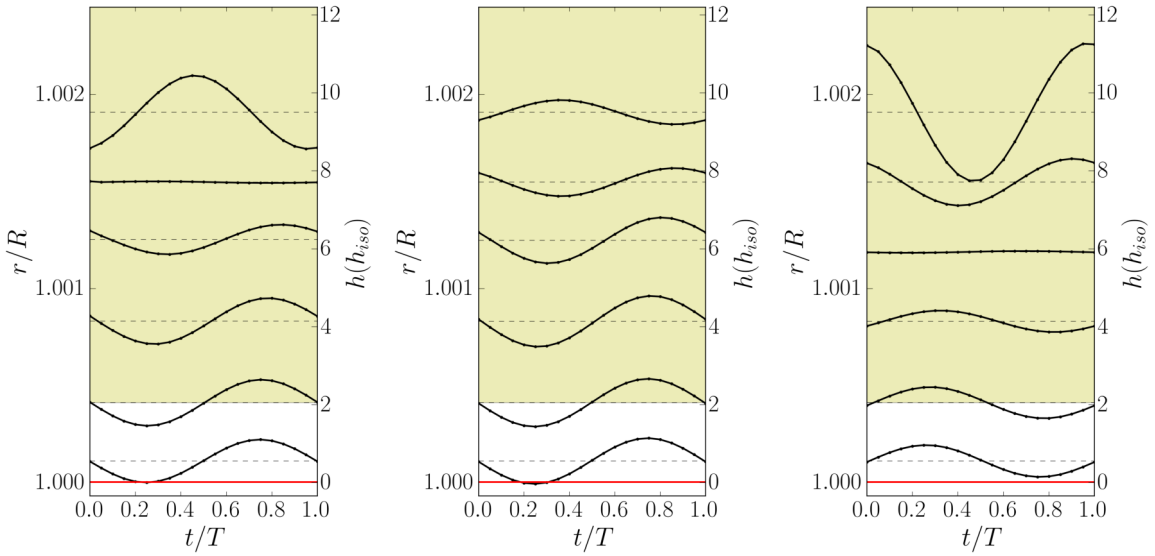

(a) 2.7 mHz - 2 kG (b) 2.7 mHz - 4 kG (c) 2.3 mHz - 1 kG

Figure 4.14: The figures show the amplitude of the radial velocity at different heights in the atmosphere, as a function of the fraction of time within an oscillation period T. The horizontal red line mark the bottom of the photosphere. (a) Mode of frequency 2.7 mHz, a degree of $l = 0$, a magnetic field of 2 kG, and an observer pole-on. (b) Mode of frequency 2.7 mHz, a degree of $l = 2$, a magnetic field of 4 kG, and an observer equator-on. (c) Mode of frequency 2.3 mHz, a degree of $l = 0$, a magnetic field of 1 kG, and an observer at 60° from the pole. For the three cases the integration is in the region defined by $53° < \theta < 127°$.

4.3.2 Spot in the middle of the hemisphere

To illustrate the results for a spot in the middle of the hemisphere, we select a case that shows a false node. The case is for a mode with a frequency of 2.3 mHz, a degree $l = 1$, a magnetic field of 3 kG, and an observer pole-on. Despite the fact that in the parameter space that we explore, the cases of a false node are not as common in a spot in the middle of the hemisphere as in an equatorial spot, we wanted to highlight this case that shows that it is also possible for a false node to appear for this type of spots. The radial

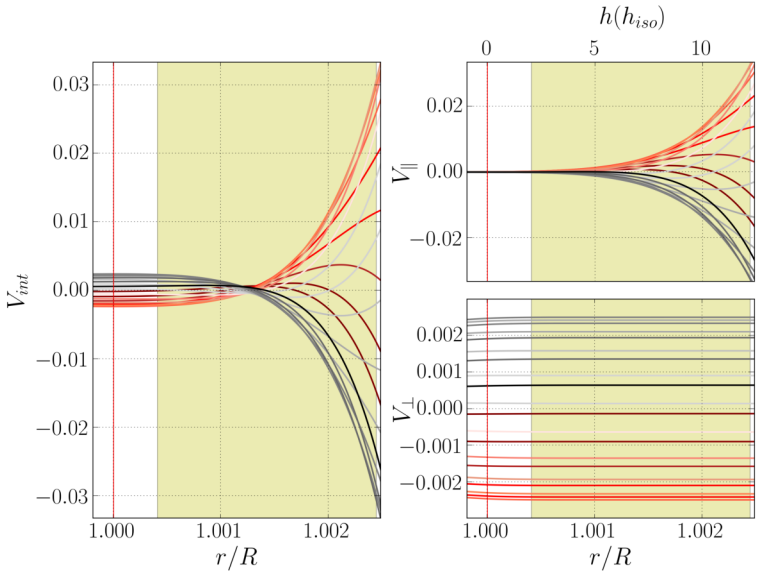

Figure 4.15: The same as Fig. 4.4 but for a mode of frequency 2.3 mHz and degree $l = 1$, a magnetic field of 3 kG, and an observer pole-on. The integration, for this case is in the region defined by $30° < \theta < 60°$.

velocity for this case is shown in Fig. 4.15, left panel, and it presents evidence for a false node at the relative radius of 1.0012. Concerning the contributions of the acoustic and magnetic waves they have the same order of magnitude throughout a large fraction of the isothermal atmosphere and opposite signs.

In Fig. 4.16 left panel, we see the amplitudes of the parallel and perpendicular components crossing each other, and the total phase going almost to zero at the same radius. In the same way, we see in the variation of the total phase the jump of almost π. Although this case does not present a complete node, in the observations it could be interpreted as one, as seen from Fig. 4.16, right panel.

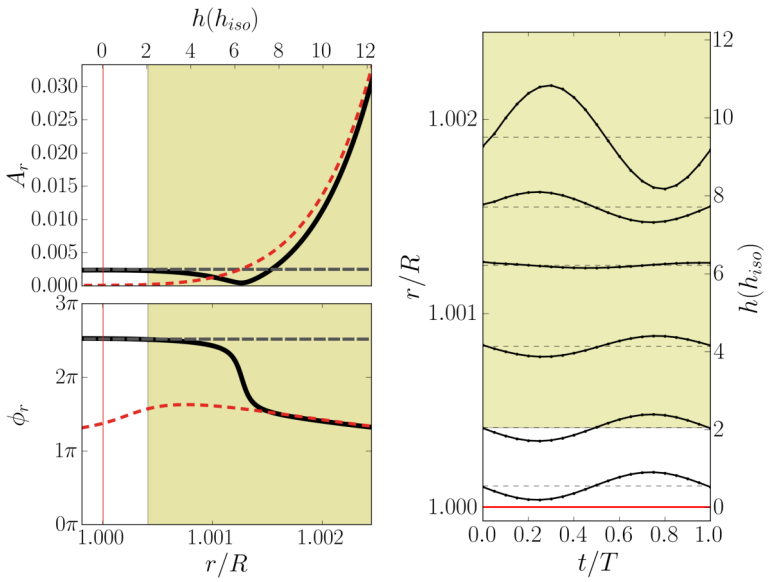

Figure 4.16: The same as Fig. 4.5 but for a mode of frequency 2.3 mHz and degree $l = 1$, a magnetic field of 3 kG, and an observer pole-on. The integration for this case is in the region defined by $30° < \theta < 60°$.

4.3.3 Polar spot

Finally, the last case that we present is that of a polar spot, for which we have not found the formation of false nodes in the atmosphere. Here we present the most common behavior we have found for this kind of spots. As we can see in Fig. 4.17, the radial velocity and the contribution to it from the parallel component of the wave are nearly the same, since the contribution of the perpendicular component is two orders of magnitude smaller than that of the parallel component. The dominance of the acoustic waves is even more clear when we look at the amplitude and phase variation on the right panels, where the total amplitude (black line) and the parallel amplitude (red line) overlap in the atmosphere of the star. The same happens for the total phase, with the difference that here in the interior of the atmosphere we start to see a change in the dominance of the contributions, from the parallel to the perpendicular phase (grey line).

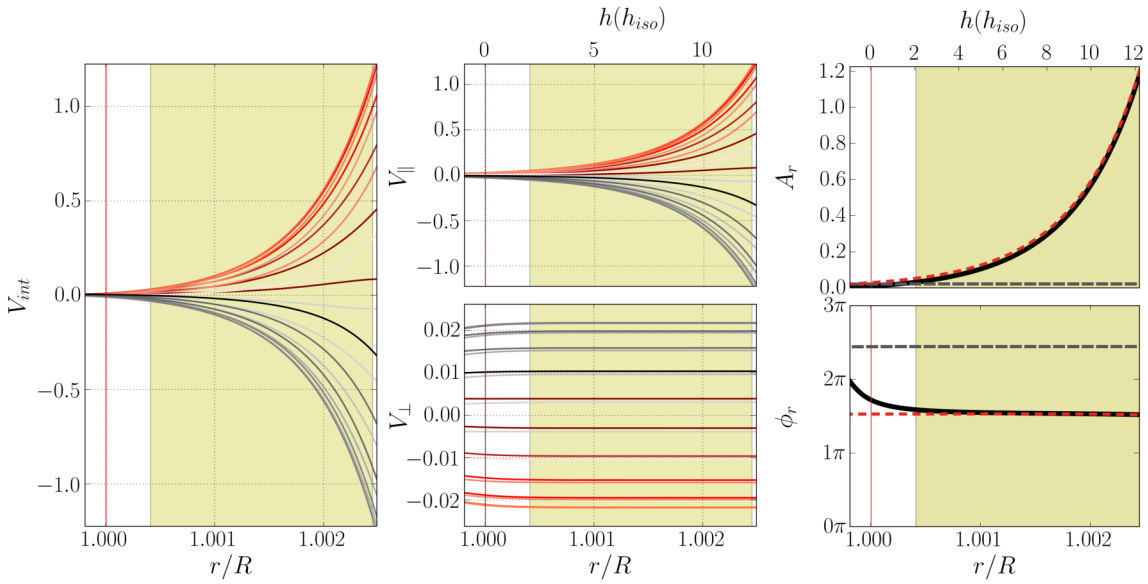

Figure 4.17: The same as Fig. 3.4 but for a mode of frequency 2.4 mHz and degree $l = 1$, a magnetic field of 2 kG, and an observer pole-on. The integration, for this case is in the region defined by $\theta < 41°$.

Chapter 5

Mode visibility in roAp stars

5.1 Cancellation effect

Up to now, we have concentrated on the modelling of the radial velocities associated with pulsations in roAp stars. Observationally, these can be studied through the analysis of high-resolution spectroscopic time series obtained with large telescopes on Earth. However, pulsations in roAp stars can also be studied from the analysis of photometric time series, as described in many studies published in the literature (Martinez et al., 1991; Martinez & Kurtz, 1994). With the advent of space data, such as that collected by the Canadian MOST and the NASA Kepler satellites for a few roAp stars (Gruberbauer et al., 2008; Holdsworth et al., 2016, 2014b) and, in particular, with the recently launch of the TESS mission, from NASA, photometric studies of roAp stars become increasingly important. For that reason, it is important also to predict the luminosity perturbations associated to pulsations in magnetic models of roAp stars.

The variation of the luminosity over time, as seen by a given observer, is computed by integrating the flux over the visible disk. Consequently, just as in the case of the radial velocity, for high degree modes there are cancellation effects (Aerts et al., 2010). For a normal pulsator, the consequence of such cancellation effects is that for modes of degree larger than 2, the luminosity variation becomes virtually undetectable, and for modes of degree larger than 3 the same happens for the radial velocities. In roAp stars, however, the distortion of the pulsations by the magnetic field may lead to a smaller cancellation in the higher degree modes. In order to investigate on the possibility of observing modes of degree larger than $l = 3$ in roAp stars, we compute the "luminosity perturbation"[1] and the radial velocity for modes of degrees from 0 to 7.

[1]Here, "luminosity perturbation" refers to the integrated flux variation seen by the observer.

This chapter is organized as follows: in Sec. 5.2 we present the expression used for the computation of the luminosity perturbation. In Sec. 5.3 we use a non-magnetic model to discuss the impact of the magnetic field on the luminosity perturbation and on the radial velocity and, finally, in Sec. 5.4, we compute the visibility of low degree modes in photometry and radial velocity, comparing it with the non-magnetic case.

5.2 Luminosity perturbation

To compute the luminosity perturbation, $\delta L/L$, we first recall that there are three different contributions to the it (Dziembowski, 1977). The first is associated to the variation of the flux, $\delta F/F$, the second is associated to the change in the integration area, and the third is associated to the change in the normal direction of a given surface element. However, because in our model the oscillations have small amplitude, we consider the changes in brightness due to the change of area in the surface element and its normal direction to be negligible compared to those resulting from the variation in the flux. Thus, the luminosity perturbation can be calculated using the integral,

$$\frac{\delta L}{L}(t) = \int_{\varphi'_i}^{\varphi'_f} \int_{\theta'_i}^{\theta'_f} \frac{\delta F}{F} \times \frac{1}{C_n}(1 - a(1 - \cos\theta')) \cos\theta' R^2 \sin\theta' d\theta' d\varphi'. \tag{5.1}$$

Through the Stefan-Boltzmann equation we can establish the relation between the flux and the temperature at the surface of the star. Assuming that each surface element of area emits as a black body with a temperature T we have, $F = \sigma T^4$, where σ is the Stefan-Boltzmann constant. When we apply a small perturbation to this equation we obtain,

$$\frac{\delta F}{F} = 4\frac{\delta T}{T}, \tag{5.2}$$

where δ refers to a Lagrangian perturbation.

Now, to compute the temperature variation we recall that in our model the oscillations are treated in the adiabatic approximation. Under the adiabatic approximation, this perturbation is proportional to the Lagrangian pressure perturbation and, thus, can be expressed in dimensionless form by

$$\frac{\delta T}{T} \propto \frac{\delta p}{p}. \tag{5.3}$$

Moreover, the Eulerian pressure perturbation, p', can be computed using the displace-

ment eigenfunction through eq. (2.6). Its final expression can be written as,

$$p' = -\xi_z \frac{\partial}{\partial r} p - \gamma p \left(\frac{1}{r^2} \frac{\partial}{\partial r} \left(r^2 \xi_z e^{i\omega t} Y_l^0 \right) + \frac{1}{r \sin\theta} \frac{\partial}{\partial \theta} \left(\sin\theta \xi_x e^{i\omega t} Y_l^0 \right) \right). \tag{5.4}$$

Considering that $\delta p = p' + \delta \vec{r} \cdot \nabla p$, the amplitude of the relative flux variation then obeys the relation,

$$\frac{\delta F}{F} \propto -\gamma \left(\frac{1}{r^2} \frac{\partial}{\partial r} \left(r^2 \xi_z e^{i\omega t} Y_l^0 \right) + \frac{1}{r \sin\theta} \frac{\partial}{\partial \theta} \left(\sin\theta \xi_x e^{i\omega t} Y_l^0 \right) \right). \tag{5.5}$$

This expression is used in eq. (5.1) to compute the luminosity perturbation. We note that the final result of the luminosity perturbation is normalized with an arbitrary number to leave it at a value close to unity. The normalization applied is the same for all cases presented below (magnetic and non-magnetic), so that the results can be compared. Likewise, the temperature fluctuation is arbitrarily normalized.

5.3 Non-Magnetic versus Magnetic Displacement

To understand the impact of the magnetic field on both the luminosity perturbation and radial velocity, we need to compute these quantities also in the non-magnetic case.

To compare the results from our magnetic model with the results from a non-magnetic oscillating star with pure p-modes, we solve the non-magnetic case using the system of equations (2.5)-(2.8) but with $\vec{B} = 0$. This non-magnetic solution provides also one of the interior boundary conditions applied in the magnetic model of Cunha (2006). The MAPPA code was modified to extract the radial component of the non-magnetic displacement solution, ξ_0, with the same normalization as that used for the magnetic solution. This non-magnetic displacement solution corresponds to that of pure acoustic waves. Because the oscillations to be considered correspond to high-order, low-degree modes, we neglected the horizontal component of the displacement which for the non-magnetic case is very small in the outermost layers of the star. Thus, the displacement can be written approximately as

$$\delta \overrightarrow{r} = \left(\xi_0(r) Y_l^0 \, \widehat{r} \right) e^{i\omega t}. \tag{5.6}$$

According to eq. (3.4) in chapter 3 the radial velocity for the non-magnetic displacement

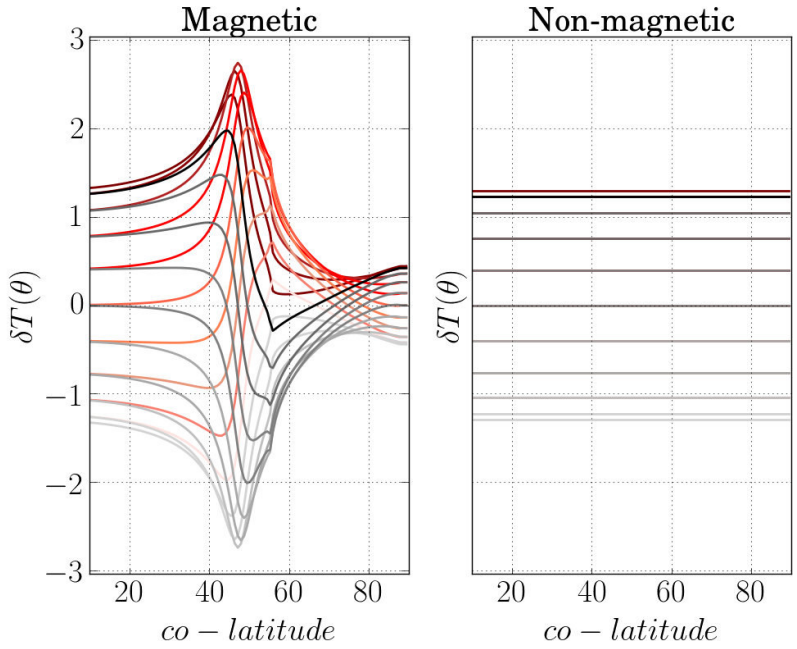

Figure 5.1: Normalized and dimensionless temperature perturbation as a function of colatitude at the photosphere (relative radius r/R=1.0), for a mode of frequency 2.2 mHz and degree $l = 0$, a magnetic field of 1 kG and a pole-on view. The color curves represent different times within the period of the oscillation. The left panel shows the magnetic model, the right panel the non-magnetic model.

is thus,

$$V_{int} = \int_{\varphi'_i}^{\varphi'_f} \int_{\theta'_i}^{\theta'_f} v_r X_r \times C_n^{-1}(1 - a(1 - \cos\theta')) \cos\theta' \sin\theta' d\theta' d\varphi', \tag{5.7}$$

with the velocity computed using the perturbation $\Re\left[v_r = \frac{d}{dt}\delta r\right]$. Moreover, the luminosity perturbation in the non-magnetic model is computed using the expression given by eq.(5.1) with the flux perturbation (eq.(5.5)) computed from the displacement considered here.

The impact of the magnetic field on the eigenfunctions is twofold. Firstly, the coupling between acoustic and magnetic waves results in an angular distortion of the eigenfunctions that, for that reason, are no longer well described by a single spherical harmonic. Secondly, due to the direction of the Lorentz force, a significant horizontal component of the displacement is generated that has no parallel in the non-magnetic case.

In Fig. 5.1 we show the temperature perturbation as a function of the colatitude at the bottom of the photosphere (relative radius $r/R = 1.0$) for the two models that we are considering: the magnetic model on left panel, and the non-magnetic model on the

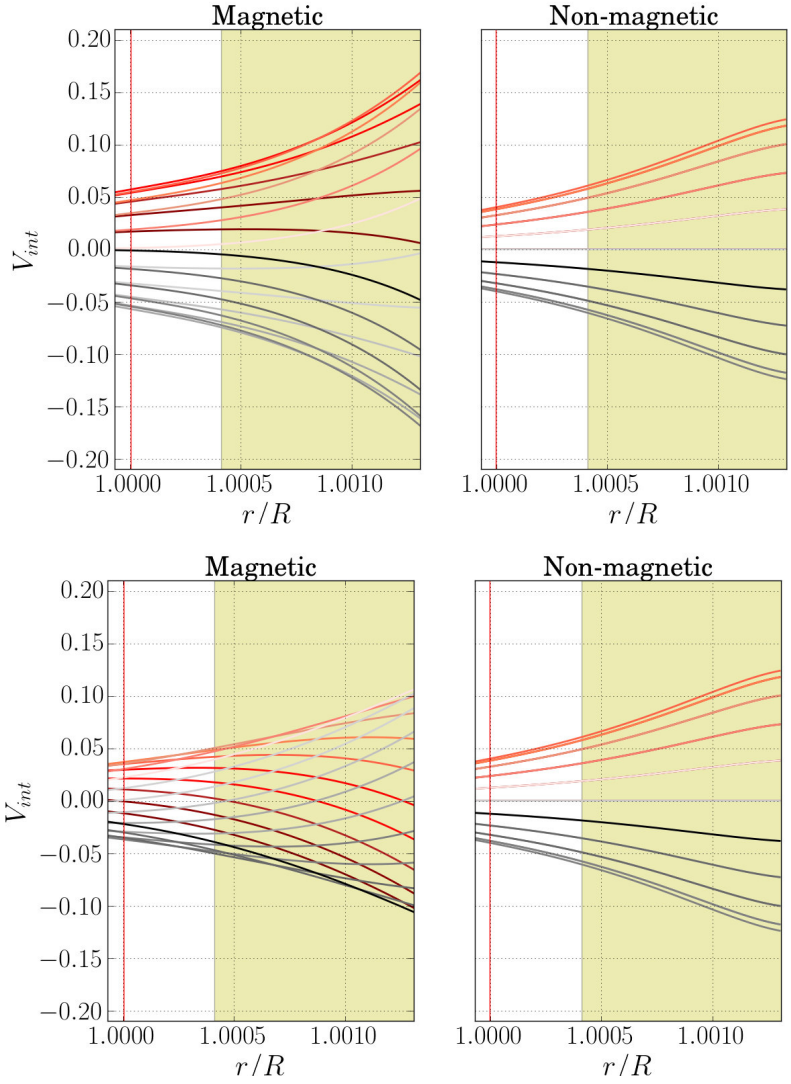

Figure 5.2: Radial velocity as a function of the radius for a mode of frequency 2.2 mHz a degree $l = 0$, a magnetic field of 1 kG and a pole-on view (top panels) and an equator-on view (bottom panels). The left panels shows the magnetic model, and the right panels the non-magnetic model.

right panel. In the figure we present a mode with a frequency of 2.2 mHz and a degree $l = 0$. The magnitude of the polar magnetic field is $B_p = 1$ kG. To make a complete analysis of the temperature perturbation of the magnetic and the non-magnetic models we need to look back at eq. (5.5). We see that the dominating term on the right hand side is the first one (associated to the large radial derivative of the radial part of the eigenfunction). Because the horizontal displacement varies only on a large scale, more precisely, a scale comparable to the angular size of the star (similar to the magnetic field), the second term on the right hand side, that comprises the derivative of the horizontal displacement, is small and does not have an impact in the flux. Likewise, the impact from the displacement on the temperature variation and on the luminosity perturbation is due, essentially, to the contribution of the radial component of the displacement.

Given that the mode considered has degree $l = 0$, the temperature perturbation in the non-magnetic model (Fig. 5.1, right panel) shows no dependence on latitude. On the other hand, looking at the temperature perturbation of the magnetic model (Fig. 5.1, left panel) we see a completely different behavior. In particular, we see a striking modulation of the temperature along the colatitude, as well as a latitudinal-dependent change in the phase of the oscillations. Because the horizontal component has no relevance in the temperature perturbation we conclude that this modulation arises, instead, from the latitudinal distortion of the wave caused by the coupling of the acoustic and magnetic waves in the magnetic boundary layer.

On the other hand, when comparing the radial velocity in the two models, one may expect the behavior to be different from that found for the temperature perturbation, as the horizontal component of the displacement has, potentially, an important role in the integration of the projected velocity field. In Fig. 5.2, we show the radial velocity as a function of the relative radius for the magnetic model, in the left panels, and for the non-magnetic model, in the right panels, for the same mode as before, with a frequency of 2.2 mHz and a degree of $l = 0$. It is shown for two different observers, looking from a pole-on (top) and an equator-on (bottom) direction. Given that the mode considered is radial, the radial velocity in the case of the non-magnetic model is independent of the observer, as expected. However for the magnetic model the radial velocity is found to be different for the different views, as we had already shown in chapter 3.

The projected components of the displacement at the bottom of the photosphere, multiplied by the limb-darkening, $limbD$, at each point in the visible surface of the star, are illustrated in the spherical plots in Fig. 5.3 for the two models. The two left spheres are for a pole-on observer and the two right spheres for an equator-on observer, alternating, from left to right, between magnetic and non-magnetic models. Top and

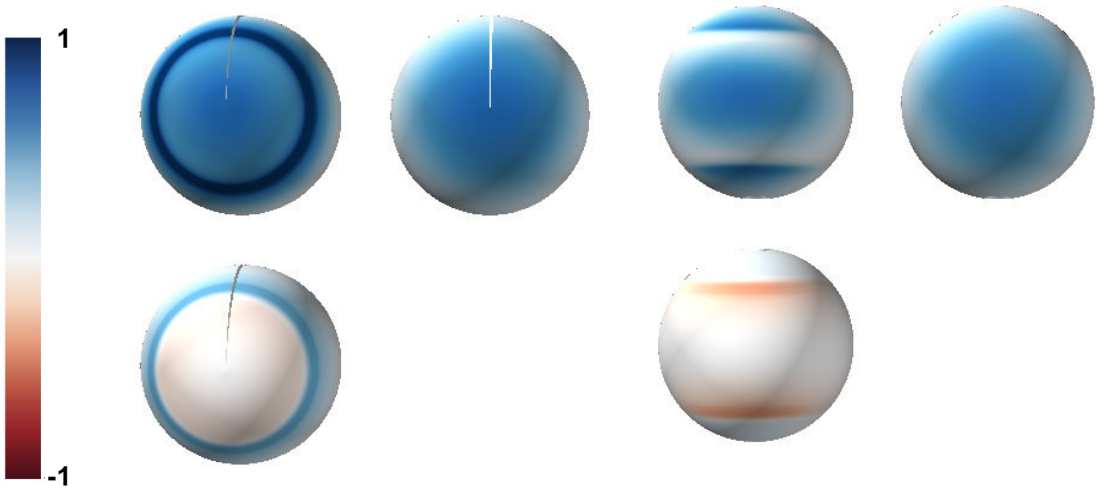

(a) pole-on view (b) equator-on view

Figure 5.3: Each panel shows the projected components of the normalized displacement multiplied by the limb darkening over the visible disk at the bottom of the photosphere, that corresponds to the relative radius of $r/R = 1.0$, for a mode with a frequency of 2.2 mHz and a degree $l = 0$, for two different views, pole-on (left panels) and equator-on (right panels). The polar magnetic field for the magnetic model is $B_p = 1$ kG. The left most spheres and the spheres on the 3rd column from the left show the projected amplitudes for the magnetic model, the top spheres concern the radial component, $\delta r_r X_r LimbD$, the bottom spheres the horizontal component, $\delta r_\theta X_\theta LimbD$. The sphere in the second column from the left and the rightmost sphere show the projected radial velocity of the non-magnetic model, $\delta r_r X_r LimbD$ (we recall that we are considering just the radial displacement in the non-magnetic model).

bottom spheres show contributions from the radial and horizontal displacement components, respectively. We do not show the contribution of the horizontal displacement in the non-magnetic case because, as mentioned earlier, it is negligible for low degree modes. In the plot, the color intensity corresponds to the magnitude, the blue color marks the regions where the function is positive and the red color the regions where it is negative.

When comparing the radial components of the magnetic and non-magnetic model, we can see in the magnetic model a larger amplitude at the mid-latitudes, from both views. This results from the latitudinal distortion of the amplitude introduced by the coupling of the magnetic and acoustic waves. Considering now the contribution from the horizontal component in the magnetic case, we see the same excess amplitude at mid-latitudes in the radial component and, in addition, an inversion in the sign of the amplitude. This sign reversal results from the variation in the phase of the waves along the colatitude which

is induced also by the latitudinal distortion introduced by the coupling of the magnetic and acoustic waves (for a detailed analysis of the time dependence of the displacement see appendix A).

Comparing Figs. 5.2 and 5.3 and focusing in the pole-on view, we notice that the amplitude of the displacement in the magnetic model is larger than in the non-magnetic model (Fig. 5.2, top panels), and that larger radial velocity is caused by the excess in the amplitude of the projected radial displacement at mid-latitudes mentioned before (Fig. 5.3, top-left panel). The horizontal displacement component for this particular case does not play a relevant role due to the latitudinal phase shift, that cancels out this contribution. Changing to the equator-on view, we find that the amplitude of the radial velocity (Fig. 5.2, bottom panels) in the magnetic case becames smaller than in the non-magnetic case. Here the horizontal displacement component is responsible for the decrease in amplitude because it contributes negatively to the radial velocity.

In summary, the amplitudes of the radial velocity and luminosity perturbation in the magnetic model are affected by a complex mixture of phenomena that result from the coupling of the acoustic and magnetic waves, such as the appearance of a significant horizontal component of the displacement, the latitudinal dependence of the amplitude and phase of the displacement, and the radial dependence of the displacement phase, which is also, latitudinal dependent. This, together with the fact that the radial velocity and observed luminosity perturbation are computed from integrations over the unresolved surface, results in a large diversity of possible outcomes that affect the visibility of the individual modes.

5.4 Visibility of low degree modes

To study the impact of the magnetic field on the visibility of modes of degree up to 7, we calculated the amplitude of the luminosity perturbation and the amplitude of the radial velocity at the bottom of the photosphere using our pulsation model, under the influence of the magnetic field, and compared them with the non-magnetic ones.

In Fig. 5.4 (a) we show the amplitude of the radial velocity (left panel) and the amplitude of the luminosity perturbation (right panel) for l modes of degrees from 0 to 7. We fix the frequency in 2.2 mHz and we vary the magnetic field from 1 to 4 kG. Fig. 5.4 (b) shows the results for the same frequency and mode degrees for the non-magnetic case. We start the analysis by concentrating on the case corresponding to a magnetic field of 1 kG (blue line top panel), in particular, by comparing it with the non-magnetic case. As expected, in the non-magnetic case the radial velocity amplitude drops drastically

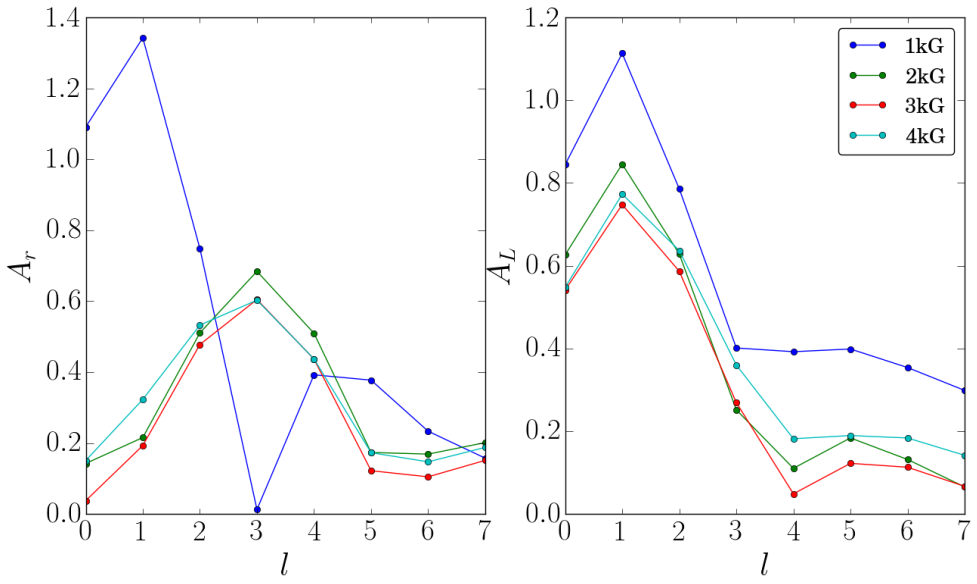

(a) Magnetic model

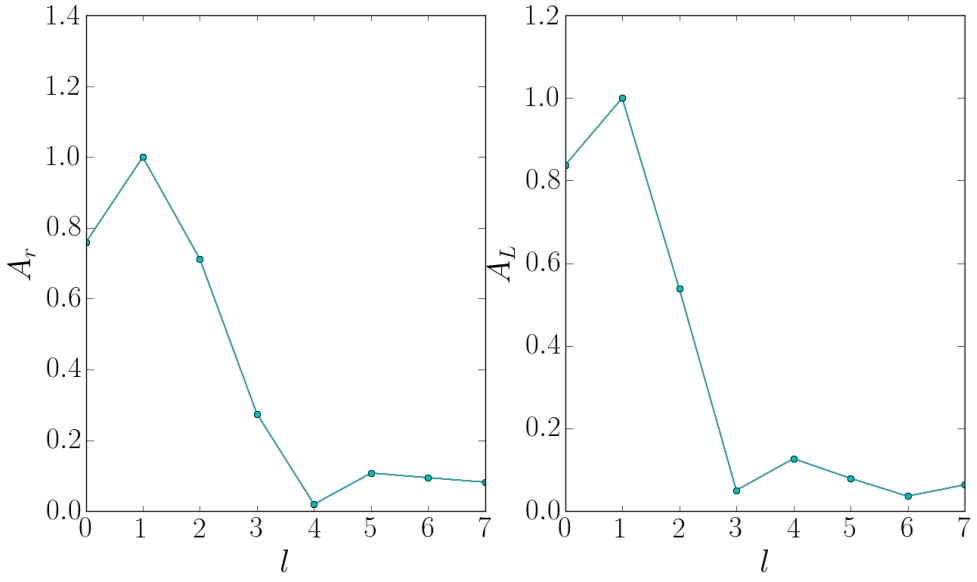

(b) Non-magnetic model

Figure 5.4: Amplitude of the radial velocity (left panels) and amplitude of the luminosity perturbation (right panels) for different mode degrees at the bottom of the photosphere for a frequency of 2.2 mHz. Pole-on view. The different colored curves are for different magnetic field polar strengths, B_p: blue for 1 kG, green for 2 kG, red for 3 kG and cyan for 4 kG. Both quantities are normalized such that they are 1 for a mode of degree $l = 1$ in the non-magnetic, pole-on view case.

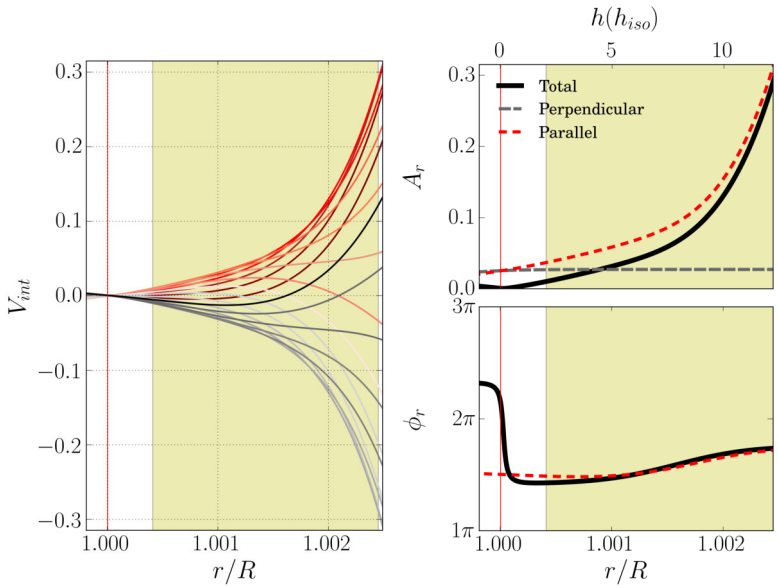

Figure 5.5: Radial velocity for a mode with a frequency of 2.2 mHz and a degree $l = 3$, with a pole-on observer and a magnetic field $B_p = 1$ kG. In the left panel is the radial velocity and in the right panels are the amplitude variation (top) and the phase variation (bottom).

for modes of degree larger than or equal to $l = 4$, while in the case of the amplitude of the luminosity perturbation significant decrease happens for modes equal or larger than $l = 3$. However, in the case of the magnetic model the results are very different from that. In the magnetic case modes of degree $l = 0, 1, 2$ have higher radial velocity and luminosity perturbation amplitudes at the bottom of the photosphere than in the non-magnetic case, but where the difference is most significant is for the higher degree modes.

For $l = 3$, we have no radial velocity in the magnetic model but the luminosity perturbation is in fact significantly larger than in the non-magnetic case. The zero radial velocity amplitude results from the fact that for this mode we have the formation of a false node right at the bottom of the photosphere, as we can see in Fig. 5.5. However, for the luminosity perturbation only the radial component of the displacement is important, since the polar displacement contributes very little to the temperature perturbation (eq. (5.3)). As a result, the cancellation that takes place when the false node in radial velocity is formed, and that results from the contribution of both displacement components, does not occur for the luminosity perturbation.

In the case of the $l = 4$, the amplitude of the radial velocity for the magnetic model increases to a value higher than that obtained for the non-magnetic model, while the amplitude of the luminosity perturbation reaches a value similar to that obtained for the

$l = 3$ mode. To investigate the origin of the differences in the magnetic and non-magnetic cases, we illustrate further the case of the mode with degree $l = 4$ in Fig. 5.6, by showing the projected components of the displacement multiplied by the limb-darkening over the visible disk, at the bottom of the photosphere. On the two left spheres we show the results for the magnetic case, and on the right sphere the results for the non-magnetic case. Blue color marks the regions where the function is positive and red color the regions where it is negative, while the color intensity corresponds to the magnitude.

For the non-magnetic case, we find that the radial velocity amplitude is almost zero, because of the alternating positive and negative projections of the radial component of the displacement. This is a well known result and is the reason why modes of degree $l = 4$ are generally not observed in pulsating stars. As this is the only component of the velocity that is relevant for the radial velocity or luminosity perturbation in the non-magnetic model, the result is that these quantities end up being very small for the mode degree under consideration. However, if we look at the results for the magnetic model, we see, on the left top sphere, an excess on the negative part located at mid-latitudes. That excess, together with the contribution from the projected horizontal displacement (bottom, left sphere) prevents the full cancellation. For the luminosity perturbation a similar cancellation happens for the non-magnetic case, although due to the absence of a projection term in the integral that defines the luminosity variation, the cancellation is not as severe for this mode as in the case of the radial velocity. For the magnetic model this cancellation is even less severe due to the excess of the radial displacement at mid-latitudes, which contributes to an excess in the flux perturbation there. It is, thus, the distortion and latitudinal phase variations of the displacement, induced by the magnetic field, that are responsible for the significant difference seen in the amplitudes of the radial velocity and luminosity perturbation for the higher degree modes, compared to the non-magnetic case.

Inspecting the cases for the other magnetic fields (2 kG- red line, 3 kG- green line, 4 kG- cyan line), we see that they are considerably different from the results obtained for the magnetic field of 1 kG (blue line). The difference is more evident in the radial velocity and for the modes with $l = 0$, 1, and 3. For the case of $l = 3$, the difference results from the fact that the false node is no longer formed when stronger magnetic fields are considered. To understand the differences seen for the $l = 0$ and $l = 1$ modes, we show in Fig. 5.7, the radial velocities for the magnetic fields varying from 1 kG to 4 kG, for a mode with a frequency of 2.2 mHz and degree $l = 0$. In addition, the radial velocity for the non-magnetic model is also illustrated for the same mode (we note that for that case only the original atmosphere of the CESAM model was considered). We

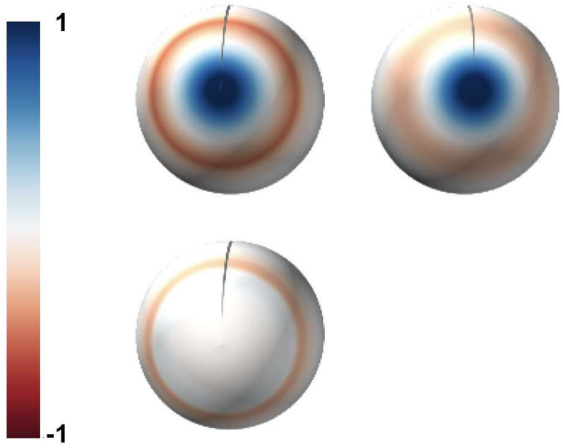

Figure 5.6: Same as Fig 5.3 but for a mode of degree $l = 4$ and an observer equator-on.

see that for magnetic fields larger than 1 kG, the interaction between the acoustic and magnetic waves near the photosphere is such that the radial velocity amplitude decreases. In the bottom-right panel of the same figure, we plot the amplitude of the radial velocity as a function of the radius for each magnetic field (dashed lines) and the non-magnetic amplitude (full black line). We can clearly see that the only amplitude that is above the non-magnetic one is that for a magnetic field of 1 kG. The other three cases have a minimum amplitude around the bottom of the photosphere (red vertical line). The cause of this difference is that, for the case of 1 kG and the frequency of 2.2 mHz, the contributions to the radial velocity of the magnetic and acoustic waves are in phase, and then, they contribute constructively to the radial velocity, whereas, for the other magnetic fields, the contributions to the radial velocity of the magnetic and acoustic waves are out of phase, consequently, they contribute destructively to the radial velocity resulting in a smaller value.

To explain this drastic change in the radial velocity behavior and, to some extent, also in the luminosity perturbation, we go back to the Fig. 2.2 in chapter 2. That figure shows the frequency shifts as a function of the cyclic frequency for different magnetic field intensities. In section 2.1 we explained the jump in frequency seen in this figure as resulting from an optimal coupling between the magnetic field and the acoustic oscillation propagating in the bulk of the star. We have analyzed what happens to the wave solutions for frequencies appearing before and after this jump, and found that the acoustic and magnetic waves' contributions change from being in phase, to being out of phase. In the present case, of a mode with a frequency of 2.2 mHz, we find from Fig. 2.2 that the mode

is before the first frequency jump for a magnetic field of 1 kG (top-left panel), but after the first jump for magnetic fields in the range 2-4 kG. For that reason, we see the drastic change in behavior in Fig. 5.4.

To further illustrate the behavior described above, we now consider a case in which we fix the magnetic field at 2 kG and analyze different frequencies. The frequency of 1.2 mHz in the top right panel of Fig. 2.2 is before the first frequency jump. If we look at the acoustic and magnetic waves' contributions to the radial velocity illustrated in the middle panels of Fig. 3.4, in chapter 3, that show the radial velocity for a mode of degree $l = 1$ in a pole-on view, we see from the color curves that the two contributions are in phase. The same happens for the $l = 0$ modes and the same frequency (Figs. 3.5 and 3.6, chapter 3). On the contrary, for the frequencies of 1.7 mHz, 2.2 mHz, and 2.7 mHz, illustrated in the middle panels of Figs. 3.9, 3.12, and 3.15, respectively, we see that the acoustic and magnetic waves' contributions to the radial velocity are out of phase. This is because all these frequencies are after the jump (top right panel of Fig. 2.2). We can then anticipate that, for a lower frequency, the change in the behavior with magnetic field strength seen in Fig. 5.4 occurs for a stronger magnetic field. For example, for a frequency of 1.2 mHz we have verified that the results for magnetic fields of 1, 2, and 3 kG behave as the blue curve in the top panel of Fig. 5.4, while the results for the magnetic field of 4 kG are more like those displayed by the curves for magnetic fields larger than 1 kG in the same figure. Looking back at Fig. 2.2, we see that this frequency is, indeed, below the first frequency jump for magnetic fields up to 3 kG, but for a 4 kG field the frequency is above the first jump.

When we change the line of sight, the dependence on mode degree of the amplitude of the photospheric radial velocity and luminosity perturbation is yet different from what we have seen with the pole-on view. In Fig. 5.8 we present these quantities for the non-magnetic model (bottom panels) and for the magnetic model (upper panels) for an observer's line of sight 45° from the pole, for the same range of magnetic field as before. We can see that with this view, in the non-magnetic model the visibility of the oscillations drops abruptly from the mode of degree $l = 2$ onwards, both for the radial velocity and luminosity perturbation. This is because for the $l = 2$ spherical harmonic and this view, the observer is looking towards a surface node and, thus, the cancellation effect is already present, leaving only the $l = 0$ and 1 modes visible. For the magnetic model, the behavior is again very different from that found for the non-magnetic model. Starting with the case of $B_p = 1$ kG, we note that now the mode of degree $l = 3$ no longer has zero radial velocity amplitude. This is because the false node mentioned in the pole-on view for $l = 3$ no longer appears when the observer is at 45°. However, from

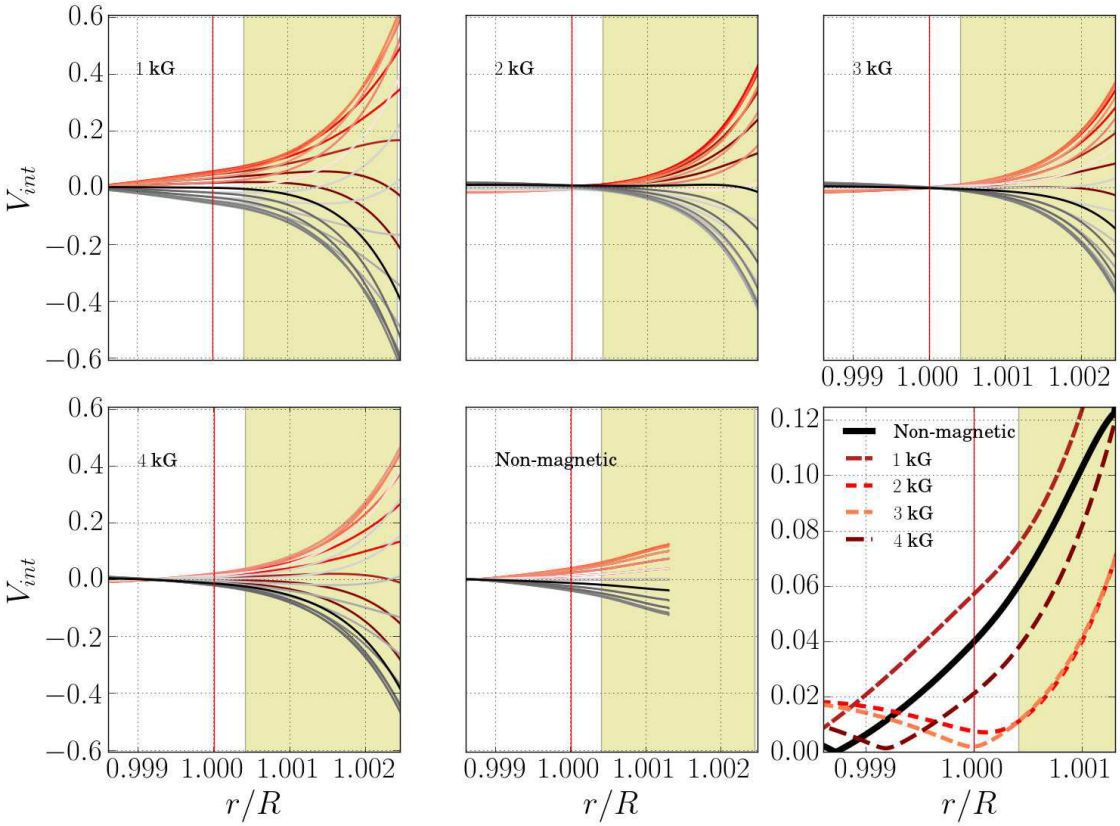

Figure 5.7: Radial velocity for a mode of frequency 2.2 mHz and degree $l = 0$, with a pole-on view. The color curves and the vertical marks are the usual. The top panels are for the magnetic fields of 1 kG on the left, 2 kG in the middle, and 3 kG on the right. The bottom panels are for the magnetic fields of 4 kG on the left, the non-magnetic radial velocity in the middle (the radial velocity curves are shorter because no isothermal atmosphere is added to the non-magnetic model), and the amplitude variation for each of the radial velocities on the right panel. The non-magnetic amplitude is shown by the full-black line, the 1 kG by the dark-red dashed line, the 2 kG by the red-dashed line, the 3 kG by the pink-dashed line, the 4 kG by the brown-dashed line.

this view we still identify the change in behavior of the radial velocity amplitude when the magnetic field is increased beyond 1 kG, discussed earlier for the pole-on observer, caused by the interaction of the magnetic and acoustic waves' components at the bottom of the photosphere. That change in behavior remains because the destructive interaction caused by the fact that the magnetic and acoustic contributions are out of phase does not depend on the line of sight.

Next we analyze the amplitude of the radial velocity and luminosity perturbation for different mode degrees from an equator-on view. From Fig. 5.9, we see that for both magnetic and non-magnetic cases, all the odd degree modes are invisible due to their anti-symmetry about the magnetic equator. We recall that the modes under consideration for both cases are defined in the coordinate system of the star which, in turn, was chosen to have the polar axis aligned with the magnetic field and that throughout this work we are only considering axissymmetric modes (i.e., with azimuthal order $m = 0$). We also see that the difference between the magnetic and non-magnetic cases for the even modes is significant. For the non-magnetic case, only $l = 0$ and 2 could be visible. For the magnetic cases, we have that the radial velocity and the luminosity amplitudes can reach significant values for higher degree modes. For the luminosity perturbation in some cases the amplitude is larger for the $l = 4$ than for the $l = 2$ modes. We note also that the amplitudes of the radial velocity and luminosity perturbation for the mode of degree $l = 2$ for the magnetic model are not as high as for the two previous line of sights. In fact, in the magnetic case we now have a radial velocity and luminosity perturbation with amplitudes lower than the values obtained in the non-magnetic case. But for the $l = 4$ we have a significantly more favorable visibility in the magnetic case than in the non-magnetic case, specially for the 1 kG field (blue line).

In Fig. 5.10 we show the projected components of the displacement multiplied by the limb-darkening over the visible disk, at the bottom of the photosphere. Results are shown for a mode of degree $l = 2$ (left panel), and a mode of degree $l = 4$ (right panel), both for the magnetic field of 1 kG and an equator-on observer, in the same way as in Fig. 5.3. For the case of $l = 2$ the radial component of the displacement of the magnetic model and the non-magnetic model (first two top spheres), show a small difference between them. The stronger intensity of the blue area in the polar regions of the magnetic model, corresponding to slightly higher positive amplitudes, cause a slightly stronger cancellation in the integration process, resulting in a slightly smaller amplitude for the radial velocity. The impact of that difference is found to be more significant for the luminosity perturbation because in the calculation of the amplitude of the luminosity perturbation the displacement is not projected onto the observer's

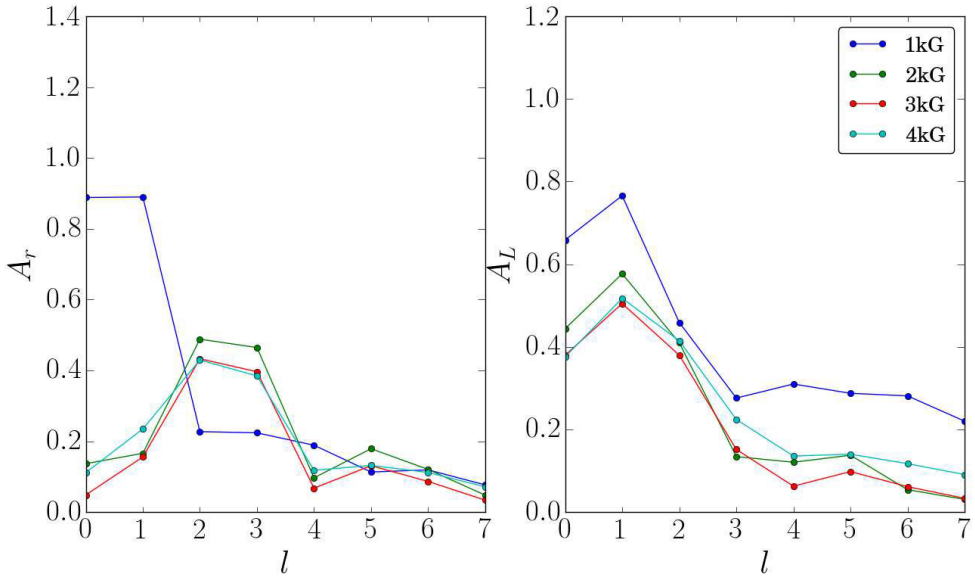

(a) Magnetic model

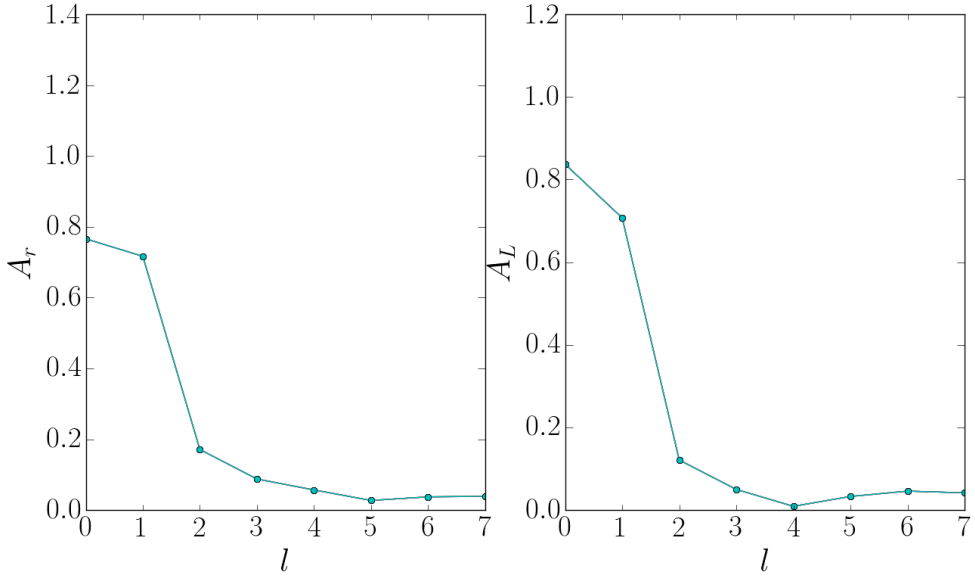

(b) Non-magnetic model

Figure 5.8: The same as Fig. 5.4 but for a line of sight 45° from the pole.

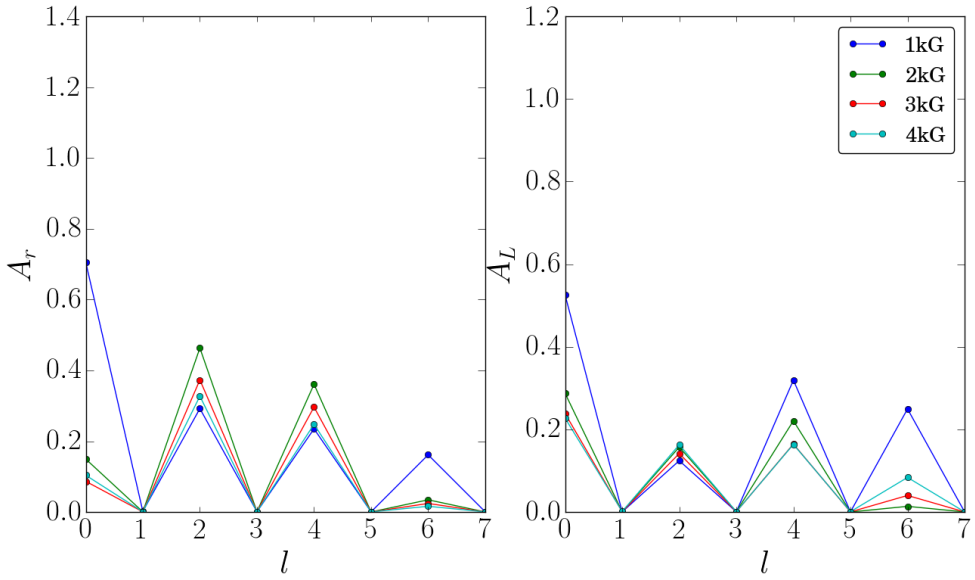

(a) Magnetic model

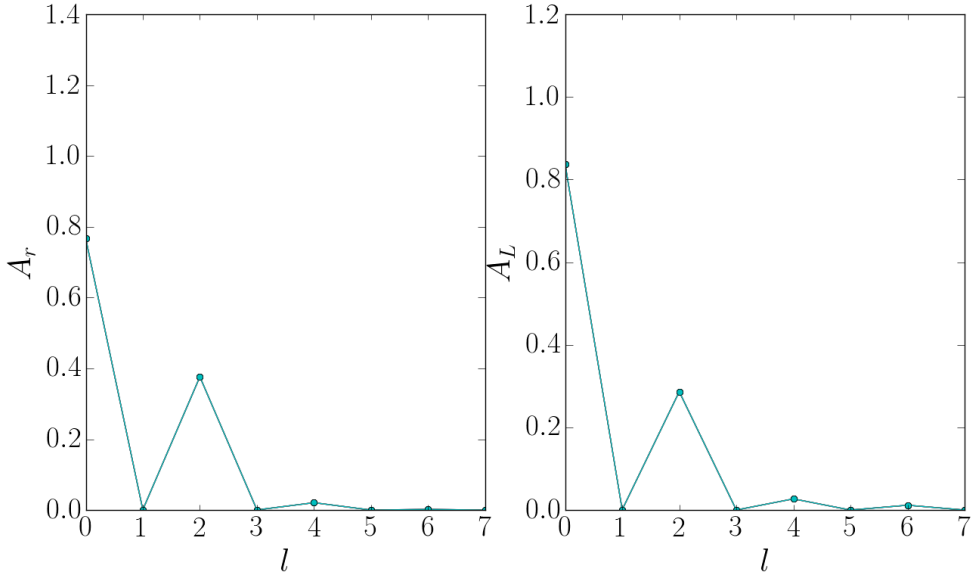

(b) Non-magnetic model

Figure 5.9: Same as Fig. 5.4 but for an observer equator-on.

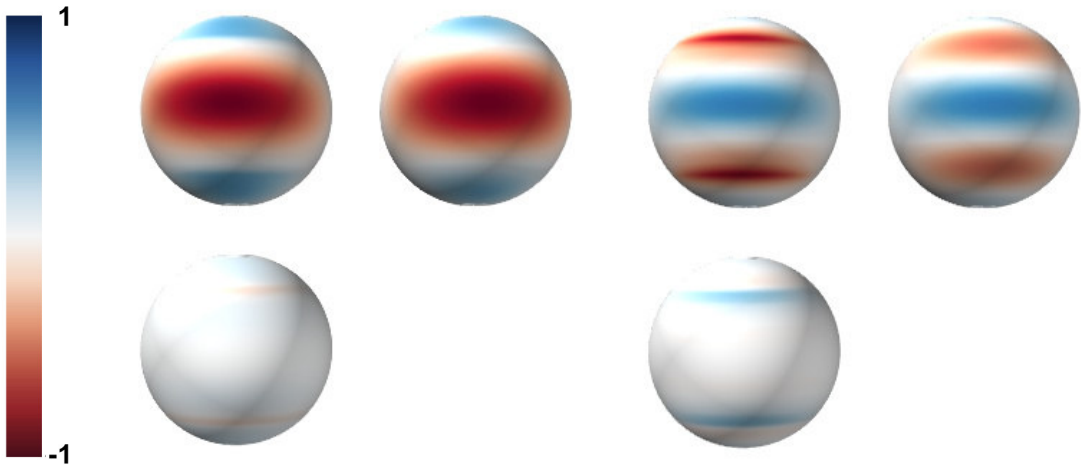

(a) $l = 2$ (b) $l = 4$

Figure 5.10: Same as Fig 5.3 but the left panels show a mode of degree $l = 2$, and the right panels show a mode of degree $l = 4$. Both with an observer equator-on.

direction. In fact, without the projection, the difference found in the magnetic and non-magnetic intensities near the borders is larger than the one seen in Fig. 5.10. In addition, in the case of the radial velocity we need to consider the horizontal component (bottom, left sphere), that contributes with a negative amplitude, hence, compensating partially for the excess positive contribution from the radial component in the magnetic case. This compensation makes the excess cancellation even less pronounced for the radial velocity than for the luminosity perturbation. For the mode of degree $l = 4$ we have a different scenario, when we compare the magnetic and the non-magnetic cases. From Fig. 5.10, right panel, top spheres, we see that there is a significant excess of the amplitude for the magnetic case, in the middle of each hemisphere. This excess prevents the cancellation seen in the non-magnetic case, resulting in the $l = 4$ modes being more visible (even more than the $l = 2$ modes) in the magnetic case both in radial velocity and in luminosity.

Chapter 6

Conclusions

6.1 General Aspects

We have developed a FORTRAN code that calculates the radial velocity and the luminosity perturbation associated to stellar oscillations in strongly magnetic stars. The code uses the displacement solution derived from the equations that describe linear perturbations about a static equilibrium under the Cowling approximation, in the presence of a magnetic field, taking into account the Lorentz force. In the case of the radial velocity computation, the velocity field is first projected in the direction of the observer and then integrated, weighted by a linear limb-darkening law. In the case of the luminosity perturbation, the flux perturbation at the bottom of the photosphere is integrated over the visible disk weighted by a limb-darkening law, where the flux perturbation is computed from the variation of the temperature associated to the displacement.

The radial velocity code allows us to study the radial velocity at different heights in the atmosphere. The integration can be performed over the full visible disk, or over a specific region at the surface, to simulate a spot of elements in the atmosphere of the star. We can, therefore, simulate different radial velocity behaviors, as seen in spectroscopic observations of roAp stars. The code for the luminosity perturbation considers the integration of the temperature variation over the visible disk, at the bottom of the photosphere, under the assumption that each element of area at the stellar surface emits like black body. This code is useful to compare with photometric observations of roAp stars.

6.2 Radial velocity

6.2.1 General behavior of the amplitude and phase

Our results for the radial velocity show that in general the amplitude increases rapidly with height, due to the rapid increase of the amplitude of the acoustic component. How significant the increase is depends also on the frequency. As higher frequencies are considered, the radial velocity can reach greater amplitudes due to the increased presence of acoustic running waves in the atmosphere of the star. As for the phase behavior, for frequencies below the acoustic cut-off the phase may vary due to a change in the type of waves that dominate the radial velocity integral. Moreover, depending on the position of the observer, the contribution of the acoustic waves in regions where the frequency is above the critical frequency, ω_c, may become dominant, resulting in a change of the phase due to the running acoustic waves. When the frequency is above the acoustic cut-off, the phase is found to vary regardless of the position of the observer. Finally, we note that the position of the observer influences the phase behavior not only because it determines the fraction of observed area where running waves are present, but also because the direction of the magnetic field around the equator makes the sound waves travel inclined to an observer that has an equator-on view, making the projection of that component of the velocity field in the direction of the observer to vary on short scales.

Concerning the contributions from the acoustic and magnetic components of the wave where these are decoupled, after inspecting the four frequencies in chapter 3 we can note that the acoustic waves dominate the behavior of the radial velocity in the upper atmosphere for most of the cases. This is explained by the difference in the amplitude behavior of the acoustic and magnetic waves. While the first has an exponential behavior in the atmosphere, the second has a constant behavior, making the acoustic waves' contributions dominant in the outer layers of the atmosphere.

In the inner layers of the atmosphere we see a different scenario, as the magnetic waves start to have an influence, changing the amplitude and the total phase of the radial velocity. This is the region where the change of dominance from acoustic to magnetic waves' contribution occurs in our model, giving rise to a phase variation that in some cases may be abrupt enough to form an false node. The position of this node, found when integrating the whole visible disk, is expected to depend on the place where the magnetic and acoustic waves decouple (illustrated in Fig. 3.3 for the current model), since that decoupling determines the relative amplitude of the two components, which beyond that point have a different dependence on atmospheric height. For that reason, it is expected that the position of the node will be different for models with different global properties

(e..g, different temperatures).

Finally, we find that apparent nodes in the higher atmospheric layers appear often for spots or belts of elements in the equatorial area, when acoustic running waves are present. Exploring several frequencies and mode degrees we found that this phenomenon can occur for any position of the observer.

6.2.2 Comparison with the observations

Our model shows that the radial velocity amplitude increases significantly (can reach one to two orders of magnitude) throughout the atmosphere. This increase is a direct consequence of the decrease in the density, as discussed in Sousa & Cunha (2011), and it is most significant when the integral defining the radial velocity is dominated by the running acoustic waves. This is in agreement with the behaviour of the radial velocity amplitudes inferred from the observations, derived from absorption lines that are formed at different depths in the atmosphere (Ryabchikova et al., 2007b,c; Kochukhov et al., 2008; Freyhammer et al., 2009).

In addition, our model shows that the phase variations throughout the atmosphere can take a variety of forms, that depend critically on the position of the observer and on the frequency of the modes. While in most cases the phase varies smoothly with height in the atmosphere, in some cases the variations are sharper, taking place over relatively short distances. These sharper variations can be found both in the low and high atmospheric regions, in our model, depending on the conditions. The cases discussed in sections 4.3.1 and 4.3.2, that simulate spots at the equatorial zone or at mid latitudes, with sharp phase variations seen at densities between $\approx 10^{-9}$ and 10^{-11} g cm^{-3}, are of particular interest when comparing with the observations. Smooth, as well as sharp radial velocity phase variations are also commonly inferred from the spectroscopic time-series of roAp stars, particularly in the strongest pulsating lines that form high in the atmosphere, between optical depths of about log tau=-4 and -6 (Saio et al., 2010, 2012), corresponding to regions of low densities similar to those mentioned above.

A common way found in the literature to analyze the observations is to combine the amplitude and phase variations in an amplitude-phase diagram. Here we perform a similar diagram based on the model results, for a chemical spot in the pole and a chemical spot in the equator. For simplicity, we shall consider that the chemical contrast is maximum, i.e., that only the regions inside the spot of a given element contribute to the radial velocity measured from that element. As we can see in Fig. 6.1, top panel, in the poles the variation in phase is smaller than in the equator, and also the amplitude can

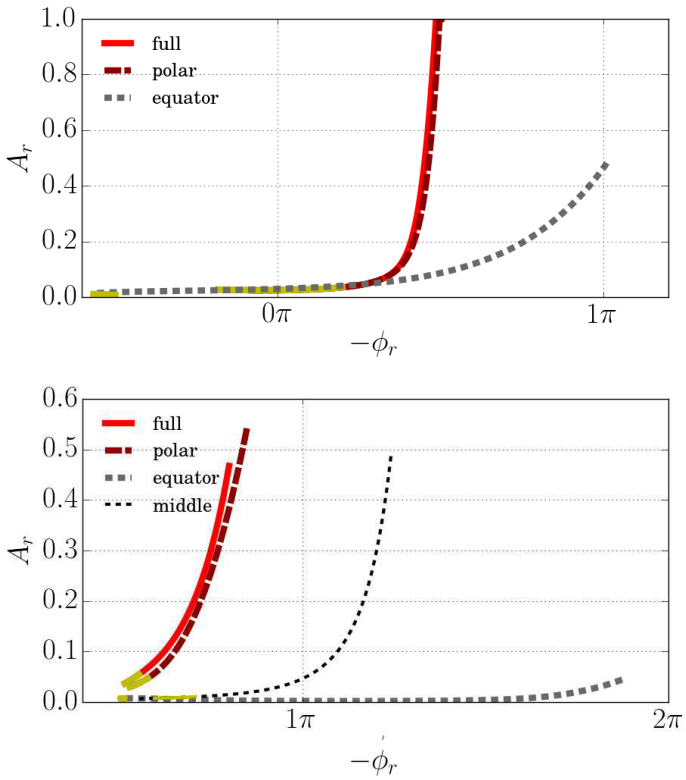

Figure 6.1: Amplitude versus phase variation. Top panel, for a mode with a frequency of 2.5 mHz and a degree $l = 0$, an observer pole-on and a magnetic field of 2 kG. Bottom panel, for a mode with a frequency of 2.3 mHz and a degree $l = 2$, and an observer pole-on and a magnetic field of 1 kG. The solid red line shows the amplitude-phase variation for integration over the full visible disk, while the long dashed dark-red line shows the result for a spot around the pole and the short thick, dashed-grey line the result for an equatorial belt. In the bottom panel, the thin, short-dashed grey line shows the case of a spot at mid latitudes. The yellow part of the curves marks the region from the bottom of the photosphere to the bottom of the isothermal atmosphere. We use the negative of ϕ_r in this figure to facilitate the comparison with the observational works (e.g. Ryabchikova et al., 2007c), where the fit is often done to a function of the form $A_r \cos(\omega t - \phi_r)$, rather than the one used in our definition (cf. eq. 3.12).

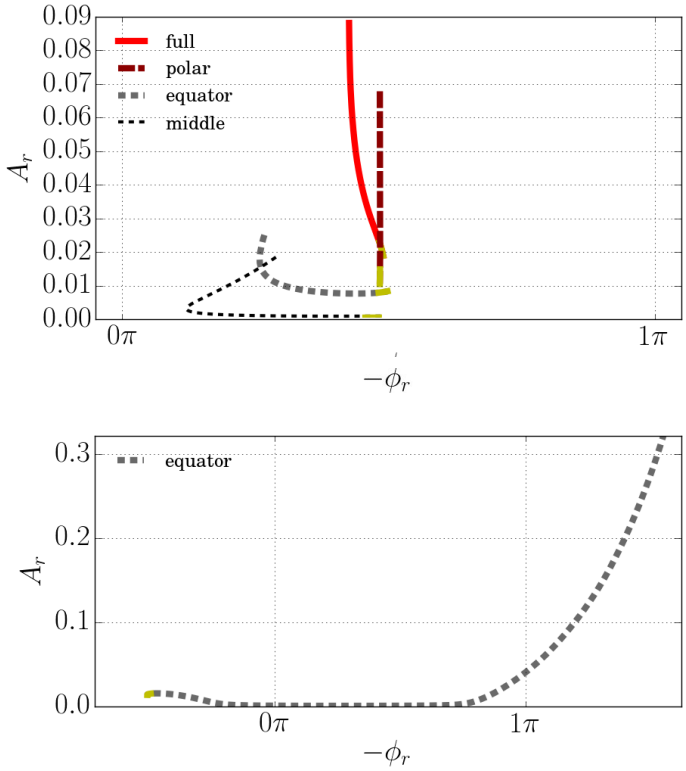

Figure 6.2: Same as Fig. 6.1, but the top panel is for a mode with a frequency of 1.9 mHz and a degree $l = 2$, an observer pole-on, and a magnetic field of 2 kG. The bottom panel is for a mode with a frequency of 2.7 mHz and a degree $l = 0$, an observer pole-on, and a magnetic field of 2 kG.

reach higher values. This difference between the radial velocity measured from elements concentrated towards the magnetic pole and towards the magnetic equator can be found also in the observations. As an example, in the case of the element Yttrium, Y, that is found to be more significantly shifted from the magnetic pole than, e.g., Nd and Pr (Lüftinger et al., 2010), the radial velocities are found to reach smaller amplitudes but to show a greater variation in phase (Ryabchikova et al., 2007c), following a behavior similar to that of the equatorial belt in Fig. 6.1. That is in contrast with the behavior found for other elements, concentrated in the polar regions, whose amplitude-phase variation behaves more like the polar spot in the same figure.

A specific example of what has been discussed before is provided by the observations of the star HD 24712, that is amongst the best studied roAp stars. The amplitude-phase diagram for this star (Ryabchikova et al., 2007b) shows a behavior that is very similar to that seen in Fig. 6.1. If we look at the position of some elements at the surface of that star (Lüftinger et al., 2010), we find that elements like Pr, Nd are distributed very close to the pole, while elements like Y and Tb are far from it, and both could be considered as spots in the middle of the hemisphere. These well behaved amplitude-phase diagrams in which phases, $-\phi_r$, all increase with increasing amplitude, such as in the example shown in Fig. 6.1 and in the observations of HD 24712, can also be found in several others roAp stars, such as in α Cir, HD 101065 and HD 124214.

Other cases studied in this work do not show such well behaved amplitude-phase diagrams. Indeed, in Fig. 6.2, top panel, we have an example of an oscillation mode whose amplitude-phase behavior is more complex. While for the integration over the full visible disk we find that the phase, $-\phi_r$, decreases with increasing amplitude, for the spot at the pole we find a constant phase. Moreover, for the spots at the equator and in the middle of the hemisphere the evolution of the phase with amplitude reverses at some point, meaning that, the phase decreases with amplitude in the inner atmosphere and increases with the latter in the outer atmosphere. This is because in the inner atmospheric layers the radial velocity is dominated by the magnetic wave's contribution while in the outer atmospheric layers is dominated by the acoustic wave's contribution. These kinds of features are present also in the observations of several stars. For example, in Ryabchikova et al. (2007c), the star HD 134214 shows a constant phase for the Pr, while other elements indicate a phase with positive variation. For γ Equ it is also found that the radial velocity measured from some elements shows a positive phase variation, while when measured from others element the phase is found to have a negative variation. Also, features like the reverse in the phase behavior can be found in some stars. Examples are shown by the studies of the Hα lines in γ Equ, or of the Nd lines in HD 134214.

A claim found in several observational papers is that a node can sometimes be seen in the outer parts of the atmosphere of roAp stars. Based on physical grounds, in a model atmosphere like the one adopted here we do not expect a node anywhere in the outer atmosphere of the star. Even for relatively low magnetic fields, the magnetic and acoustic waves are decoupled throughout most of the atmosphere. The amplitude of the magnetic waves is constant and has a characteristic scale that is larger than the atmosphere, thus, it cannot show a node. Moreover, the amplitude of the acoustic waves, with an exponential growth, is either non-oscillatory, when the frequency is below the critical cut-off frequency ω_c, or has an oscillatory behavior that changes with time, when the frequency is above ω_c. Therefore, in such a model, any node detected in the outer atmosphere must be only apparent, resulting from the projection and integration of the velocity field over the visible disk or part of it. We have shown an example of how that observational illusion can occur, in sections 4.3.1 and 4.3.2. In Fig. 6.2, bottom panel, we can see the amplitude versus phase variation diagram for the first case in section 4.3.1, namely, that of an equatorial belt with a mode with a frequency of 2.7 mHz, degree $l = 0$, and a magnetic field of polar magnitude $B_p = 2$ kG. The node is evident in the grey dashed line, as we can see that the amplitude first decreases, then goes through a minimum of almost a pi long over a short variation of radius, and grows back again. This kind of behavior can be seen in the amplitude versus phase diagrams of 33 Lib and 10 Aql (Ryabchikova et al., 2007c; Sachkov et al., 2008).

On the other hand, true node-like features may be physically expected if sharp structural variations, capable of reflecting partially the acoustic waves, are present in the atmosphere. That kind of phenomenon has been discussed in different contexts, including in the transition between the chromosphere and corona in the sun (Balmforth & Gough, 1990) and has been found in models of roAp stars presented by Saio et al. (2010, 2012). In the latter case, the partial reflection of the waves is thought to be associated to the temperature inversion that is present in their model atmosphere. Evidence for non-standard temperature gradients, including temperature inversions, has been found in a number of Ap stars. These abnormal temperature gradients are linked to a chemical stratification of elements, in particular a significant accumulation of REEs in the outer atmospheric layers (e.g. Shulyak et al., 2009, 2010). In any case, the main impact on pulsations of this complexity of the Ap stars' atmospheric structure is expected to come from the possible temperature inversion, which, as mentioned above, will induce partial reflection of the acoustic waves. In particular, that partial reflection is likely in the origin of the quasi-nodes discussed in Saio's work.

Two stars have been argued to show a node in the atmosphere, 33 Lib and 10 Aql

(Mkrtichian et al., 2003; Elkin et al., 2008; Sachkov et al., 2008). These two stars have a main frequency above the acoustic cut-off frequency and very long rotational periods. Because of the latter the magnetic field structure and the surface distribution of elements cannot be derived making difficult a direct comparison with our model. Nevertheless, in the light of the understanding of the problem provided by the present work we can confidently conclude that either we are in the presence of a false node, resulting from the cancellation effect of the acoustic and magnetic waves' contributions to the integral defining the radial velocity, or sharp variations in the atmospheric structure of these roAp stars are capable of significantly reflecting the acoustic waves. Checking the latter possibility requires adopting a more realistic atmospheric model, which we will do in a future work.

In conclusion, we find that the behavior of the radial velocity in our magnetic model resembles that inferred from high-resolution spectroscopic time-series of roAp stars, both in the amplitude and phase variations throughout the atmosphere. Quantitative comparisons and further tests to the model shall be carried out in a follow-up work directed at the modeling of particular stars, in which the atmospheric structure to adopt will be one derived from empirical self-consistent modeling of the stellar spectra.

6.3 Visibility of the modes

To understand the potential impact of the magnetic field on the visibility of the low-degree modes of oscillation in roAp stars, we have compared the radial velocity and luminosity perturbation for the cases of a magnetic and a non-magnetic model. We verified that in the magnetic model the amplitude of the luminosity perturbation can reach higher values due to the coupling of the acoustic and magnetic waves that modifies the amplitude of the displacement according to the colatitude.

This is particularly clear for modes of degree $l = 3$ or larger that may in some cases become visible, when have been generally assumed to be invisible due to cancellation effects in a non-magnetic star. This may also be true, although not as evident, for the case of radial velocity observations. In both cases the visibility of these higher degree modes seems to depend critically on the combination of magnetic field and mode frequency.

Significant differences in the magnetic and non-magnetic visibilities are seen also for the lowest degree modes. In particular, in the case of the radial velocity, it seems that certain combinations of magnetic field and frequency lead to a strong suppression of the radial velocity amplitude, resulting in, e.g., $l = 2$ modes being more visible than $l = 0$ and $l = 1$ modes.

Bibliography

Aerts C., Christensen-Dalsgaard J., Kurtz D. W., 2010, Asteroseismology. Springer

Alecian G., 2015, Monthly Notices of the Royal Astronomical Society, 454, 3143

Alecian G., Stift M., 2017, Monthly Notices of the Royal Astronomical Society, 468, 1023

Alecian E., Villebrun F., Grunhut J., Hussain G., Neiner C., 2017, arXiv preprint arXiv:1705.10650

Alentiev D., Kochukhov O., Ryabchikova T., Cunha M., Tsymbal V., Weiss W., 2012, Monthly Notices of the Royal Astronomical Society: Letters, 421, L82

Appourchaux T., et al., 2008, Astronomy and Astrophysics, 488, 705

Babcock H., 1947, The Astrophysical Journal, 105, 105

Baglin A., Auvergne M., Catala C., Michel E., Team C., et al., 2001, in SOHO 10/GONG 2000 Workshop: Helio-and Asteroseismology at the Dawn of the Millennium. pp 395–398

Baglin A., et al., 2002, in Stellar Structure and Habitable Planet Finding. pp 17–24

Baldry I., Bedding T., Viskum M., Kjeldsen H., Frandsen S., 1998, Monthly Notices of the Royal Astronomical Society, 295, 33

Balmforth N., Gough D., 1990, Solar Physics, 128, 161

Balmforth N., Cunha M., Dolez N., Gough D., Vauclair S., 2001, Monthly Notices of the Royal Astronomical Society, 323, 362

Balona L. A., et al., 2010, Monthly Notices of the Royal Astronomical Society, 410, 517

Balona L., et al., 2011, Monthly Notices of the Royal Astronomical Society, 413, 2651

Bedding T. R., et al., 2010, The Astrophysical Journal Letters, 713, L176

Benomar O., et al., 2018, Science, 361, 1231

Bigot L., Dziembowski W., 2002, Astronomy & Astrophysics, 391, 235

Bigot L., Kurtz D., 2011, Astronomy & Astrophysics, 536, A73

Bigot L., Provost J., Berthomieu G., Dziembowski W., Goode P., 2000, Astronomy and Astrophysics, 356, 218

Bowman D. M., Kurtz D. W., 2018, Monthly Notices of the Royal Astronomical Society, 476, 3169

Braithwaite J., Spruit H. C., 2004, Nature, 431, 819

Bruntt H., et al., 2009, Monthly Notices of the Royal Astronomical Society, 396, 1189

Chaplin W. J., Basu S., 2008, Solar Physics, 251, 53

Chaplin W., et al., 2010, The Astrophysical Journal Letters, 713, L169

Christensen-Dalsgaard J., 2002, Reviews of Modern Physics, 74, 1073

Christensen-Dalsgaard J., Arentoft T., Brown T., Gilliland R., Kjeldsen H., Borucki W., Koch D., 2007, Comm. in Asteroseismology, 150

Claret A., Hauschildt P., 2003, Astronomy & Astrophysics, 412, 241

Cowling T. G., 1941, Monthly Notices of the Royal Astronomical Society, 101, 367

Cunha M. S., 2002, Monthly Notices of the Royal Astronomical Society, 333, 47

Cunha M., 2006, Monthly Notices of the Royal Astronomical Society, 365, 153

Cunha M., 2007, Communications in Asteroseismology, 150, 48

Cunha M. S., Gough D., 2000, Monthly Notices of the Royal Astronomical Society, 319, 1020

Cunha M., Alentiev D., Brandão I., Perraut K., 2013, Monthly Notices of the Royal Astronomical Society, 436, 1639

Dziembowski W., 1977, Acta Astronomica, 27, 203

Dziembowski W., Goode P., 1985, The Astrophysical Journal, 296, L27

Dziembowski W., Goode P. R., 1996, The Astrophysical Journal, 458, 338

Elkin V., Kurtz D., Mathys G., 2008, Monthly Notices of the Royal Astronomical Society, 386, 481

Freyhammer L., Kurtz D., Elkin V., Mathys G., Savanov I., Zima W., Shibahashi H., Sekiguchi K., 2009, Monthly Notices of the Royal Astronomical Society, 396, 325

Gilliland R. L., et al., 2010, Publications of the Astronomical Society of the Pacific, 122, 131

Gough D., 1986, in Hydrodynamic and Magnetodynamic Problems in the Sun and Stars. p. 117

Gruberbauer M., et al., 2008, Astronomy & Astrophysics, 480, 223

Hale G., 1908, Publ. astr. Soc. Pacific, 20, 220

Holdsworth D. L., et al., 2014a, Monthly Notices of the Royal Astronomical Society, 439, 2078

Holdsworth D. L., Smalley B., Kurtz D. W., Southworth J., Cunha M. S., Clubb K. I., 2014b, Monthly Notices of the Royal Astronomical Society, 443, 2049

Holdsworth D. L., Kurtz D. W., Smalley B., Saio H., Handler G., Murphy S. J., Lehmann H., 2016, Monthly Notices of the Royal Astronomical Society, 462, 876

Joshi S., Joshi Y. C., 2015, Journal of Astrophysics and Astronomy, 36, 33

Joshi S., Mary D., Martinez P., Kurtz D., Girish V., Seetha S., Sagar R., Ashoka B., 2006, Astronomy & Astrophysics, 455, 303

Joshi S., et al., 2016, Astronomy & Astrophysics, 590, A116

Khomenko E., Kochukhov O., 2009, The Astrophysical Journal, 704, 1218

Koch D. G., et al., 2010, The Astrophysical Journal Letters, 713, L79

Kochukhov O., 2004, The Astrophysical Journal Letters, 615, L149

Kochukhov O., 2005, EAS Publications Series, 17, 103

Kochukhov O., 2010, arXiv preprint arXiv:1010.0264

Kochukhov O., Ryabchikova T., 2017, Monthly Notices of the Royal Astronomical Society, 474, 2787

Kochukhov O., Ryabchikova T., Bagnulo S., Curto G. L., 2008, Astronomy & Astrophysics, 479, L29

Kochukhov O., Lundin A., Romanyuk I., Kudryavtsev D., 2011, The Astrophysical Journal, 726, 24

Kurtz D., 1978, Information bulletin on variable stars, 1436

Kurtz D., 1982, Monthly Notices of the Royal Astronomical Society, 200, 807

Kurtz D., 1989, Monthly Notices of the Royal Astronomical Society, 238, 1077

Kurtz D., 2013, EAS Publications Series, 63, 151

Kurtz D. W., 2014, Asteroseismology, 22, 163

Kurtz D., Shibahashi H., Goode P., 1990, Monthly Notices of the Royal Astronomical Society, 247, 558

Kurtz D., Elkin V., Mathys G., 2005a, Monthly Notices of the Royal Astronomical Society: Letters, 358, L6

Kurtz D., et al., 2005b, Monthly Notices of the Royal Astronomical Society, 358, 651

Kurtz D. W., et al., 2011, Monthly Notices of the Royal Astronomical Society, 414, 2550

Landstreet J., 1992, The Astronomy and Astrophysics Review, 4, 35

Landstreet J., Mathys G., 2000, Astronomy and Astrophysics, 359, 213

Ledoux P., 1951, Astrophysical Journal, 114, 373

Lüftinger T., Kochukhov O., Ryabchikova T., Piskunov N., Weiss W., Ilyin I., 2010, Astronomy & Astrophysics, 509, A71

Martinez P., Kurtz D., 1994, Monthly Notices of the Royal Astronomical Society, 271, 129

Martinez P., Kurtz D., Kauffmann G., 1991, Monthly Notices of the Royal Astronomical Society, 250, 666

Mathys G., 2017, Astronomy & Astrophysics, 601, A14

Matthews J. M., Wehlau W. H., Walker G. A., Yang S., 1988, The Astrophysical Journal, 324, 1099

Mkrtichian D. E., Hatzes A. P., Kanaan A., 2003, Monthly Notices of the Royal Astronomical Society, 345, 781

Morel P., 1997, Astronomy and Astrophysics-Supplement Series, 124, 597

Neiner C., Mathis S., Alecian E., Emeriau C., Grunhut J., et al., 2014, Proceedings of the International Astronomical Union, 10, 61

Pagano I., et al., 2014, in European Planetary Science Congress.

Paunzen E., Netopil M., Rode-Paunzen M., Handler G., Božić H., Ruždjak D., Sudar D., 2012, Astronomy & Astrophysics, 542, A89

Preston G. W., 1974, Annual Review of Astronomy and Astrophysics, 12, 257

Reiners A., 2012, Living Reviews in Solar Physics, 9, 1

Ricker G. R., et al., 2010, in Bulletin of the American Astronomical Society. p. 459

Ryabchikova T., et al., 2007b, Astronomy & Astrophysics, 462, 1103

Ryabchikova T., et al., 2007a, Astronomy and Astrophysics-Les Ulis, 462, 1103

Ryabchikova T., Sachkov M., Kochukhov O., Lyashko D., 2007c, Astronomy & Astrophysics, 473, 907

Sachkov M., Kochukhov O., Ryabchikova T., Huber D., Leone F., Bagnulo S., Weiss W., 2008, Monthly Notices of the Royal Astronomical Society, 389, 903

Saio H., 2005, Monthly Notices of the Royal Astronomical Society, 360, 1022

Saio H., Gautschy A., 2004, Monthly Notices of the Royal Astronomical Society, 350, 485

Saio H., Ryabchikova T., Sachkov M., 2010, Monthly Notices of the Royal Astronomical Society, 403, 1729

Saio H., Gruberbauer M., Weiss W., Matthews J., Ryabchikova T., 2012, Monthly Notices of the Royal Astronomical Society, 420, 283

Schmid V., Aerts C., 2016, Astronomy & Astrophysics, 592, A116

Shibahashi H., 1979, Publications of the Astronomical Society of Japan, 31, 87

Shibahashi H., Takata M., 1993, Publications of the Astronomical Society of Japan, 45, 617

Shulyak D., Tsymbal V., Ryabchikova T., Stütz C., Weiss W., 2004, Astronomy and Astrophysics, 428, 993

Shulyak D., Ryabchikova T., Mashonkina L., Kochukhov O., 2009, Astronomy & Astrophysics, 499, 879

Shulyak D., Ryabchikova T., Kildiyarova R., Kochukhov O., 2010, Astronomy & Astrophysics, 520, A88

Smalley B., et al., 2011, Astronomy & Astrophysics, 535, A3

Smalley B., et al., 2015, Monthly Notices of the Royal Astronomical Society, 452, 3334

Smalley B., et al., 2016, Monthly Notices of the Royal Astronomical Society, p. stw2903

Sousa J., Cunha M., 2008a, Contributions of the Astronomical Observatory Skalnaté Pleso, 38, 453

Sousa S., Cunha M., 2008b, Monthly Notices of the Royal Astronomical Society, 386, 531

Sousa J., Cunha M., 2011, Monthly Notices of the Royal Astronomical Society, 414, 2576

Takata M., Shibahashi H., 1994, Publications of the Astronomical Society of Japan, 46, 301

Tassoul M., 1980, The Astrophysical Journal Supplement Series, 43, 469

Tassoul M., 1990, The Astrophysical Journal, 358, 313

Van Reeth T., Tkachenko A., Aerts C., 2016, Astronomy & Astrophysics, 593, A120

Villebrun F., Alecian E., Bouvier J., Hussain G., Folsom C., 2016, in SF2A-2016: Proceedings of the Annual meeting of the French Society of Astronomy and Astrophysics. pp 199–202

Appendices

Appendix A

Temporal variation of the velocity Field

A.1 Dipolar cases

To illustrate how the velocity field of the pulsation, with and without the magnetic distortion, varies over time in an oscillation cycle, we have included here figures for some of the cases discussed in chapter 5.

The Fig A.1 shows the normalized and projected velocity field multiplied by limb darkening (hereafter designated projected velocity field, for simplicity) at the surface of the star, for a mode of frequency 2.2 mHz and degree of $l = 0$. The magnetic field of 1kG and the observer has a pole-on view. Each panel is for a different time within the period of oscillation. The large spheres show the total velocity field projected onto the observer's directions, the magnetic model on the left sphere, and the non-magnetic model on the right one. In addition, the radial and the horizontal components of the velocity field projected onto the observer's direction are shown in the middle panels, top and bottom, respectively. Following the right spheres in time (moving between consecutive panels), we can see how the radial oscillation in the non-magnetic case is a simple oscillation varying from zero to the positive maximum velocity, to zero again, into its negative maximum. But, for the magnetic case, we can see that the oscillation is not that simple. The first thing that stands out, is that at no time the velocity field is completely zero during the whole period of oscillation. This is because of the phase shift introduced by the coupling of the magnetic and acoustic waves. When we look at the radial and horizontal components (middle spheres) this became more evident as we always have a non-zero contribution from one of the two components. Although the radial velocity

passes through zero in the magnetic model, the velocity field itself is not zero, unlike in the non-magnetic case.

The second Fig. (A.2) that we present is for the same case (mode of frequency 2.2 mHz, and a degree of $l = 0$, and a magnetic filed of 1kG) but for an equator-on view. We can see that the projected velocity field for the non-magnetic case (right spheres) is the same as for the previous view (except from the normalization, which is based on the maximum value in the magnetic model), as is expected for a mode of $l = 0$. On the contrary, the projected velocity field for the magnetic case (left spheres) has a completely different shape. This is due to the distortion caused by the dipolar magnetic field. As for the previous view, at no time during the oscillation period the velocity field is completely zero.

The third Fig (A.3) shows the projected velocity field for the case a magnetic field of 2 kG. The oscillation mode is for a frequency of 2.2 mHz and a degree of $l = 0$, with a pole-on view. The non-magnetic case (right spheres) still looks the same as in the previews figures, since the degree is still $l = 0$. The magnetic case (left spheres), in contrast, looks different from the case presented in Fig. (A.1), for a magnetic field of 1 kG. If we look at the projected radial and horizontal components (middle spheres), we see that they are always in out of phase, consequently the radial velocity will be affected, due to the cancellation effect.

A.2 False node

Here we show the case of the false node for a mode of degree $l = 3$ discussed in Chapter 5. The oscillation mode has a frequency of 2.2 mHz and a degree of $l = 3$. The case is for magnetic filed of 1 kG and a pole-on view. Fig. (A.4) shows the projected velocity field at different times within an oscillation period, as in the figures described in A.1. In the non-magnetic case (right spheres) we see a reversed in amplitude due to the degree of the spherical harmonics ($l = 3$). In the magnetic case (left spheres) we see that the distortion caused by the magnetic field is acting in such a way that the positive part of the projected velocity field is always similar to the negative part, which explains the presence of the false node when the integration is performed.

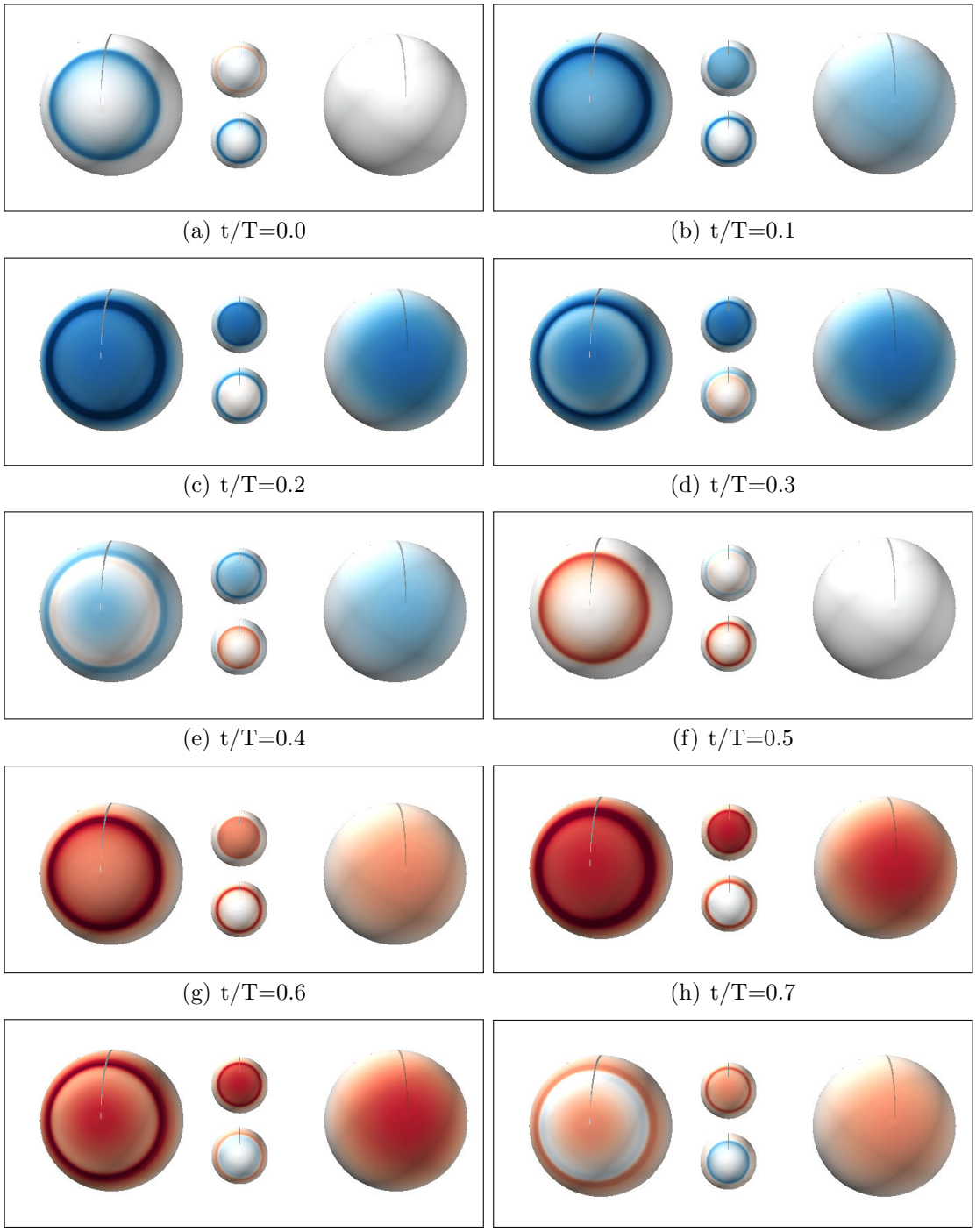

(a) t/T=0.0 (b) t/T=0.1

(c) t/T=0.2 (d) t/T=0.3

(e) t/T=0.4 (f) t/T=0.5

(g) t/T=0.6 (h) t/T=0.7

(i) t/T=0.8 (j) t/T=0.9

Figure A.1: Each panel shows the velocity field projected and multiplied by the limb darkening at different times within the oscillation period, for a mode of frequency 2.2 mHz, degree $l = 0$, the magnetic field of $B_p = 1$ kG, from a pole-on view. In each panel, the magnetic model is shown on the left sphere, its radial and horizontal components in the middle top and bottom spheres, respectively, and the non-magnetic model on the right sphere.

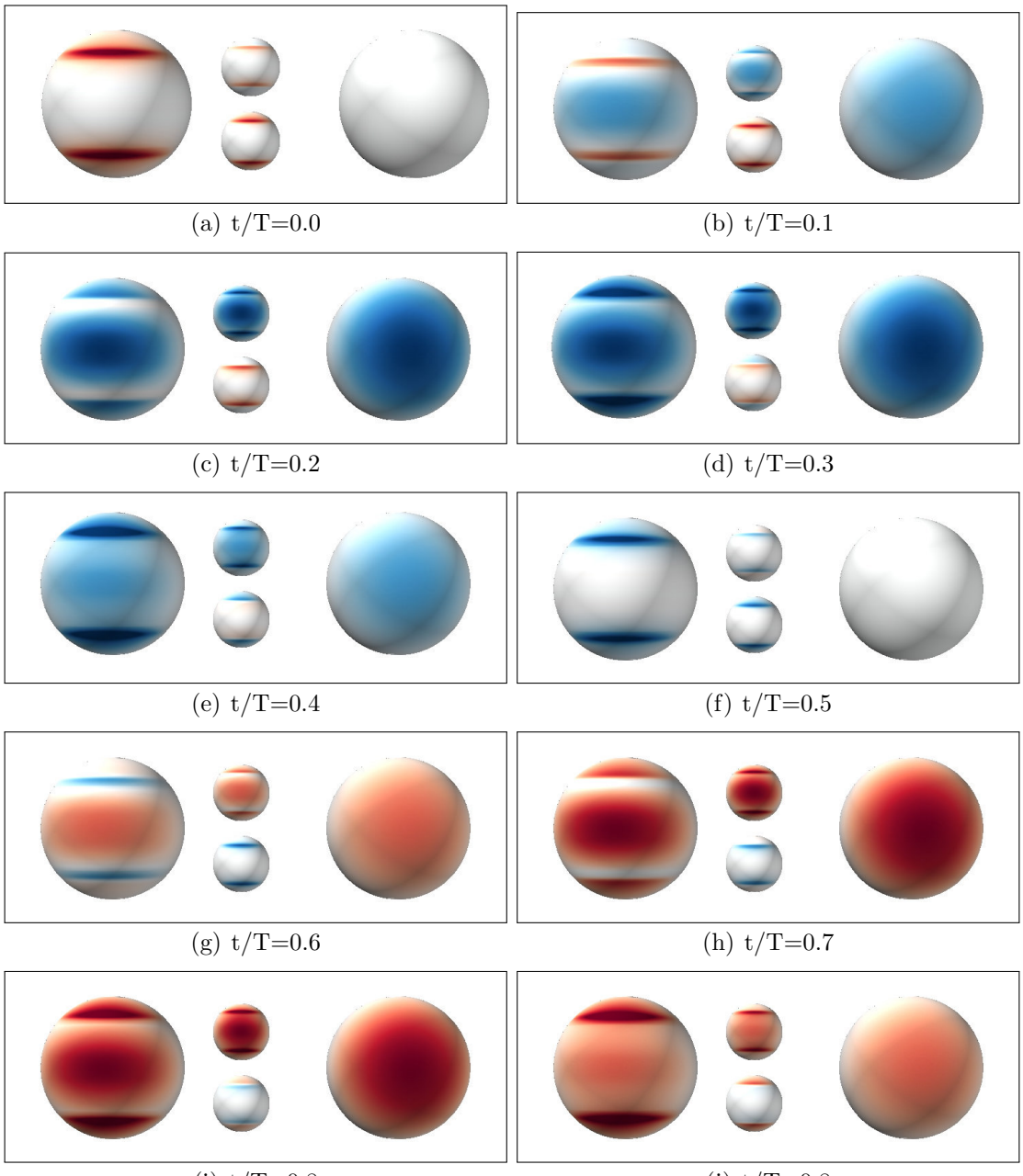

(a) t/T=0.0 (b) t/T=0.1

(c) t/T=0.2 (d) t/T=0.3

(e) t/T=0.4 (f) t/T=0.5

(g) t/T=0.6 (h) t/T=0.7

(i) t/T=0.8 (j) t/T=0.8

Figure A.2: The same as Fig. A.1 but for an observer equator-on.

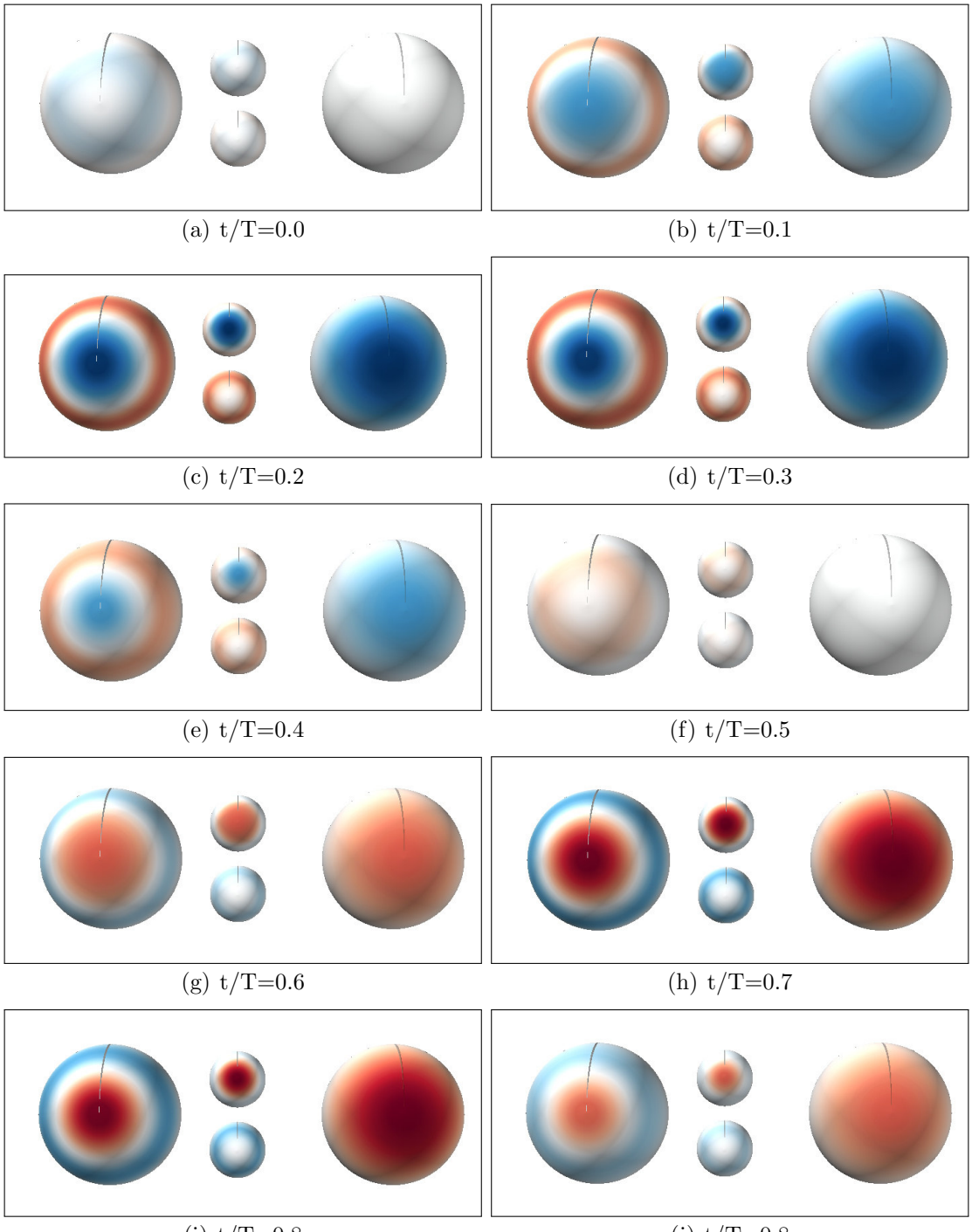

(a) t/T=0.0 (b) t/T=0.1

(c) t/T=0.2 (d) t/T=0.3

(e) t/T=0.4 (f) t/T=0.5

(g) t/T=0.6 (h) t/T=0.7

(i) t/T=0.8 (j) t/T=0.8

Figure A.3: The same as Fig. A.1 but for a magnetic field of $B_p = 2$ kG.

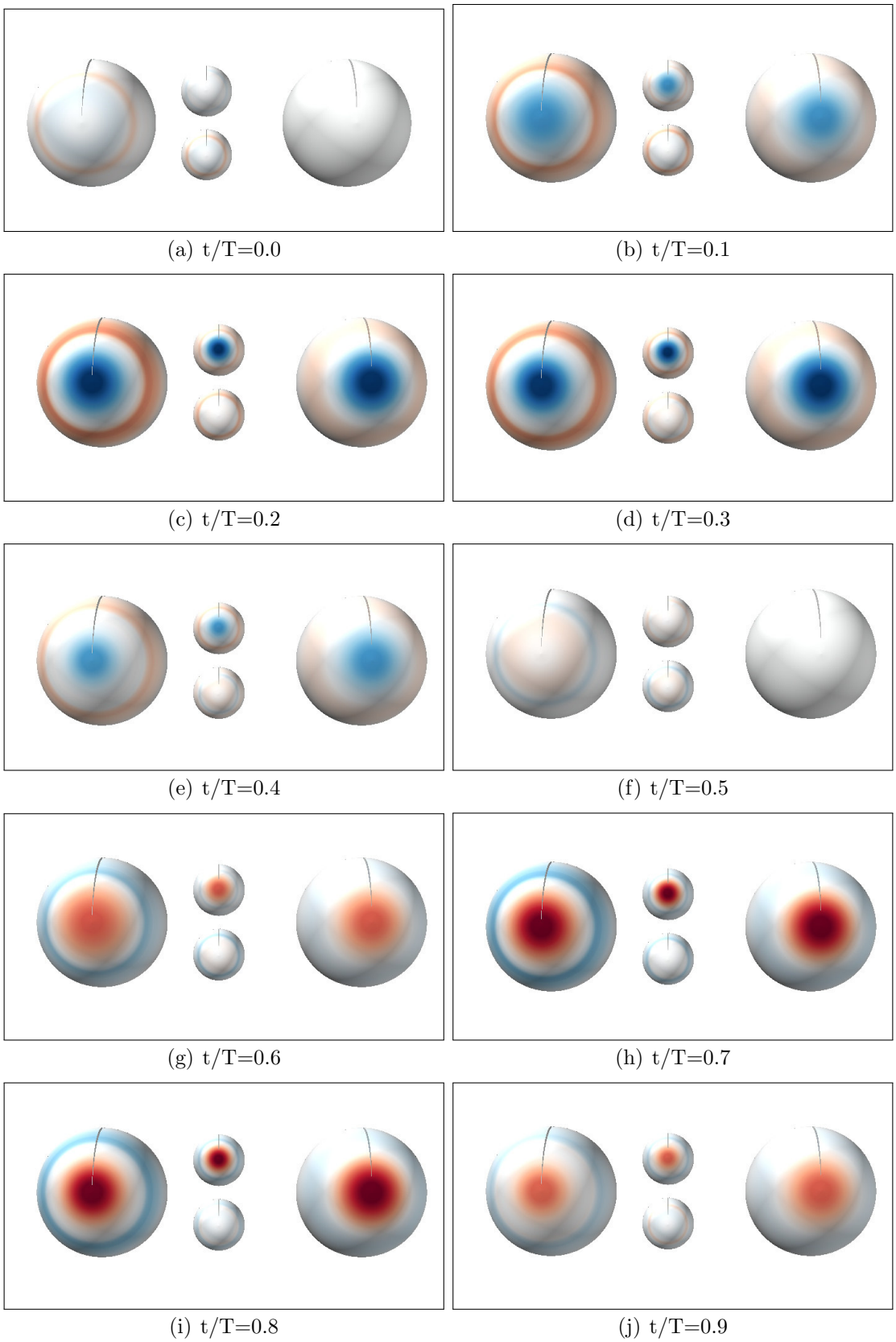

(a) t/T=0.0 (b) t/T=0.1

(c) t/T=0.2 (d) t/T=0.3

(e) t/T=0.4 (f) t/T=0.5

(g) t/T=0.6 (h) t/T=0.7

(i) t/T=0.8 (j) t/T=0.9

Figure A.4: The same as Fig. A.1 but for a mode of degree $l = 3$.